NUMERICAL SIMULATIONS OF RESISTIVE
MAGNETOHYDRODYNAMIC INSTABILITIES
IN A POLOIDAL DIVERTOR TOKAMAK

by

EIJIRO UCHIMOTO

A thesis submitted in partial fulfillment of
the requirements for the degree of

Doctor of Philosophy
(Physics)

at the
UNIVERSITY OF WISCONSIN-MADISON
1988

Dedication

This thesis is dedicated to my parents,
Heihachiro and Kiyo Uchimoto,
and aunt, Utako Ichikawa,
for their unfailing love, support, and prayers,
which are truly beyond words to thank.

Acknowledgements

First and foremost, I would like to express my sincerest thanks to my major advisor, Professor J.D. Callen, for his support, advice, and patience during my graduate study. His ideas and suggestions were always inspiring and proved to be extremely helpful. I also wish to thank Professor S.C. Prager for originally suggesting this project and his continuing enthusiasm in this work.

I am very grateful to Professor Callen for giving me the opportunities to work with the resistive MHD group of Oak Ridge National Laboratory. I wish to acknowledge a number of helpful discussions and constructive criticism that I received from all the members of the group there. Especially helpful were Drs. B.A. Carreras and L. Garcia who patiently spent a considerable amount of time with me in the early stage of my code development. I also appreciate an additional computer time allocation I was given from ORNL when the computer time at the University of Wisconsin was extremely limited.

Many people in the Wisconsin Plasma Group in the past and at present have contributed to my research in different ways either directly or indirectly. I wish to thank them all. However, in addition to Professors Callen and Prager, there are several people who deserve special recognition.

I am indebted to Zuoyang Chang for helping me analyze

my numerical results with the magnetic field line tracing code TUBE. His hard work led us to intriguing observations regarding magnetic field stochasticity or the lack of it in a divertor geometry.

I wish to give special thanks to Rick Moyer for providing me with exciting experimental results on the Tokapole II and discussing with me interpretations of my code results in relation to his experiment. The enormous amount of data that was collected and analyzed by Rick and Drs. Tom Osborne and Nancy Brickhouse has always been a major impetus for this research.

I would also like to thank Dr. Mark Carter for helping me learn to use the MFE computers, Darrell Skinner for helping me develop a good programming style, and Bill Ho for numerous conversations and discussions about computers in general as well as plasma physics. I also give thanks to Drs. Joe Johnson and John Santarius for accommodating my special requests for additional computer time.

In order to make maximum use of the limited computer time available, I routinely had to keep very long and odd hours including weekends and holidays when the computers were relatively underutilized. On a more personal note, I wish to offer my sincere gratitude to my wife, Yoshiko, and daughter, Mari, for their unfailing support and understanding. I also wish to thank my relatives for their support.

This work has been supported by the United States Department of Energy.

NUMERICAL SIMULATIONS OF RESISTIVE MAGNETOHYDRODYNAMIC INSTABILITIES IN A POLOIDAL DIVERTOR TOKAMAK

Eijiro Uchimoto

Under the supervision of Professor James D. Callen

A new 3-D resistive MHD initial value code RPD has been successfully developed from scratch to study the linear and nonlinear evolution of long wavelength resistive MHD instabilities in a square cross-section tokamak with or without a poloidal divertor. The code numerically advances the full set of compressible resistive MHD equations in a toroidal geometry, with an important option of permitting the divertor separatrix and the region outside it to be in the computational domain. A severe temporal step size restriction for numerical stability imposed by the fast compressional waves was removed by developing and implementing a new, efficient semi-implicit scheme extending one first proposed by Harned and Kerner. As a result, the code typically runs faster than that with a mostly explicit scheme by a factor of about the aspect ratio. The equilibrium input for RPD is generated by a new 2-D code EQPD that is based on the Chodura-Schlüter method.

The RPD code, as well as the new semi-implicit scheme, has passed very extensive numerical tests in both divertor and divertorless geometries. Linear and nonlinear simulations in a divertorless geometry have reproduced the standard, previously

known results. In a geometry with a four-node divertor the m=2, n=1 (2/1) tearing mode tends to be linearly stabilized as the q=2 surface approaches the divertor separatrix. However, the m=1, n=1 (1/1) resistive kink mode remains relatively unaffected by the nearness of the q=1 surface to the divertor separatrix. When plasma current is added to the region outside the divertor separatrix, the 2/1 tearing mode is linearly stabilized not by this current, but by the profile modifications induced near the q=2 surface and the divertor separatrix. A similar stabilization effect is seen for the 1/1 resistive kink mode, but to a lesser extent. Nonlinear runs of the 2/1 tearing mode suggest saturation of the 2/1 magnetic island. For the nonlinear 1/1 mode, partial reconnection of the 1/1 island has been observed for one equilibrium. All these numerical results compare favorably with the Wisconsin Tokapole II experiments.

Approved:

March 9, 1988 — James D. Callen

Date — Professor James D. Callen
Department of Physics

Table of Contents

Chapter 1. INTRODUCTION

1-1. Motivation for Research

Most tokamaks in the world are designed and built to be stable against virulent ideal magnetohydrodynamic (MHD) instabilities in their normal operational ranges. When a small but finite resistivity is added to the ideal MHD plasma, a new class of instabilities known as resistive MHD instabilities[1] come into existence. Although such instabilities grow on a much slower time scale that is a hybrid of the rapid Alfvén transit and the very slow resistive diffusion time scales, they have profound effects on the evolution of the magnetic field structure and confinement of plasma.[2] With finite resistivity the magnetic field lines are no longer frozen into the plasma. As a result, the magnetic field lines are allowed to break and reconnect to form magnetic islands in the vicinity of singular layers where helical perturbations resonate with the equilibrium magnetic field. (See Fig. 1-1.)

When a magnetic island develops, it changes the magnetic topology in which plasma transport occurs;[2] the thermal insulation quality of the magnetic field disappears significantly in the region of the magnetic island. Still worse, an overlap of magnetic islands of incommensurate helicity leads to stochasticity of the magnetic field lines and a loss of plasma confinement.[2,4] It is not surprising, therefore, that tokamak

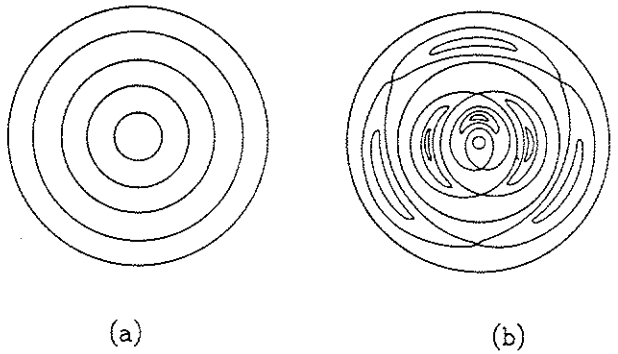

Fig. 1-1. Schematic cross sections of (a) simply nested magnetic flux surfaces and (b) magnetic flux surfaces with magnetic islands.[3] The magnetic flux surface is tangent to magnetic field line(s) everywhere.

discharges often exhibit macroscopic MHD behavior that can be attributed to the resitive MHD instabilities.

Resistive tearing modes, which are the resistive counterparts of current driven ideal kink modes, are believed to be at least partially responsible for three kinds of macroscopic MHD phenomena observed in tokamak discharges: Mirnov oscillations,[5] the sawtooth oscillations,[6] and major disruptions.[7]

Mirnov oscillations are small poloidal magnetic field oscillations detected at the edge of the plasma in the steady state of a tokamak discharge. (The words 'poloidal' and 'toroidal' refer to the short way around and the long way around a

toroid, respectively.) During the initial current ramp-up a sequence of oscillations with discrete and decreasing poloidal mode numbers is observed as the plasma column shrinks. This usually starts with the poloidal mode number m > 6 and decreases to m = 2 by the time the current flat top of a discharge is reached. The magnetic perturbations were found to be resonant with the equilibrium magnetic field that is helical and the pattern rotates approximately at the electron diamagnetic drift frequency. Furthermore, the plasma confinement time was shown to decrease as the magnetic perturbation amplitude increases. Mirnov osillations are interpreted to be a manifestation of nonlinearly saturated magnetic islands generated by the resistive tearing modes that rotate at the electron diamagnetic drift frequency.[8,9] The Mirnov signal is usually dominated by an m=2,n=1 magnetic island (n is the toroidal mode number) and it is sometimes accompanied by an m=3,n=1 magnetic island.

Sawtooth oscillations refer to a wide range of repetitive relaxation oscillations observed in the soft X ray signal and/or electron temperature measurements from the central core of the plasma. Each sawtooth basically consists of a slowly rising phase where the plasma center is Ohmically heated and an abrupt drop phase where the heat rapidly redistributes itself over the central region of the plasma. Unfortunately, there is not a simple unified theoretical model presently available that

accounts for all the features of different types of sawteeth.[10] The standard model,[11-13] however, can explain most features of classical sawteeth where significant precursor oscillations are observed prior to the sawtooth crash and the safety factor q in the central region returns to above unity after the crash. (q is the ratio of the toroidal winding number to the poloidal winding number of a magnetic field line.) In this model the precursor oscillations are thought to be a manifestation of a rotating m=1,n=1 magnetic island that was generated by the m=1,n=1 resistive kink mode. This mode is linearly unstable when the q value on the magnetic axis becomes less than unity as the central region is heated preferentially and the plasma current concentrates there. Unlike the m=2,n=1 magnetic island, the m=1,n=1 island does not saturate nonlinearly in a standard tokamak but grows until it completely takes over the central region including the original magnetic axis.[14,15] When this topological flip takes place, the heat is removed from the plasma center and deposited in the region outside the original q=1 surface where the plasma is colder. As a result, the plasma temperature in the central region suddenly drops, which we perceive to be a sawtooth crash.

The major disruption is an abrupt expansion of the temperature and current profiles that leads to an abnormal termination of the tokamak discharge. It is accompanied by a sudden inward shift of the plasma column, a very large

negative voltage spike and a loss of runaway electron confinement. The standard theoretical picture[16-18] of the major disruption includes a nonlinear destabilization of m=5, n=3 tearing mode in addition to the nonlinear growth of m=2, n=1 and m=3, n=2 tearing modes. The m=2, n=1 and m=3, n=2 islands are usually well separated spatially even late in the nonlinear phase, but their nonlinear evolution results in the steepening of the current profile of the intervening region. This destabilizes the m=5, n=3 tearing mode and eventually leads to an explosive growth of all three modes as the three sets of islands begin to overlap. With an excitation of a number of satellite islands particularly when toroidal coupling effects are included, a very large portion of the plasma volume suddenly turns into a stochastic sea of the magnetic field lines and the major disruption takes place.

At the Physics Department of the University of Wisconsin-Madison a series of experiments have been conducted to study the macroscopic MHD behavior of a poloidal divertor tokamak. The device used in this work is the Wisconsin Tokapole II,[19] a four node poloidal divertor tokamak with a square cross section. (See Figs. 1-2 and 1-3.) The cross section of the vacuum vessel is 44 cm x 44 cm and the major radius is 50 cm. Typical plasma parameters are as follows. The electron temparature is 80-150 eV, ion temperature 40-70 eV, electron and ion densities 5×10^{12} - 1×10^{13} cm^{-3}, toroidal magnetic field

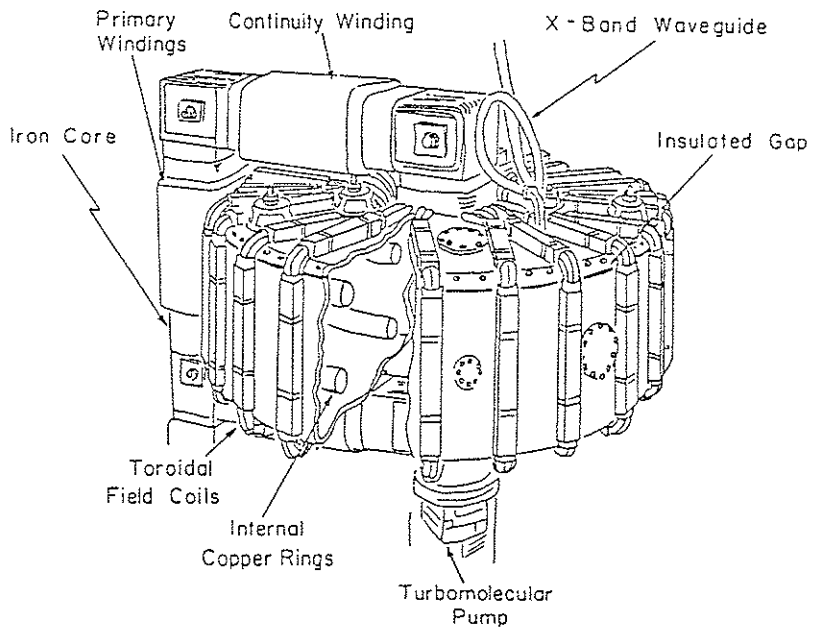

Fig. 1-2. Schematic illustration of the Wisconsin Tokapole II.

3-5 kG, plasma current 15-30 kA, plasma beta (ratio of thermal pressure to magnetic energy density) 0.1-0.4 percent, magnetic Reynolds number (ratio of resistive diffusion time to Alfvén transit time) 5×10^{3}-1×10^{4} and discharge length 4-10 msec. Unlike most other poloidal divertor tokamaks (e.g., ASDEX,[20] DIVA,[21] PDX[22] which is now known as PBX), the divertor rings of the Tokapole II are placed not too close to the wall and

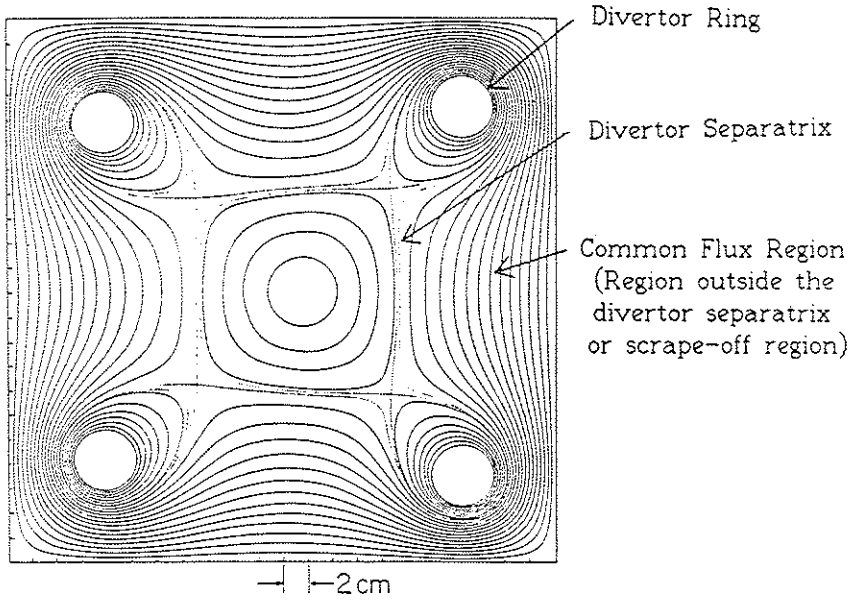

Fig.1-3. Contour plot of poloidal magnetic flux surfaces on a constant toroidal angle plane.

a considerable amount of the magnetic flux is present outside the divertor separatrix. The currents in the divertor rings are inductively driven. One very interesting feature of this device is that the MHD behavior can be studied over a wide range of q values.[23-30] In addition, discharges can be obtained with and without plasma current outside the divertor separatrix

depending on the position of retractable scrape-off plates. The two operational modes are referred to as the magnetic and material limiter discharges, respectively. Key experimental results are summarized in Fig.1-4.[23-30] There are at least two points that deserve special attention. They are both favorable features from the viewpoint of effective tokamak operation but they do not agree with the results of the standard theoretical models for circular cross-section divertorless tokamaks.

1) Low q discharges (q on the magnetic axis as low as 0.5) can be obtained in both magnetic and material limiter discharges. Despite sawtooth oscillations the q value on the magnetic axis does not return to unity after the crash.
2) The major disruption does not take place in magnetic limiter discharges regardless of the volume averaged q inside the divertor separatrix.

A major stimulus for the research in this thesis was to develop theoretical tools to aquire an understanding of these two important characteristics of Tokapole II operation.

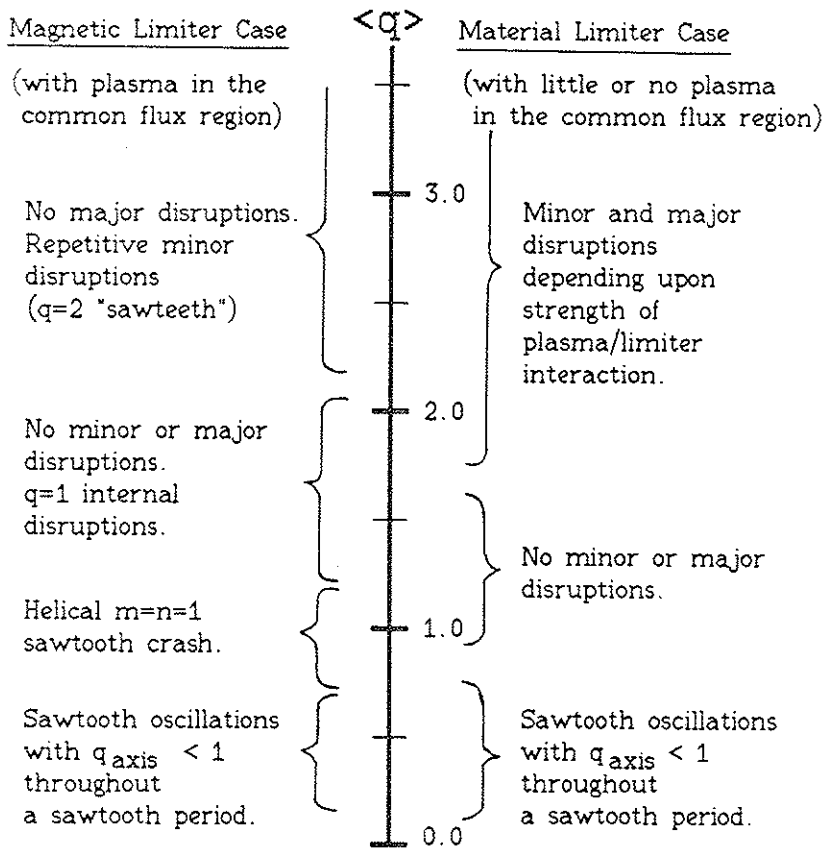

Fig. 1-4. Summary of long wavelength MHD activity in the Wisconsin Tokapole II.[23-30] <q> is the q at the edge of a uniform current circular plasma with the same current and roughly the same cross sectional area as the actual discharge. For the magnetic limiter case m=2, n=1 modes are present for $\langle q \rangle \gtrsim 2.2$ and m=1, n=1 modes for $\langle q \rangle \lesssim 2.2$. For the material limiter case the dividing line between these two different types of macroscopic modes is $\langle q \rangle \sim 1.7$.

1-2. Objectives and Overview of Research

One of the ultimate goals of theoretical research in fusion plasma physics is to conceive of a theoretical model that can explain a wide range of experimental data and guide the development of future devices. When an apparent conflict between theory and experiment is discovered, the applicability of an existing theoretical model to such an experiment needs to be reevaluated.

Existing theoretical models for Mirnov oscillations, the sawtooth oscillations, and the major disruption were originally developed for a cylindrical model of a tokamak (no toroidal effect) with a circular cross section. The plasma is assumed to be in the collisional regime where the resistive MHD equations are applicable. The magnetic Reynolds number of a typical Tokapole discharge is of order 10^4 and neoclassical corrections[31] to resistive MHD are small because of the fairly collisional (plateau or Pfirsch-Schlüter regime) plasma. On the other hand, the very large geometric deviations from a straight circular cylinder due to the poloidal divertor should definitely be taken seriously. Flux surfaces become highly noncircular as we move away from the magnetic axis to the divertor separatrix. The region outside the divertor separatrix or the common flux region has a strong multipole character. In fact, it is not possible to map the Tokapole geometry onto a standard tokamak geometry because of a non-simply connected boundary

condition due to the divertor rings. The linear and nonlinear evolution of resistive instabilities in such a configuration could be significantly different. A high magnetic shear near the divertor separatrix and the presence of a plasma in the common flux region could modify the linear growth rate. Interactions of magnetic islands with the divertor separatrix could lead to considerable stochasticity before the total reconnection of an m=1, n=1 island and the saturation of an m=2, n=1 island. To investigate such effects, it is essential to include the region outside the divertor separatrix and the separatrix itself in resistive MHD simulations.

At the time this research was started several years ago, however, a computer code that was suited for this purpose did not exist. Resistive MHD simulations in a poloidal divertor tokamak were limited to the region inside the divertor separatrix.[32] This stemed from the fact that most previously written major resistive MHD initial value codes for production runs employed a spectral representation in both the poloidal and toroidal directions. A two dimensional (2-D) spectral representation would require a very large number of poloidal Fourier harmonics to describe an axisymmetric equilibrium of the Tokapole II magnetic geometry including the divertor rings.

Despite such a shortcoming, the HIB code[33,34] was used to simulate the nonlinear evolution of the m=1, n=1 resistive kink mode including a portion of the divertor separatrix by

placing the divertor rings just outside a circular boundary.[24] The simulation demonstrated that the interaction of the m=1, n=1 island and the divertor separatrix indeed leads to stochasticity. This work, however, was limited in that the divertor rings were not included in the computational domain, plasma in the common flux region was not included, and the reduced MHD model[35] was employed. The reduced MHD model is not suitable for studying low q discharges because the ordering assumptions in this model break down when q is considerably smaller than unity.

To overcome such limitations we have developed from scratch a new three dimensional (3-D), compressible, full resistive MHD initial value code RPD[36,37] (Resistive MHD code for a Poloidal Divertor tokamak). To handle the complicated geometry the dependent variables are written in a finite difference form in the two Cartesian directions of a constant toroidal angle plane. They are, however, Fourier analyzed in the toroidal direction to facilitate efficient mode representations.

The code is toroidal and can be run with or without a poloidal divertor. A severe step size restriction for numerical stability imposed by the fast compressional mode is removed by a new, efficient semi-implicit scheme[37] based on that proposed by Harned and Kerner.[38] Axisymmetric MHD equilibria for the resistive MHD simulations are generated by a new 2-D equilibrium code EQPD[39] (MHD EQuilibrium code for a Poloidal

Divertor tokamak) that utilizes the basic features of the Chodura-Schlüter method.[40]

The newly developed 'resistive MHD package' that consists of the 2-D Chodura-Schlüter code EQPD and the 3-D resistive MHD initial value code RPD is written in FORTRAN 77 and designed to run efficiently on the supercomputers that use the Cray Time Sharing System (CTSS). They include the Cray-1 (C machine), Cray-1S (D machine), Cray X-MP/24 (E machine), and Cray-2 (B machine) of the National Magnetic Fusion Energy Computer Center(NMFECC) at Lawrence Livermore National Laboratory(LLNL) and the Cray X-MP/48 (A machine) of the San Diego Supercomputer Center(SDSC) at the University of California-San Diego.

Our RPD code has passed very extensive, if not exhaustive, numerical tests both linearly and nonlinearly in a divertorless tokamak with a square cross section.[37] Particular attention is paid to checking the integrity of the new semi-implicit scheme. In the course of this study a number of standard theoretical results are reproduced.

The RPD code has also passed numerical tests in a poloidal divertor geometry.[37,41] The new semi-implicit scheme is shown to be a simple but quite powerful method to improve the code efficiency in the divertor geometry as well. The effects of the divertor separatrix and the plasma current in the common flux region on the linear and/or nonlinear resistive MHD

instabilities are studied.[37,41-43] The m=2,n=1 tearing mode tends to be linearly stabilized when the q=2 surface is brought close to the divertor separatrix. On the other hand, the m=1,n=1 resistive kink mode remains linearly unstable regardless of the nearness of the q=1 surface to the divertor separatrix. The addition of a plasma current outside the divertor separatrix tends to stabilize strongly the linear m=2,n=1 mode and modestly the linear m=1,n=1 mode. This is due to a profile modification near the mode rational surface but not due to the mere presence of the current outside. Nonlinear results, which are still preliminary in nature, suggest that the m=1,n=1 magnetic island may not totally reconnect but instead saturate for at least one divertor equilibrium. The m=2,n=1 magnetic island may become stochastic before saturation. Although a complete understanding of Tokapole discharges would undoubtedly require inclusion of other effects such as thermal transport and impurities, resistive MHD simulation results so far compare favorably with the Tokapole II experiments.

1-3. Organization of Thesis

This thesis is organized as follows. Chapter 2 deals with our work on axisymmetric MHD equilibria of noncircular and poloidal divertor tokamaks. This is an important prerequisite for conducting resistive MHD simulations in such devices.

Chapter 3 describes the details of the 3-D resistive MHD initial value code RPD, the main tool that was developed and used in this thesis research. Also described in this chapter is the new, efficient semi-implicit scheme that was developed and implemented to improve the code efficiency. Chapter 4 presents the linear and nonlinear simulation results of the m=2, n=1 resistive tearing mode and the m=1, n=1 resistive kink mode in a divertorless geometry. The primary purposes of this chapter are to demonstrate the correctness of our RPD code and the accuracy of the new, efficient semi-implicit scheme. Chapter 5 presents the linear and nonlinear simulation results of the m=2, n=1 and m=1, n=1 modes in a poloidal divertor geometry. The ramifications of our numerical results for the interpretation of Tokapole II experiments are also briefly discussed. Chapter 6 summarizes what we have accomplished in this research. We also make suggestions for future research.

Chapter 2. IDEAL MHD EQUILIBRIUM

2-1. Introduction

Before embarking on the resistive MHD studies we need to generate a family of axisymmetric MHD equilibria. It is to this equilibrium state that a helical magnetic perturbation is added. Once the axisymmetry is broken, the tearing and/or resistive kink modes will develop in the resistive MHD plasma provided that the equilibrium is unstable to such modes.

Because of the highly nonlinear nature of the MHD equilibrium problem compounded by geometries that lack sufficient symmetry, an analytic solution is not possible in general for noncircular and poloidal divertor tokamaks. We therefore turned to a numerical approach. We have developed from scratch an axisymmetric equilibrium code EQPD that adopts the basic features of the Chodura-Schlüter method.[40] This method was perceived as being able to handle effectively a geometry with multiple magnetic axes; the multiple-valuedness of flux quantities need be considered only in the initialization procedure. Unfortunately, significant spurious numerical oscillations in the current density were observed in the vicinity of the divertor rings and the divertor separatrix. This problem was overcome partially by introducing a small but finite resistivity[39] in the Chodura-Schlüter method. A simpler version of EQPD without a poloidal divertor calculates an

axisymmetric MHD equilibrium for a square cross-section divertorless tokamak over a wide range of plasma beta (ratio of thermal pressure to magnetic energy). The resistivity term is not required in this case.

In this chapter we first present two methods for computing an axisymmetric MHD equilibrium. We then describe the EQPD code that was used to generate input files for resistive MHD studies. The test results of the code are also given.

2-2. Methods of Solution for Axisymmetric MHD Equilibria

2-2-1. Direct solution of the Grad-Shafranov equation

A plasma in a static MHD equilibrium state is described by the set of time independent, flow-free ideal MHD equations:

$$\mathbf{J} \times \mathbf{B} = \nabla P \,, \tag{2.1}$$

$$\nabla \times \mathbf{B} = \mu_o \mathbf{J} \,, \tag{2.2}$$

$$\nabla \cdot \mathbf{B} = 0 \,, \tag{2.3}$$

where $\mathbf{B}$ is the magnetic field, $\mathbf{J}$ the current density, P the thermal pressure, and μ_o the magnetic permeability. Eq. (2.3) suggests that if the plasma geometry possesses a symmetry (translational, axial or helical), a stream function can be introduced to describe the magnetic field. In the case of an axisymmetric torus, this leads to the well known Grad-Shafranov equation:[44,45]

$$\Delta^* \psi = - \mu_o R^2 \frac{dP}{d\psi} - I \frac{dI}{d\psi} \,, \tag{2.4}$$

where $\Delta^* \equiv R \frac{\partial}{\partial R} \frac{1}{R} \frac{\partial}{\partial R} + \frac{\partial^2}{\partial y^2}$.

Here, ψ and I are the poloidal flux and poloidal current functions, respectively, which are related to the magnetic field by the relations

$$\mathbf{B} = \nabla \times (\psi \hat{\zeta}) + \frac{I}{R} \hat{\zeta} \,, \tag{2.5}$$

$$I(\psi) \equiv R B_\zeta \,, \tag{2.6}$$

where $\hat{\zeta}$ is a unit vector in the toroidal direction. The coordinate system used is the cylindrical coordinate system (R, y, ζ) with the angular variable taken to be in the toroidal direction. It is shown in Fig. 2-1.

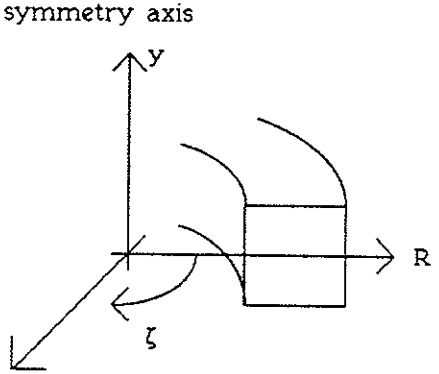

Fig. 2-1. Coordinate system used for an axisymmetric torus.

The solution of the Grad-Shafranov equation requires a numerical approach in general because $P = P(\psi)$ and $I = I(\psi)$; the equation becomes highly nonlinear unless unrealistically simple functional forms are chosen for P and I.

In the direct approach[46-48] the Grad-Shafranov equation is solved for ψ in the two Cartesian variables R and y. (This contrasts with the moment approach[49] in which Eq.(2.4) is transformed to and solved in flux surface variables. Although the moment approach is the fastest computational method available for a divertorless tokamak equilibrium, it is not suitable for a poloidal divertor tokamak in which P and I are multiple-valued functions of ψ.) To solve for ψ, the functional forms of $P=P(\psi)$ and $I=I(\psi)$ are usually specified first. After making a reasonable choice for the initial $\psi = \psi^1(R,y)$, we solve Eq.(2.4) iteratively for $\psi = \psi^n(R,y)$. The simplest iteration method is the Picard iteration scheme:

$$-\Delta^*\psi^{n+1}(R,y)=g(R,\psi^n(R,y)), \qquad (2.7)$$

where g is the right side of Eq.(2.4) and the superscript denotes the iteration level. To prevent ψ from converging to a physically uninteresting solution, we impose a constraint such as a constant total toroidal current during the iterations. The matrix that results from having to invert the Δ^* operator in each iteration step is solved with a fast solver for a sparse matrix, usually by either the SOR(successive over-relaxation) or the ICCG(incomplete Choleski conjugate gradient) method.

A code of this type (TOPEC) was developed by M.W. Phillips[50] for studying axisymmetric MHD equilibria in the Wisconsin Tokapole II. Although the code has been used quite extensively to interpret the experimental results, it is limited in that plasma current and pressure were excluded from the region outside the divertor separatrix. This is not a fundamental limitation of the direct Grad-Shafranov solver and TOPEC can in principle be modified to include such effects.[24]

2-2-2. The Chodura-Schlüter method

An alternative approach to the ideal MHD equilibrium problem is to treat it as a minimization problem for the plasma potential energy $W = \int d^3x\,[B^2/2\mu_0 + P/(\Gamma-1)]$, where Γ is the ratio of specific heats. This approach is particularly useful for a general 3-D configuration in which there are no symmetries.

Chodura and Schlüter[40] proposed an iteration scheme using a spatially fixed Eulerian grid that brings a plasma of an arbitrary configuration to a stationary state $\delta W=0$ subject to the constraints of magnetic flux and mass conservation. Consider the ideal MHD equations:

$$\rho \frac{d\mathbf{v}}{dt} = \frac{1}{\mu_0}(\nabla \times \mathbf{B}) \times \mathbf{B} - \nabla P \ , \qquad (2.8)$$

$$\frac{\partial \mathbf{B}}{\partial t} = \nabla \times (\mathbf{v} \times \mathbf{B}) \ , \qquad (2.9)$$

$$\nabla \cdot \mathbf{B} = 0 \ , \qquad (2.10)$$

$$\frac{dP}{dt} = - \Gamma P \nabla\cdot\mathbf{v} , \qquad (2.11)$$

$$\frac{\partial \rho}{\partial t} + \nabla\cdot(\rho\mathbf{v}) = 0 , \qquad (2.12)$$

where $d/dt = \partial/\partial t + (\mathbf{v}\cdot\nabla)$, ρ is the mass density, and $\mathbf{v}$ is the flow velocity. In the Chodura-Schlüter method the inertial response $\rho(d\mathbf{v}/dt)$ in the momentum balance equation is replaced by a frictional response $\alpha\,\mathbf{v}$, where α is a positive number, function or operator. This gives rise to the MHF (magneto-hydro-friction) model of a plasma. The time t should now be regarded as a relaxation parameter. Since the friction force extracts energy from the plasma subject to the constraints of magnetic flux and mass conservation (Eqs. (2.9) and (2.12)), the plasma relaxes into an equilibrium state. Convergence to the stationary state can be accerelated significantly by introducing a conjugate gradient term of the form

$$\mathbf{v}^{t+\Delta t} = \mathbf{F}^{t+\Delta t} + b\,\frac{\langle F^2\rangle^{t+\Delta t}}{\langle F^2\rangle^{t}}\,\mathbf{v}^{t} , \qquad (2.13)$$

where $\mathbf{F} = (1/\mu_o)[(\nabla \times \mathbf{B}) \times \mathbf{B}] - \nabla P$. The superscripts t and $t+\Delta t$ denote the old and new 'time' levels, $\langle\ \rangle$ denotes an average over the entire plasma volume, and b is a numerical constant that is slightly less than unity. The use of the Eulerian grid allows us to treat a geometry with more than one

magnetic axis effectively.

Although the Chodura-Schlüter method was developed with 3-D MHD equilibrium calculations in mind, it can also be used to calculate axisymmetric MHD equilibria. The assumption of axisymmetry reduces a 3-D problem to a 2-D problem on a constant toroidal angle plane. By introducing the poloidal flux function, the divergence-free condition for the magnetic field can be imposed very accurately. Magnetic flux conservation implies that the functional form of the safety factor $q(\psi) = d\phi/d\psi$, where ϕ is the toroidal flux function, is preserved in the Chodura-Schlüter method. (This is an alternative expression for q that was defined to be the ratio of the toroidal winding number to the poloidal winding number in chapter 1.) The poloidal current function $I(\psi)$, which is difficult to guess, need not be prespecified; it comes out numerically as an output of the code. Furthermore, the multiple-valuedness of $P(\psi)$ and $q(\psi)$ in a poloidal divertor geometry need not be considered except for the initialization step.

2-3. Description of the 2-D Chodura-Schlüter Code EQPD

In this section we describe key features of our EQPD code that calculates axisymmetric MHD equilibria for square cross-section tokamaks with and without a poloidal divertor.

The code employs a 2-D version of the Chodura-Schlüter method which uses the conjugate gradient iteration scheme.

By introducing the poloidal flux function ψ and the poloidal current function I, as defined in Eqs. (2.5) and (2.6), the set of 2-D equations can be written in the numerically convenient form

$$F_R = -\frac{1}{R^2}\frac{\partial\psi}{\partial R}\Delta^*\psi - \mu_o\frac{\partial P}{\partial R} - \frac{1}{R^2}I\frac{\partial I}{\partial R}\,, \qquad (2.14)$$

$$F_y = -\frac{1}{R^2}\frac{\partial\psi}{\partial y}\Delta^*\psi - \mu_o\frac{\partial P}{\partial y} - \frac{1}{R^2}I\frac{\partial I}{\partial y}\,, \qquad (2.15)$$

$$v_R^{t+\Delta t} = F_R^{t+\Delta t} + b\,\frac{<F^2>^{t+\Delta t}}{<F^2>^t}\,v_R^t\,, \qquad (2.16)$$

$$v_y^{t+\Delta t} = F_y^{t+\Delta t} + b\,\frac{<F^2>^{t+\Delta t}}{<F^2>^t}\,v_y^t\,, \qquad (2.17)$$

$$\frac{\partial\psi}{\partial t} = \left[\frac{\partial}{\partial R}(\psi v_R) + \frac{\partial}{\partial y}(\psi v_y)\right] + \psi\left(\frac{\partial v_R}{\partial R} + \frac{\partial v_y}{\partial y}\right) + \eta_\zeta\Delta^*\psi\,, \qquad (2.18)$$

$$\frac{\partial}{\partial t}\left(\frac{I}{R}\right) = -\left[\frac{\partial}{\partial R}\left(\frac{I}{R}v_R\right) + \frac{\partial}{\partial y}\left(\frac{I}{R}v_y\right)\right]\,, \qquad (2.19)$$

$$\frac{\partial P}{\partial t} = \left[\frac{\partial}{\partial R}(Pv_R) + \frac{\partial}{\partial y}(Pv_y)\right] + P\left(\frac{\partial v_R}{\partial R} + \frac{\partial v_y}{\partial y}\right)\,, \qquad (2.20)$$

where Δ^* is the elliptic differential operator of the Grad-Shafranov equation (Eq. (2.4)) and $<F^2> = <F_R^2+F_y^2>$ is the average over a constant toroidal angle plane. The toroidal resistivity η_ζ is added to the poloidal flux advancement equation (Eq. (2.18)) as an option. This tends to smooth numerical ripples of the toroidal current density in the vicinity of the

divertor rings and the divertor separatrix.

The plasma pressure P is convected according to Eq. (2.20). (The right side of this equation is $-\mathbf{v}\cdot\nabla P$ in a constant toroidal angle plane.) As a result, the 'time' advancement equations for ψ and P assume the same form provided that $\eta_\zeta = 0$. It follows that the functional form $P(\psi)$ will be preserved throughout this calculation. Also preserved when $\eta_\zeta = 0$ is the functional form of $q(\psi)$ because all magnetic fluxes are convected by a perfectly conducting fluid. On the other hand, the poloidal current function $I(R,y)$ may deviate significantly from a function of ψ during the iteration process since its 'time' evolution equation is not convective. As the plasma evolves into a stationary state ($\mathbf{F}\to 0$ and $\mathbf{v}\to 0$), however, the poloidal current function I should become a function of ψ and Eqs. (2.14) and (2.15) then reduce to the Grad-Shafranov equation.

The vacuum vessel and the divertor rings are assumed to be perfect conductors. The poloidal flux function ψ at the boundaries is frozen in 'time'. The velocity $\mathbf{v}$ at the boundaries is set equal to zero, which is consistent with the final state of a static MHD equilibrium. Furthermore, the pressure P is assumed to vanish at the boundaries.

Our EQPD code numerically advances the dependent variables ψ, I, P, v_R, and v_y. The numerical procedure proceeds as follows. Eqs. (2.14) and (2.15) are used to calculate the ficticious force $\mathbf{F}$. The force is related to a new

velocity by using the conjugate gradient scheme given by Eqs. (2.16) and (2.17). This new velocity is then used in Eqs. (2.18)-(2.20) to advance ψ, I, and P. In doing so, the left side of the equation is discretized as $(f^{t+\Delta t} - f^{t})/\Delta t$, where f is ψ, I/R or P. We then go back to Eqs. (2.14) and (2.15) to start a new iteration loop. The iteration loop is repeated until the fictitious force **F** becomes sufficiently small and the poloidal current function I converges to a function of ψ.

In the code Eqs. (2.14)-(2.20) are finite differenced in R and y. We consider only the upper half of a square cross-section tokamak assuming up-down symmetry. An equally spaced but staggered two dimensional grid is set up on this rectangular region. The way the plasma quantities are placed in a grid cell is shown in Fig. 2-2. All the first and second

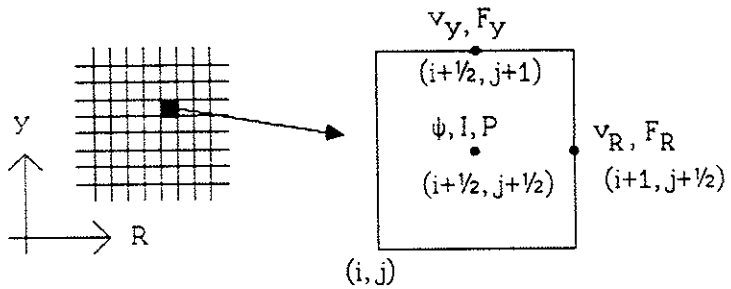

Fig. 2-2. Placement of plasma quantities in a grid cell. i and j are indicies in the R and y directions.

derivative terms with respect to R and/or y are discretized in the standard second-order accurate form taking into account the location at which the quantities are evaluated. The grid is extended one row and one column beyond the physical boundaries and two rows beyond the midplane to efficiently impose the boundary conditions. For simplicity, the cross-section of the divertor ring is assumed to be a square.

Our EQPD code can in principle evolve any axisymmetic MHD plasma to an axisymmetic MHD equilibrium state. To facilitate convergence to a desired state, however, we have developed a separate program SETPD. This program creates an input data file for EQPD as follows. The elliptic differential equation $-\Delta^*\psi = RJ_\zeta$ that relates the poloidal flux function and the toroidal current density is solved first for $\psi \equiv \psi^1$ with a parabolic current distribution peaked at the magnetic axis ($\psi=\psi_{min}$). The matrix inversion is done by using a band-storage direct solver. The same equation is then solved for $\psi \equiv \psi^2$ with a reasonable choice for $J_\zeta = J_\zeta(\psi^1(R,y))$. Upon choosing $I(\psi)$, which we take to be spatially uniform at the beginning of an EQPD run, the functional form $q(\psi)$ is specified. Note that the ψ^2 obtained with SETPD does not in general satisfy the Grad-Shafranov equation for the $P(\psi)$ we choose. We use EQPD to relax ψ, P, and I to satisfy the Grad-Shafranov equation while retaining the functional forms of $P(\psi)$ and $q(\psi)$.

The EQPD code creates three output files. One of them is a binary sequential file that can be read by our 3-D resistive MHD initial value code RPD. The second file contains the machine and plasma parameters of the equilibrium. It also prints out various plasma quantities at all the grid points. The third file is a graphic file and it consists of the contour level plots of $\psi(R,y)$, $P(R,y)$, $I(R,y)$, and $J_\zeta(R,y)$, the plots of various plasma quantities on the midplane, and the 'time' evolution plots of the square of the unbalanced ficticious force $|\mathbf{F}|^2$ and the shift of the magnetic axis.

We conclude that we have found an axisymmetric MHD equilibrium when the output meets the following criteria:

1) The contour shapes of ψ, P, and I agree reasonably well (by visual examination) indicating that $P=P(\psi)$ and $I=I(\psi)$.
2) The square of the unbalanced ficticious force decreases by several orders of magnitude and the magnetic axis shift saturates with 'time'.
3) The toroidal current density does not exhibit large numerical ripples in the vicinity of the divertor rings and the divertor separatrix for the case of a poloidal divertor geometry.

2-4. Code Tests

2-4-1. Divertorless tokamak

We first present an example of a divertorless tokamak equilibrium calculated by our EQPD code. The aspect ratio $A_r \equiv R_o/a$ of the device is chosen to be five, where R_o is the major radius (the distance between the symmetry axis and the geometric center of the poloidal cross section) and a is one half the width of the square. Fig. 2-3 shows the contour plots of ψ, P and I. The grid size used in this calculation is 60 by 30.

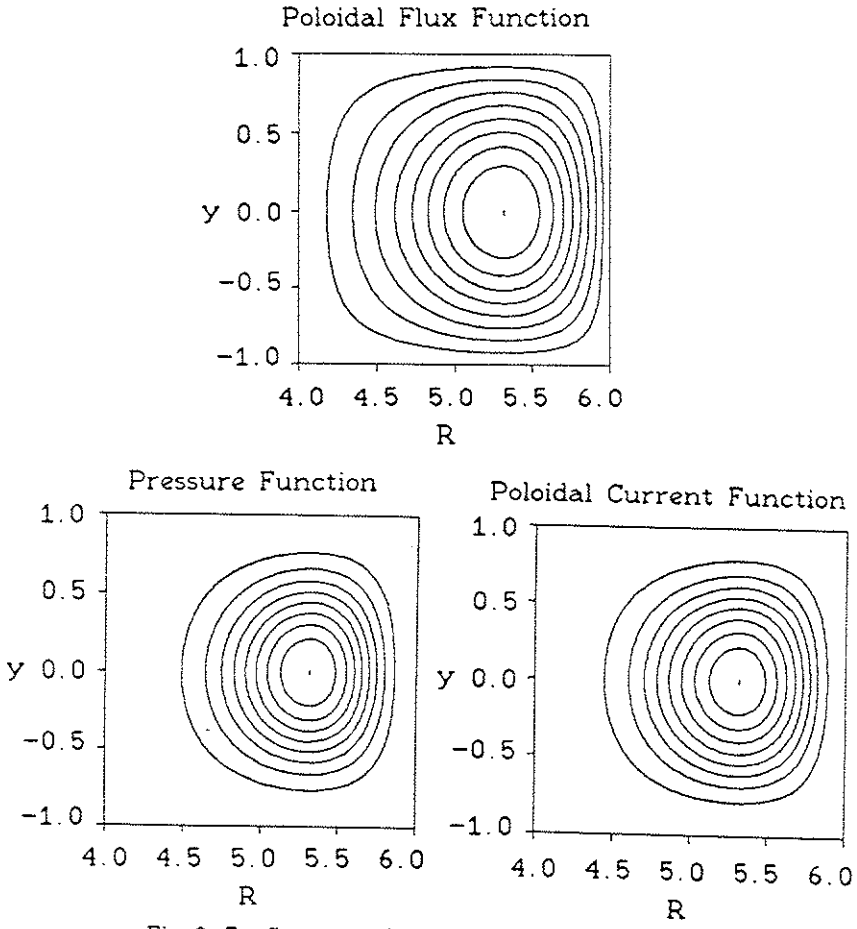

Fig. 2-3. Contour plots of ψ, P, and I.

To better illustrate the global features of the three quantities, the contour levels are equally spaced between their minimum and maximum values. R and y are normalized to a. The pressure is chosen to be proportional to $[(\psi - \psi_{wall})/(\psi_o - \psi_{wall})]^2$ and the peak beta (β_{max}) and the volume-averaged beta ($<\beta>$) are 6.3 and 1.4 percent, respectively. Here, ψ_o and ψ_{wall} are the values of the poloidal flux function on the magnetic axis and the wall. The toroidal current density J_ζ and the q profiles of this equilibrium on the midplane are shown in Fig.2-4. J_ζ is measured in units of $B_{\zeta o}/(a\mu_o)$, where $B_{\zeta o}$ is the toroidal magnetic field on the magnetic axis. The q value on the magnetic axis is chosen to be 1.00. The q value at the wall goes to infinity because the poloidal component of the

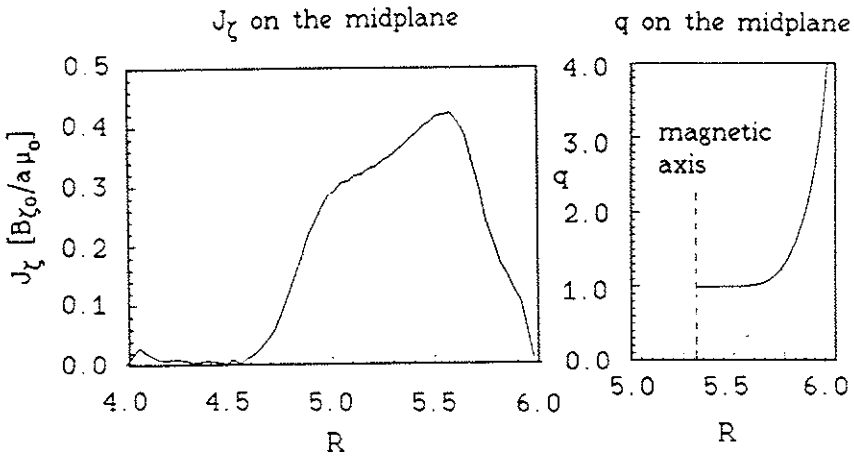

Fig.2-4. J_ζ and q profiles on the midplane. q is plotted only for $R_o \le R \le R_o + a$

magnetic field vanishes at the sharp corners of the square cross-section container that is assumed to be a perfect conductor.

Convergence of the calculations is illustrated in Figs.2-5, 2-6, and 2-7. The two contour plots of Fig.2-5 on the next page compare P and I with ψ. The contour curves for two quantities in each plot are launched from the same points on the midplane of the poloidal cross section. Except for the outermost contours of I and ψ, the three quantities are in good to excellent agreement. A slight discrepancy between I and ψ on the outermost contours should not be taken too seriously because the poloidal current function I is found to be almost constant near the wall. This shows that P and I are indeed functions of ψ for all practical purposes.

Fig.2-6 on page 32 shows the evolution of the square of the unbalanced ficticious force as a function of iteration step number. This quantity diminished by more than five orders of magnitude in 15000 iteration steps with a step size $\Delta t = 0.0001$ and the constant in front of the conjugate gradient term of b= 0.999. When b is reduced to 0.99, it required as many as 50000 iteration steps to reach the same convergence level. On the other hand, a further increase of b closer to unity, say b= 0.9995, resulted in run-terminating numerical instabilities. Fig.2-7 shows the evolution of the shift of the magnetic axis. After about 7500 iteration steps the axis shift seems to saturate as it asymptotically approaches its terminal value.

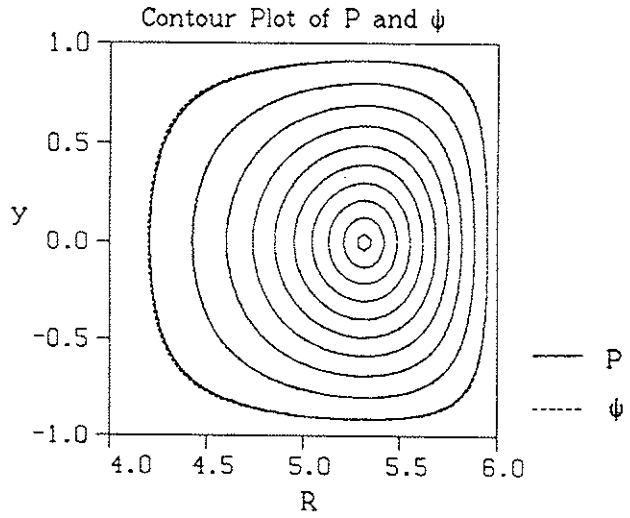

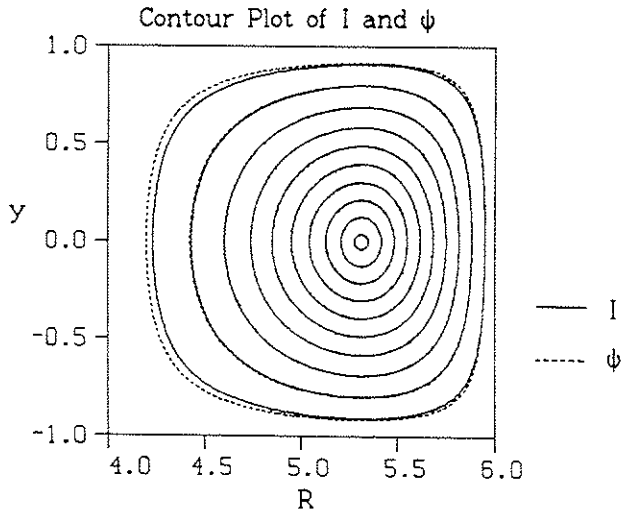

Fig. 2-5. Comparison of P and I with ψ contours.

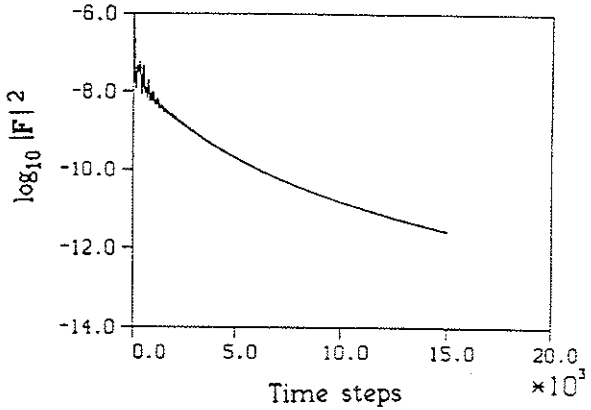

Fig. 2-6. The evolution of the square of the unbalanced ficticious force with iteration number. (b=0.999)

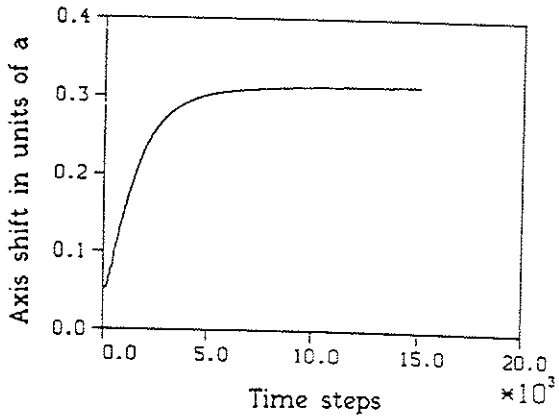

Fig. 2-7. The shift of the magnetic axis in units of a (one half the size of the square cross section) as a function of the iteration number.

To examine the effect of the spatial discretization of the equations on the calculated MHD equilibrium, the EQPD code was run with the same machine and plasma parameters but with three different grid sizes of 20 by 10, 40 by 20, and 60 by 30. In all three cases the shift of the magnetic axis was found to be 0.315a. We conclude that the grid convergence is excellent indicating very good numerics in the code.

To demonstrate the versatility of the code, we changed the plasma pressure while keeping the machine parameters, the pressure profile ($P(\psi)/P_{max}$) and the q profile ($q(\psi)$) unchanged. Here, P_{max} is the plasma pressure on the magnetic axis. Fig. 2-8 shows the effect of a finite plasma beta

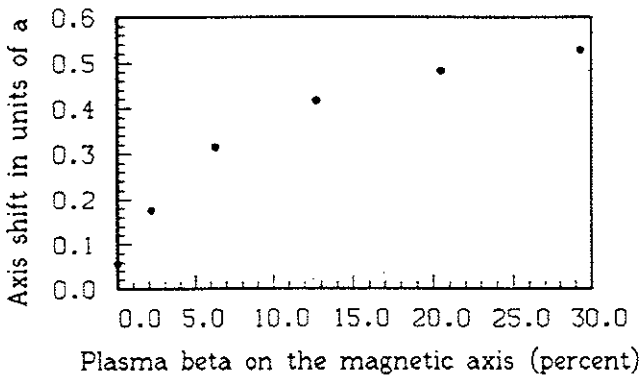

Fig. 2-8. Magnetic axis shift from the geometric center of the poloidal cross section due to finite plasma pressure.

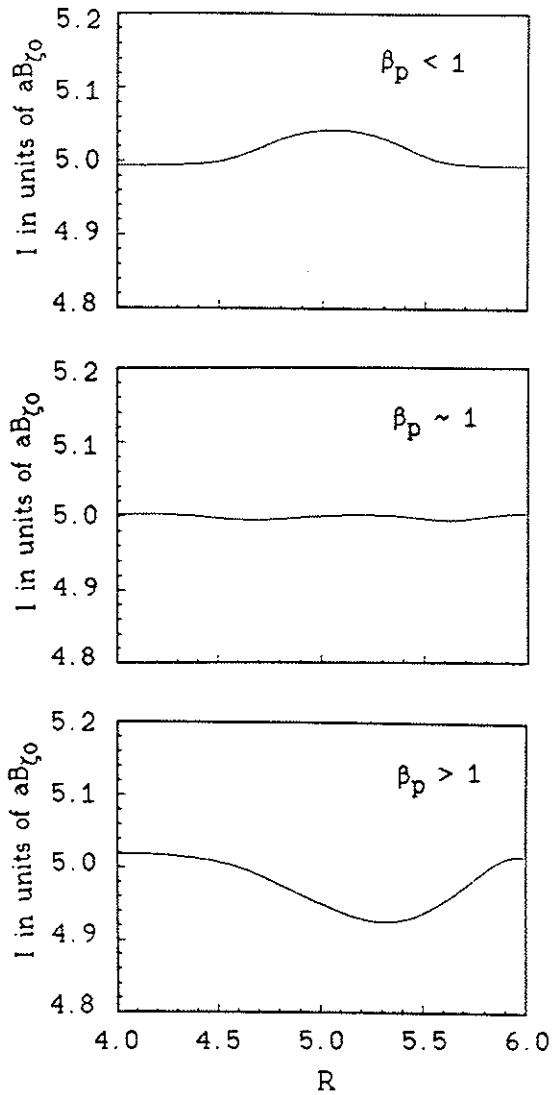

Fig. 2-9. Poloidal current function on the midplane for equilibria with $\beta_p < 1$, $\beta_p \sim 1$, and $\beta_p > 1$.

on the shift of the magnetic axis. At a very low β the axis shift is found to be 0.053a, which is of order $a/A_r^2 = 0.04a$. As the plasma pressure is increased, the magnetic axis is displaced toward the outer edge of the vacuum vessel due to an additional outward force. At a very high β the axis shift approaches its terminal value which is of order a/2. These results are in good agreement with those previously obtained.[46,51-53] In Fig.2-9 on the preceding page, we plot the poloidal current function on the midplane for the three lowest beta cases in Fig.2-8. The second case has poloidal beta β_p ($\sim 2P/B_p^2$, where B_p is the poloidal magnetic field) of about unity. As a result, $I(\psi)$ is almost constant. The first and third cases clearly exhibit the well-known[46] paramagnetic and diamagnetic effects for these $\beta_p < 1$ and $\beta_p > 1$ cases.

It is reasonable to conclude from the above tests, as well as a number of other tests, that our EQPD code works very well for a divertorless tokamak for a wide range of plasma parameters. An example of other tests includes conservation of the functional form of $q(\psi)$ during the iterations, which was found to be satisfactory. As for the code efficiency, a typical run with a 60 by 30 grid takes 30 seconds to 2 minutes of Cray-1 CPU time. The program size is about 600 thousand octal words including graphic routines.

2-4-2. Poloidal divertor tokamak

The EQPD code has been run extensively for a tokamak with a four-node poloidal divertor. The contour plot of ψ in Fig.2-10 is obtained by setting $\eta_\zeta = 0$ as in a divertorless tokamak calculation but subject to an additional constraint that ψ at the divertor rings is fixed. In the plot the contour levels are equally divided between the minimum and maximum values

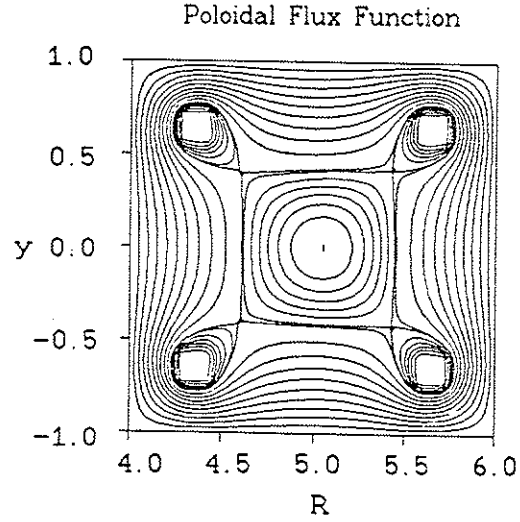

Fig.2-10. Contour plot of ψ. ($\eta_\zeta = 0$)

of ψ in the regions inside and outside the divertor separatrix, respectively. The ratio of poloidal flux inside and outside the divertor separatrix is one to four. R and y are normalized as in a divertorless tokamak. Although the ψ contour plot looks

very smooth, the code failed to converge to a physically meaningful solution. To best illustrate this problem, we present two plots of the toroidal current density J_ζ in Fig.2-11. Serious spurious numerical oscillations that originate from the regions near the divertor rings and the divertor separatrix occupy the bulk of the plasma. This is not surprising because J_ζ involves second derivatives of ψ and even the slightest irreguralities in ψ will show up in J_ζ.

The problem can be alleviated considerably by introducing a small but finite resistivity term in Eq.(2.18). To minimize significant resistive diffusion of the plasma during the iterations, we turn on the resistivity term only after some numerical oscillations begin to develop. Furthermore, η_ζ is chosen so that it rises sharply (by a factor of 100) near the divertor rings.

Fig.2-12 on page 39 shows an approximate MHD equilibrium generated in this way in terms of contour plots of ψ, P and I. The contour levels of P and I are equally divided between their minimum and maximum values, while the contour levels of ψ are chosen in the same way as in Fig.2-10. The peak plasma beta β_{max} is chosen to be 2.0 percent. The volume averaged betas excluding and including the region outside the divertor separatrix are 1.2 and 0.44 percent, respectively. For this particular run, η_ζ at the plasma center is raised from 0.0 to 0.3 [$\mu_0 a^2$/'time'] during the iterations. The grid size is 60 by 30. The toroidal current density thus

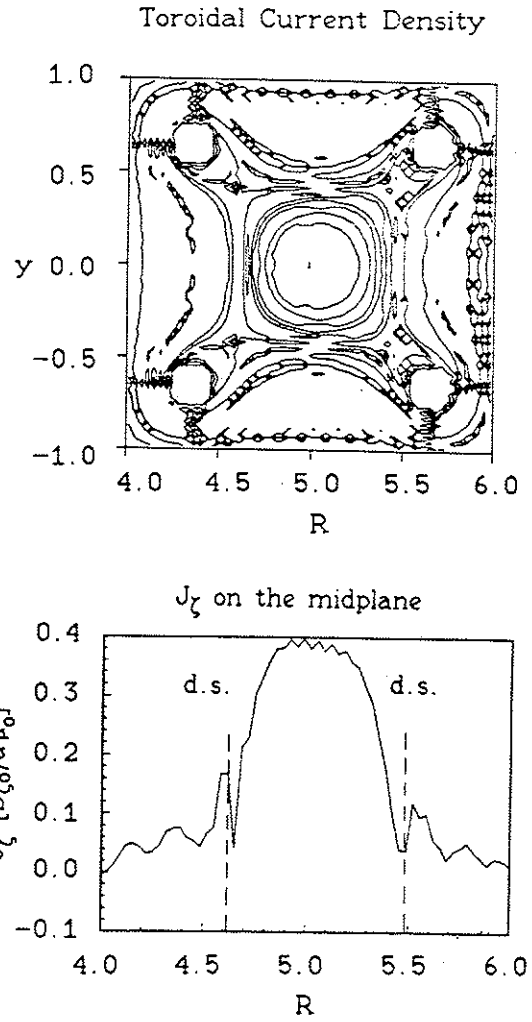

Fig.2-11. Contour plot of J_ζ and the J_ζ profile on the midplane for a run with η_ζ = 0. 'd.s.' denotes the divertor separatrix.

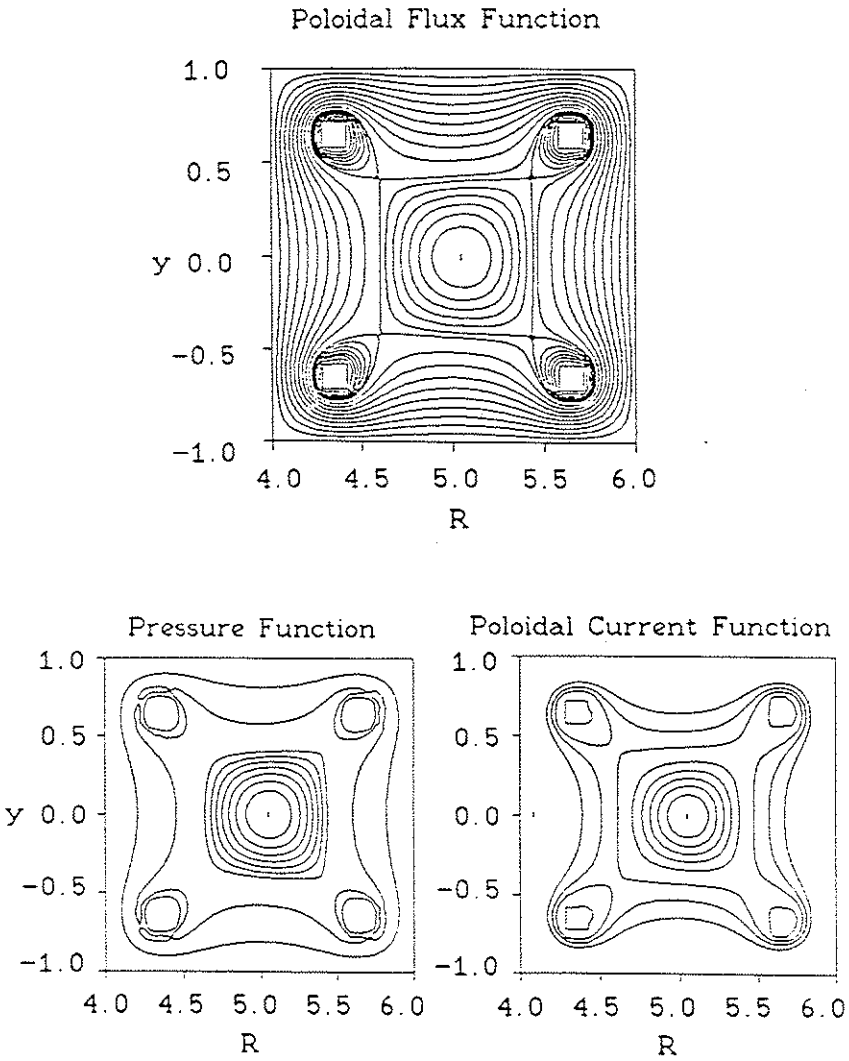

Fig. 2-12. Contour plots of ψ, P, and I.

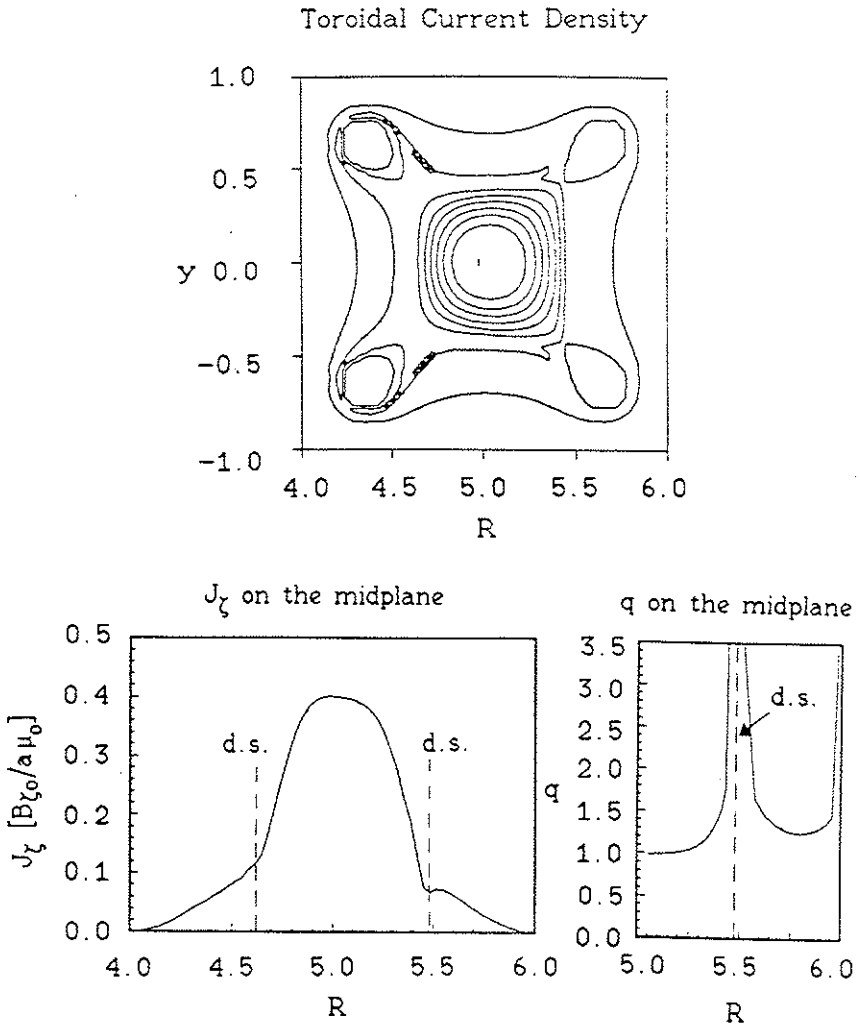

Fig. 2-13. Contour plot of J_ζ, and the J_ζ and q profiles on the midplane for a run in which η_ζ at the plasma center is increased from 0.0 to 0.3 units during the iterations.

obtained is shown in Fig.2-13 on page 40, which should be compared with Fig.2-11 on page 38. Except for the remnant of the numerical oscillations near the divertor separatrix, the toroidal current density has been smoothed out significantly. Note that plasma current is allowed to flow outside the divertor separatrix. The ratio of current carried by the divertor rings to that carried by the plasma is 3.7. The q profile on the midplane is also plotted in Fig.2-13. The q value goes to infinity on the divertor separatrix surfaces because the poloidal magnetic field vanishes at the separatrix x-points.

The results of convergence tests are presented in Figs.2-14, 2-15, and 2-16. The two contour plots of Fig.2-14 compare the pressure P and the poloidal current function I with the poloidal flux ψ. The contour curves for the two quantities in each plot are launched from the same points on the midplane. P and ψ are in very good to excellent agreement except for the region near the divertor separatrix. The pressure ridge that surrounds each divertor ring is difficult to represent numerically and a lack of adequate spatial resolution there manifests itself in the irregularities of the pressure contours near the divertor separatrix. (P is assumed to go to zero at the wall and the divertor rings.) On the other hand, ψ is easier to represent numerically near the ring in part because the value of ψ changes monotonically between the ring and the closest wall. I and ψ are in very good agreement

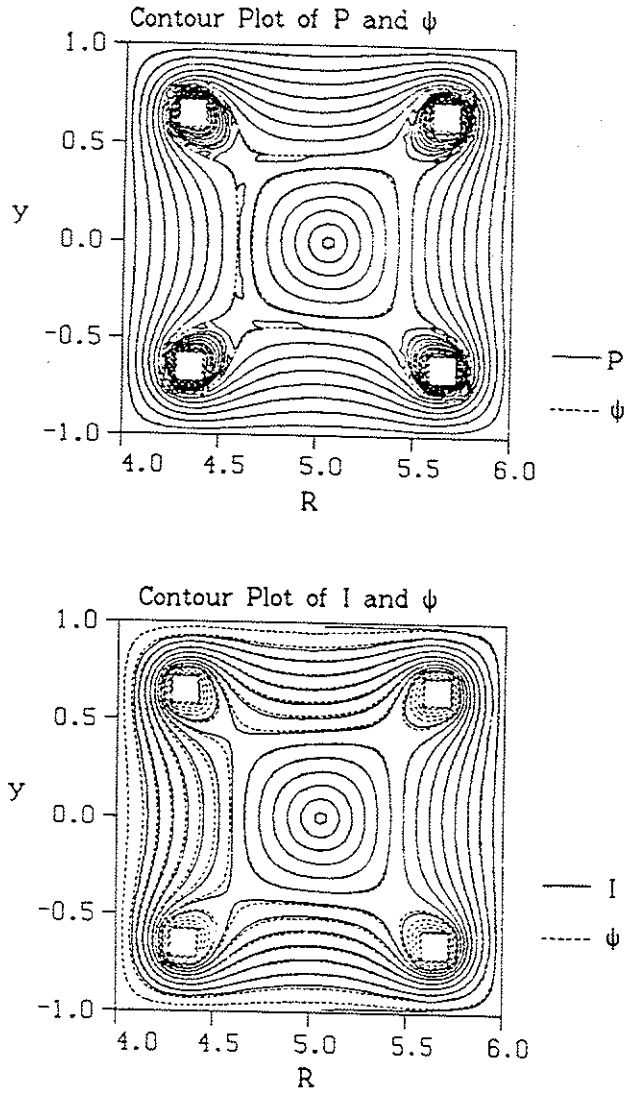

Fig. 2-14. Comparison of P and I with ψ contours.

inside the divertor separatrix but they exhibit slight to moderate discrepancies outside the divertor separatrix. The discrepancies can be attributed in part to a finite toroidal resistivity that was included for numerical purposes.

Fig.2-15 shows the evolution of the square of the unbalanced ficticious force during the iterations. By using $\Delta t = 0.0001$ and $b = 0.999$, this quantity was reduced by more than five orders of magnitude in 15000 iteration steps. Fig.2-16 illustrates the shift of the magnetic axis during the iterations. In contrast to the divertorless tokamak calculations in section 2-4-1, the axis shift here, which is small, fails to saturate. This is due to the finite η_ζ that gives rise to resistive diffusion of J_ζ. As this gradually takes place, the poloidal beta of the plasma increases and, as a result, the axis shift continues to increase. When η_ζ is set to zero, the axis shift does saturate during the iterations. However, such a run cannot be accepted because of the numerical problems with the current density near the divertor rings described before. As a reasonable compromise, we are forced to terminate the calculation when all other criteria in Sec.2-3 are satisfied approximately. The computer time requirement for such divertor calculations is about 10 percent longer than calculations for a divertorless tokamak.

Although the EQPD code can generate acceptable divertor equilibria for a number of cases, it cannot be used reliably

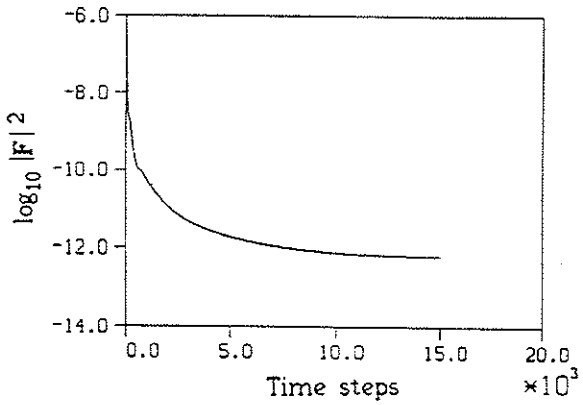

Fig.2-15. The evolution of the square of the unbalanced ficticious force during the iterations. (b=0.999)

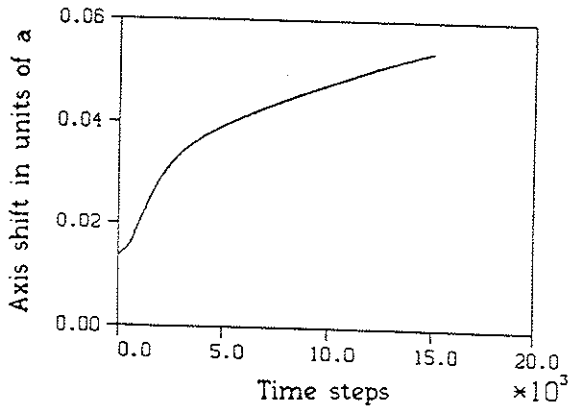

Fig.2-16. The shift of the magnetic axis in units of a during the iteration.

when the axis shift is large. A poloidal divertor tokamak with a small aspect ratio and/or a high beta must be excluded from investigation. We thus conclude that the Chodura-Schlüter method is not the best approach for a tokamak with more than one magnetic axis. In retrospect, the standard direct solution of the Grad-Shafranov equation should have been used despite the extra bookkeeping needed to handle multivaluedness of flux quantities.

Chapter 3. 3-D RESISTIVE MHD INITIAL VALUE CODE(RPD)

3-1. Introduction

Most resistive MHD initial value codes (e.g., HIB,[33,34] RSF,[18,54] and FAR[55,56]) for a tokamak Fourier analyze dependent variables in both toroidal and poloidal directions to take advantage of the symmetry or approximate symmetry of the device. However, when a vacuum vessel with a circular or elliptical cross section is replaced by that with a square or rectangular cross section, the advantage of a Fourier representation in the poloidal direction diminishes considerably. In the case of a poloidal divertor tokamak the problem is complicated significantly by the divertor separatrix that divides the computational domain into several topologically distinct regions. The equilibrium flux coordinates that would otherwise facilitate an efficient spatial representation for a noncircular tokamak[57] are no longer appropriate because of the singularities at the separatrix x-points and the multivaluedness of the flux function.

To simulate resistive tearing modes in a complicated geometry including the region outside the divertor separatrix, we have developed a new 3-D resistive MHD initial value code RPD.[36,37] Key features of the RPD are as follows.

1) Numerically advance the 3-D compressible full resistive MHD equations linearly or nonlinearly in a toroidal

geometry.

2) Fourier analyze dependent variables in the toroidal direction only. Use a finite difference representation in the two Cartesian directions of a constant toroidal angle plane.
3) Adopt a new, efficient semi-implicit scheme based on that proposed by Harned and Kerner.[38]
4) Handle nonsimply connected boundaries including poloidal divertor rings.

J.K. Lee has also developed a 1-D spectral, 2-D grid point resistive MHD initial value code CART[58] and studied the linear evolution of n=1 and 2 modes in highly elongated and poloidal divertor tokamaks.[59] He has shown that the separatrix has only a small effect on the linear behavior of global modes. His work, however, is limited in that the reduced MHD model was used, only the linear phase of mode evolution was studied and the divertor rings were kept outside the computational domain. With the features described above, the RPD code is capable of studying many effects that are important but neglected in the CART code work. They include the effects of toroidicity, nonlinearlity and compressibility on the resistive MHD evolution of noncircular and poloidal divertor tokamaks. The rest of this chapter elaborates the details of our RPD code.

3-2. Description of RPD

3-2-1. Plasma model

The full set of 3-D compressible resistive MHD equations used in this work are

$$\rho\left[\frac{\partial \mathbf{v}}{\partial t} + (\mathbf{v}\cdot\nabla)\,\mathbf{v}\right] = \frac{1}{\mu_o}(\nabla \times \mathbf{B}) \times \mathbf{B} - \nabla P + \nu\nabla^2\mathbf{v}\ , \qquad (3.1)$$

$$\frac{\partial \mathbf{B}}{\partial t} = \nabla \times (\mathbf{v} \times \mathbf{B}) - \nabla \times \left[\frac{\eta}{\mu_o}(\nabla \times \mathbf{B})\right]\ , \qquad (3.2)$$

$$\nabla\cdot\mathbf{B} = 0\ , \qquad (3.3)$$

$$\frac{\partial P}{\partial t} = -(\mathbf{v}\cdot\nabla)\,P - \Gamma P \nabla\cdot\mathbf{v}\ , \qquad (3.4)$$

where $\mathbf{B}$ is the magnetic field, $\mathbf{v}$ the flow velocity, P the thermal pressure, ρ the mass density, η the resistivity, ν the viscosity, and Γ the ratio of specific heats.

The magnetic field, velocity, and pressure are allowed to evolve linearly or nonlinearly by keeping linear terms only or by keeping both linear and nonlinear terms in the above set of equations. On the other hand, the resistivity and viscosity are frozen in time for simplicity. We should keep in mind that this simplification could lead to physically incorrect results in a highly nonlinear regime since the resistivity and viscosity of a plasma change significantly as the magnetic field lines become stochastic. Such effects, however, are of a highly global nature and cannot be readily included in the standard resistive

MHD model.

The continuity equation (Eq. (3.4) above) is dropped as is done in the CYL code[60] and the FAR code[55,56] of Oak Ridge National Laboratory, under the assumption that the effect of mass density fluctuations on the tearing mode evolution is negligibly small. This is known to be a good approximation for the tearing modes. This also has a numerically desirable consequence that then all the nonlinear terms can be evaluated easily by a straightforward convolution routine. Should the mass density be allowed to evolve in the momentum balance equation, the terms such as $(1/\rho)((\nabla \times \mathbf{B}) \times \mathbf{B})$ and $(1/\rho)(\nabla P)$ would require special treatment. They would have to be evaluated using a fast Fourier transform routine, which is significantly slower and requires considerably more memory space than a convolution routine unless the number of Fourier harmonics is very large.

Geometries considered in this work are square cross section tokamaks with and without a poloidal divertor. Full toroidal effects are included in both geometries. In the case of the divertor geometry each divertor ring is also assumed to have a square cross section for simplicity.

The wall and the divertor rings are assumed to be perfect conductors. In addition, we impose impermeable and no-slip boundary conditions on the surfaces of the conductors. We also require the pressure perturbation to vanish there. Then,

the boundary conditions that the dependent variables must satisfy at the wall and ring boundaries are

$$\hat{\mathbf{n}} \cdot \mathbf{B} = 0 \ , \tag{3.5}$$

$$\hat{\mathbf{n}} \times (\nabla \times \tilde{\mathbf{B}}) = 0 \ , \tag{3.6}$$

$$\mathbf{v} = 0 \ , \tag{3.7}$$

$$P = 0 \ , \tag{3.8}$$

where $\hat{\mathbf{n}}$ is the unit vector normal to the boundary and $\sim$ denotes a perturbation value.

3-2-2. Dimensionless set of equations

First, we introduce dimensionless variables as follows. The magnetic field is normalized to the equilibrium toroidal magnetic field $B_{\zeta o}$, the velocity to the Alfvén velocity $v_A \equiv B_{\zeta o} / (\mu_o \rho)^{1/2}$, and the thermal pressure to the equilibrium value P_o, all at the magnetic axis. To absorb the constant in front of the pressure gradient term in a dimensionless form of Eq. (3.1), however, we measure the dimensionless pressure in units of one half the plasma beta β, where $\beta \equiv P_o/((B_{\zeta o})^2/2\mu_o)$. The length and the time are normalized to one half the size of the poloidal cross section of dimension 2a by 2a and the fast Alfvén time $\tau_A \equiv a/v_A$ (characteristic time for the propagation of the compressional Alfvén wave perpendicular to the toroidal direction), respectively. The mass density is assumed to be constant and set equal to unity everywhere. The resistivity is normalized to the value η_o at the magnetic axis and measured

in units of the reciprocal of the 'fast Alfvénic' magnetic Reynolds number $S_A \equiv \tau_R/\tau_A = (a^2\mu_0/\eta_0)/(a/v_A)$. This should be distinguished from the standard magnetic Reynolds number $S \equiv \tau_R/\tau_{Hp} = (a^2\mu_0/\eta_0)/(R/v_A)$ often used in resistive MHD papers on tokamaks, where τ_{Hp} is the time required for the shear Alfvén wave to circumnavigate once toroidally divided by 2π. It follows from these definitions that $\tau_{Hp}=\tau_A A_r$ and $S = S_A/A_r$, where the aspect ratio A_r is the ratio of R_0 (major radius) to a(one half the width of poloidal cross section). Furthermore, the viscosity is normalized to the value ν_0 at the magnetic axis and measured in units of $\nu_0/(av_A)$.

Eqs. (3.1)-(3.4) can then be written in the compact dimensionless form

$$\frac{\partial \bar{\mathbf{v}}}{\partial \bar{t}} = -(\bar{\mathbf{v}}\cdot\bar{\nabla})\bar{\mathbf{v}} + (\bar{\nabla}\times\bar{\mathbf{B}})\times\bar{\mathbf{B}} - \bar{\nabla}\bar{P} + \bar{\nu}\bar{\nabla}^2\bar{\mathbf{v}} , \qquad (3.9)$$

$$\frac{\partial \bar{\mathbf{B}}}{\partial \bar{t}} = \bar{\nabla}\times(\bar{\mathbf{v}}\times\bar{\mathbf{B}}) - \bar{\nabla}\bar{\eta}\times(\bar{\nabla}\times\bar{\mathbf{B}}) + \bar{\eta}\bar{\nabla}^2\bar{\mathbf{B}} , \qquad (3.10)$$

$$\bar{\nabla}\cdot\bar{\mathbf{B}} = 0 , \qquad (3.11)$$

$$\frac{\partial \bar{P}}{\partial \bar{t}} = -\bar{\nabla}\cdot(\bar{P}\bar{\mathbf{v}}) + (1-\Gamma)\bar{P}\bar{\nabla}\cdot\bar{\mathbf{v}} , \qquad (3.12)$$

where a bar over a symbol signifies a dimensionless quantity. However, the overbar will be dropped from the rest of this

thesis for brevity of notation. Henceforth, all the quantities should be regarded as dimensionless unless otherwise noted.

We adopt a cylindrical coordinate system (R,y,ζ) and choose the angular variable in the toroidal direction (See Fig.2-1). Then, Eqs.(3.9)-(3.12) become

$$\frac{\partial v_R}{\partial t} = -\left[v_R\frac{\partial v_R}{\partial R} + v_y\frac{\partial v_R}{\partial y} + v_\zeta\left(\frac{1}{R}\frac{\partial v_R}{\partial \zeta} - \frac{v_\zeta}{R}\right)\right]$$
$$+(J_yB_\zeta - J_\zeta B_y) - \frac{\partial P}{\partial R} + \nu\left(\nabla^2 v_R - \frac{2}{R^2}\frac{\partial v_\zeta}{\partial \zeta} - \frac{v_R}{R^2}\right), \qquad (3.13)$$

$$\frac{\partial v_y}{\partial t} = -\left(v_R\frac{\partial v_y}{\partial R} + v_y\frac{\partial v_y}{\partial y} + v_\zeta\frac{1}{R}\frac{\partial v_y}{\partial \zeta}\right)$$
$$+(J_\zeta B_R - J_R B_\zeta) - \frac{\partial P}{\partial R} + \nu\nabla^2 v_y , \qquad (3.14)$$

$$\frac{\partial v_\zeta}{\partial t} = -\left[v_R\frac{\partial v_\zeta}{\partial R} + v_y\frac{\partial v_\zeta}{\partial y} + v_\zeta\left(\frac{1}{R}\frac{\partial v_\zeta}{\partial \zeta} + \frac{v_R}{R}\right)\right]$$
$$+(J_RB_y - J_yB_R) - \frac{1}{R}\frac{\partial P}{\partial \zeta} + \nu\left(\nabla^2 v_\zeta + \frac{2}{R^2}\frac{\partial v_R}{\partial \zeta} - \frac{v_\zeta}{R^2}\right) , \qquad (3.15)$$

$$\frac{\partial B_R}{\partial t} = \left[\frac{\partial}{\partial y}(v_RB_y - v_yB_R) - \frac{1}{R}\frac{\partial}{\partial \zeta}(v_\zeta B_R - v_R B_\zeta)\right]$$
$$-\frac{\partial \eta}{\partial y}J_\zeta + \eta\left(\nabla^2 B_R - \frac{2}{R^2}\frac{\partial B_\zeta}{\partial \zeta} - \frac{B_R}{R^2}\right) , \qquad (3.16)$$

$$\frac{\partial B_y}{\partial t} = \left[\frac{1}{R}\frac{\partial}{\partial \zeta}(v_yB_\zeta - v_\zeta B_y) - \frac{1}{R}\frac{\partial}{\partial R}(R(v_RB_y - v_yB_R))\right]$$
$$+\frac{\partial \eta}{\partial R}J_\zeta + \eta\nabla^2 B_y , \qquad (3.17)$$

$$\frac{\partial B_\zeta}{\partial t} = [\frac{\partial}{\partial R}(v_\zeta B_R - v_R B_\zeta) - \frac{\partial}{\partial y}(v_y B_\zeta - v_\zeta B_y)]$$

$$-\frac{\partial \eta}{\partial R} J_y + \frac{\partial \eta}{\partial y} J_R + \eta \left(\nabla^2 B_\zeta + \frac{2}{R^2}\frac{\partial B_R}{\partial \zeta} - \frac{B_\zeta}{R^2}\right) , \qquad (3.18)$$

$$\frac{1}{R}\frac{\partial}{\partial R}(RB_R) + \frac{\partial}{\partial y} B_y + \frac{1}{R}\frac{\partial}{\partial \zeta} B_\zeta = 0 , \qquad (3.19)$$

$$\frac{\partial P}{\partial t} = -[\frac{1}{R}\frac{\partial}{\partial R}(RPv_R) + \frac{\partial}{\partial y}(Pv_y) + \frac{1}{R}\frac{\partial}{\partial \zeta}(Pv_\zeta)]$$

$$+(1-\Gamma)P[\frac{1}{R}\frac{\partial}{\partial R}(Rv_R) + \frac{\partial v_y}{\partial y} + \frac{1}{R}\frac{\partial v_\zeta}{\partial \zeta}] , \qquad (3.20)$$

where the current density $\mathbf{J} = (J_R, J_y, J_\zeta)$ is given by

$$J_R = \frac{\partial B_\zeta}{\partial y} - \frac{1}{R}\frac{\partial B_y}{\partial \zeta} ,$$

$$J_y = \frac{1}{R}\frac{\partial B_R}{\partial \zeta} - \frac{1}{R}\frac{\partial}{\partial R}(RB_\zeta) ,$$

$$J_\zeta = \frac{\partial B_y}{\partial R} - \frac{\partial B_R}{\partial y} ,$$

and $\nabla^2 f = \frac{1}{R}\frac{\partial}{\partial R}(R\frac{\partial f}{\partial R}) + \frac{\partial^2 f}{\partial y^2} + \frac{1}{R^2}\frac{\partial^2 f}{\partial \zeta^2}$.

These equations must be numerically advanced linearly or nonlinearly subject to the boundary conditions as follows:

At the vertical boundary

$$B_R = 0 , \qquad (3.21)$$

$$\frac{\partial \tilde{B}_y}{\partial R} = 0 , \qquad (3.22)$$

$$\frac{1}{R}\frac{\partial}{\partial R}(R\tilde{B}_\zeta) = 0 , \qquad (3.23)$$

$$v_R = v_y = v_\zeta = 0 , \qquad (3.24)$$

$$\tilde{P} = 0 . \qquad (3.25)$$

At the horizontal boundary

$$B_y = 0 , \qquad (3.26)$$

$$\frac{\partial \tilde{B}_R}{\partial y} = 0 , \qquad (3.27)$$

$$\frac{\partial \tilde{B}_\zeta}{\partial y} = 0 , \qquad (3.28)$$

$$v_R = v_y = v_\zeta = 0 , \qquad (3.29)$$

$$\tilde{P} = 0 . \qquad (3.30)$$

3-2-3. Spatial discretization

The seven dependent variables $\mathbf{B} = (B_R, B_y, B_\zeta)$, $\mathbf{v} = (v_R, v_y, v_\zeta)$, and P are Fourier analyzed only in the toroidal direction to take advantage of the periodicity in this direction. Thus, a function (e.g., **B**, **J**) will be expanded as

$$f(R,y,\zeta;t) = f^{o}(R,y;t)$$

$$+\sum_{n=1}^{\infty} [\, f^{n^{+}}(R,y;t)\cos(n\zeta) + f^{n^{-}}(R,y;t)\sin(n\zeta)] \quad . \quad (3.31)$$

Assuming a slow toroidal variation of the plasma quantities, we usually truncate the Fourier series keeping only several terms. We distinguish between Fourier cosine and sine terms by adding superscripts $^{+}$ and $^{-}$ to the toroidal mode number. For example, $n = 2^{+}$ and 3^{-} refer to $\cos(2n\zeta)$ and $\sin(3n\zeta)$ terms, respectively.

As for the two Cartesian directions R and y, an equally spaced but staggered two dimensional grid (see Fig. 3-1) is set up to handle the complicated geometry including the divertor separatrix and the divertor rings. The grid is extended one row and one column beyond the physical boundaries to properly advance the plasma quantities near the edge subject to the boundary conditions. All the first and second derivative terms with respect to R and/or y are discretized by using the standard second-order accurate difference form.

Use of the staggered grid requires more interpolation steps and additional bookkeeping compared with an unstaggered grid, but it does have the desirable feature of strongly coupling the plasma quantities at even-numbered and odd-numbered grid points. In addition, our choice of placing B_R, B_y, and B_ζ in a grid cell allows us to evaluate the nonaxisymmetric part of B_ζ accurately by using Eq. (3.19) with B_R and B_y that are only

$\Delta R/2$ and $\Delta y/2$ away. Had we used the unstaggered grid instead, B_R and B_y would be twice as far from the center of a grid cell where B_ζ is evaluated and this results in a larger discretization error.

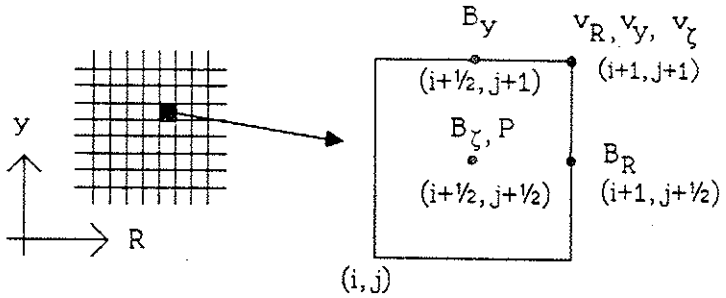

Fig. 3-1. Placement of dependent variables in a grid cell. i and j are indicies in the R and y directions.

It would be desirable to have more grid points near the tearing layers where the plasma quantities vary rapidly and near the divertor separatrix where the magnetic field structure is expected to be sensitive to a small perturbation. A grid packing is found to be impractical, however, because such regions are not confined to a few rows and/or columns of the grid. The extra logical IF statements needed to identify such regions would slow down dramatically the execution of the code on the Cray computers by making many DO loops nonvectorizable. Furthermore, in a highly nonlinear regime a large number of secondary modes are excited and a significant portion of the plasma could become stochastic. In such a case

the grid density must be increased everywhere. A more practical option for grid packing would be to increase grid points near the divertor rings where the gradients of plasma quantities are large. This option should be included in a future version of the RPD code.

3-2-4. Time advancement

The first successful version of the code adopted a mostly explicit, first-order accurate time advancement scheme as in the CYL code. The dependent variables are not staggered in time and time advancement is not time-centered. This scheme can be summarized as follows.

First, the three components of the velocity v_R, v_y, and v_ζ are advanced fully explicitly as

$$\frac{\mathbf{v}^{t+\Delta t}-\mathbf{v}^{t}}{\Delta t} = \mathbf{F}^{t} , \qquad (3.32)$$

where $\mathbf{F}^t \equiv -(\mathbf{v}^t\cdot\nabla)\mathbf{v}^t + (\nabla \times \mathbf{B}^t)\times \mathbf{B}^t - \nabla P^t + \nu\nabla^2\mathbf{v}^t$ and Δt is the temporal advancement step size. The superscripts t and $t+\Delta t$ refer to values at the old and new times.

Next, the two Cartesian components (B_R, B_y) and the axisymmetric part of the toroidal component of the magnetic field $(B_{\zeta n=0})$ and the pressure P are advanced as

$$\frac{\mathbf{B}^{t+\Delta t}-\mathbf{B}^{t}}{\Delta t} = \nabla \times (\mathbf{v}^{t+\Delta t}\times\mathbf{B}^{t}) - \nabla\eta\times\nabla\times\mathbf{B}^{t} + \eta(\nabla^2\mathbf{B})^{ADI} , \qquad (3.33)$$

$$\frac{P^{t+\Delta t}-P^{t}}{\Delta t} = -\nabla\cdot(P^{t}\mathbf{v}^{t+\Delta t}) + (1-\Gamma)P^{t}\nabla\cdot\mathbf{v}^{t+\Delta t} , \qquad (3.34)$$

by evaluating the velocity at the new time $t+\Delta t$ that was just calculated in Eq. (3.32). This essentially makes the time advancement of the magnetic field and the pressure partially implicit. When the old time was used for the velocity in these equations, the scheme was found to be unconditionally unstable.

We also treat the resistivity term implicitly. The superscript ADI in Eq. (3.33) stands for an alternating direction implicit method. The second derivative terms of the resistivity terms are treated implicitly (i.e., evaluated at the new time) one term at a time. This reduces a large matrix inversion problem to the solution of a set of small tridiagonal matrices.

Finally, the nonaxisymmetric parts of B_ζ are evaluated by using the divergence-free condition for the magnetic field in the form

$$B_\zeta^{t+\Delta t} = \pm\frac{1}{n}\left[\frac{\partial}{\partial R}(RB_R^{t+\Delta t}) + R\frac{\partial}{\partial y}B_y^{t+\Delta t}\right] , \qquad (3.35)$$

where the + or − sign must be chosen for Fourier cosine and sine terms, respectively.

Despite some implicitness we call this scheme mostly explicit because the maximum step size for numerical stability is found to be limited by the fully explicit time advancement of the

velocity. We will come back to this point in section 3-3 and present an efficient, new semi-implicit scheme in section 3-4.

We could make the scheme second-order accurate in time by adding a predictor corrector step as in the RSF code.[18,54] However, for the small step sizes that were used in runs with the mostly explicit scheme first-order accuracy in time was shown to be very satisfactory. This is because numerical errors in such a code are dominated by spatial discretization. Furthermore, additional 3-D arrays and extra numerical steps were found to cause an unacceptable extra cost in terms of memory and CPU time requirements. This was especially true before the advent of the Cray-2. To facilitate efficient code runs, we use the first-order accurate scheme throughout this thesis research.

3-2-5. Some numerical details

3-2-5-a. Treatment of unresolved force in the equilibrium

An axisymmetric MHD equilibrium input for this code is generated by the 2-D Chodura-Schlüter code that was described in Chapter 2. Unfortunately, the numerical equilibrium usually contains a small but finite unresolved force and it could become significant when the poloidal flux function is transformed numerically to the two Cartesian components of the magnetic field. To eliminate the effect of this residual force on the evolution of the resistive instabilities, we calculate the three

components of this residual force at the beginning of a run, store them in three 2-D arrays, and substract them from the right hand sides of Eqs. (3.13)-(3.15).

3-2-5-b. Addition of a helical perturbation

To excite a tearing mode in a tokamak plasma, we need to break the axisymmetry of the original MHD equilibrium. This can be accomplished by adding any perturbation as long as it includes a helical component that is resonant with the tearing mode of interest. In fact, even a random perturbation will most likely serve this purpose because it consists of a very large number of small but finite helical harmonics. To facilitate a rapid convergence to a true eigensolution, however, it is desirable to add a helical perturbation that is reasonably close to the final state. Furthermore, the perturbation needs to be divergence-free.

To this end, we first add a small helical perturbation ψ_{pert} to the equilibrium poloidal flux function ψ_{eq} of the form

$$\psi_{pert} = A \frac{\psi_{eq}^{m}(1-\psi_{eq})}{1+\exp[10(-1+\psi_{eq}/\psi_{q})]} \cos(m\Theta - n\zeta), \qquad (3.36)$$

where A is a constant, ψ_q is the value of ψ_{eq} on which $q = m/n$, and Θ is the poloidal angle measured with the center shifted to the location of the magnetic axis. ψ_{eq} is set equal

to zero at the magnetic axis and it is normalized to the value at the wall or that at the inner divertor separatrix in divertorless or divertor geometries, respectively.

Next, the perturbed poloidal flux function is transformed to $(B_R)_{pert}$ and $(B_y)_{pert}$. Each component is then expanded into a form $f^+(R,y)\cos(n\zeta) + f^-(R,y)\sin(n\zeta)$ and the coefficients in front are stored in proper arrays to initialize a resistive MHD run.

3-2-5-c. Suppression of resistive decay of the equilibrium

It is well known that the time scale for the linear growth of a resistive tearing mode is significantly faster than that for the resistive decay of the MHD equilibrium. Nevertheless, in a nonlinear run that extends as long as several resistive diffusion times the effect of resistive decay could become quite important. From a theoretical viewpoint, it is desirable to distinguish the modification of the equilibrium due to the nonlinear mode couplings from that due merely to resistive diffusion which takes place even in the absence of tearing modes. To this end, we apply to the plasma an electric field that eliminates the resistive diffusion effect completely. This is accomplished by breaking up the axisymmetric (n=0) part of the magnetic field into two parts: the equilibrium part that was originally present and the additional axisymmetric part that is generated by nonlinear mode couplings. The former part is

excluded from the resistivity terms of the time advancement equations for the magnetic field (Eqs. (3.16)-(3.18)).

3-2-5-d. Treatment of divertor ring regions

The regions near the divertor rings, especially near the sharp corners, tend to cause numerical problems. They almost invariably manifest themselves as growing ripples in v_ζ and B_ζ at first and gradually propagate to other quantities over the entire plasma. The ripples result from the steep gradient of the plasma quantities that are not accurately represented by a limited number of grid points and the singularities at the sharp corners where the normal and tangential directions are not well defined. To overcome such difficulties, both resistivity and viscosity are increased sharply near the divertor rings. Although numerically motivated, this is qualitatively consistent with the real physical characteristics of the plasma in a poloidal divertor tokamak.

3-2-6. Additional features of the code

A number of run options are made available for our RPD code. Control parameters in the input file are an essential part of the code to make the code versatile. Here, we discuss only two control parameters: a start/restart flag and a linear/nonlinear flag.

When the code is run with a start option, it reads an

equilibrium file and adds a helical perturbation to the axisymmetric MHD equilibrium. Just before the end of the run the code creates a data file that contains information about the latest plasma state and the initial MHD equilibrim at all the grid points. When a restart option is chosen in the next run, the code reads this data file instead and resumes calculations from the state it had reached previously. This data file can also be used as an input file for data analysis routines, some of which are not attached to the RPD itself. This restart option is very important for two reasons.

First, a typical nonlinear run takes hours, sometimes tens of hours, of Cray CPU time and there is a small but finite possibility that the calculation gets contaminated or even lost due to computer problems before a successful completion of the run. By breaking up a long simulation run into several shorter run segments, however, we can always restart the code from the most recent data file that is valid, and thereby minimize the damage due to such an event.

Secondly, it is not always easy to predict in advance what and when to plot in the course of a long simulation run. It is also not efficient to attach all the diagnostic routines to the main simulation program because of the larger program size required. On the other hand, keeping track of the entire history of the simulation would not be feasible due to the enormous disk space requirements and slow disk I/O rates. A

family of data files created at the end of run segments constitute a convenient data base to study the time history of the resistive MHD evolution later.

The code can be run linearly or nonlinearly by properly setting the linear/nonlinear flag. When the linear option is chosen, all the equilibrium quantities are frozen in time regardless of the size of the perturbation. When the nonlinear option is chosen instead, all the nonlinear terms are calculated by a fully vectorized convolution routine.

By combining the nonlinear and restart options together we can use the data file created by a linear run as an input for a nonlinear run. This facilitates an efficient nonlinear simulation because the initial transient phase that contaminates nonlinear mode interactions can be calculated through with a faster linear simulation.

3-3. Code Efficiency Improvement

3-3-1. Limitations of the mostly explicit scheme

Our RPD code is almost fully optimized for the Cray computers. Virtually all the vectorizable DO loops are vectorized. When the CIVIC or CFT compiler fails to vectorize a vectorizable DO loop by erroneously detecting a vector hazard, we invoke a compiler directive to force vectorization. For nested DO loops, a DO loop with the largest range is usually placed inside since the CIVIC and CFT compilers on the Cray only

vectorize innermost loops. Additional care is taken to minimize bank conflicts and quadrant conflicts in memory access that could slow down the code precipitously.

Despite such care, the efficiency of the first successful version of the code was found to be too poor to conduct efficient code tests, let alone an extensive parameter survey. To obtain a highly converged linear result with a 60x60 grid, we need to run the code for 30 to 120 minutes of Cray-1 CPU time, depending on the growth rate of the mode. This stems from the large number of grid points required by the finite difference representation in two directions and a small temporal step size due to the mostly explicit scheme. The size of the executable file (controlee) of such a case ranges from 1.2 to 1.4 million octal words depending on the geometry (with or without a poloidal divertor) chosen, which compiler (CFT or CIVIC) is used, and the amount of diagnostic routines attached. This means that a fairly high priority must be used on the Cray-1 (also on the Cray X-MP) except when the machine is underutilized.

When the grid size is increased for higher spatial resolution, the simulation becomes prohibitively expensive. For example, for a case with a 100x100 grid and only three toroidal harmonics (n=0, 1^+, and 1^-) the size of the executable file increases to about 3 million octal words and it can no longer be run on the smaller Cray-1 (C machine). Not only need

plasma quantities be advanced at many more grid points, but the temporal step size needs to be reduced because of the mostly explicit scheme. We now examine the two factors that make a higher resolution run almost infeasible.

The first factor is the quadratic increase in the number of grid points in the RPD code for a higher spatial resolution run. The quadratic increase may seem to be much worse than the linear increase of the number of grid points in the 2-D spectral code. However, we need to keep in mind that we are primarily interested in a poloidal divertor tokamak. A higher resolution run in such a geometry using a 2-D spectral code would require more poloidal Fourier harmonics as well as more radial grid points. Worse yet, these additional poloidal Fourier harmonics interacting with a helical perturbation need to be evaluated using a relatively time-consuming convolution routine. The quadratic dependence of computational requirements for a higher resolution run is indeed an intrinsic feature of a poloidal divertor tokamak and there is nothing much we can do about it except for a grid packing near the divertor rings.

The second factor is the linear dependence of the maximum temporal step size Δt_{max} for numerical stability on the grid spacing Δx. The number of time steps required to reach the same physical state, therefore, increases linearly with the number of the grid points in the R (or y) direction. This is

the well known Courant-Fredrichs-Lewy(CFL) stability criterion[61] for an explicit scheme. When the step size Δt is made greater than the time required for the fastest wave in the plasma model to propagate from one grid point to the nearest neighbor, the wave can no longer be represented properly by this numerical scheme. The velocity at the new time would then depend on the region that extends beyond the grid points from which the new velocity is calculated. The fastest wave that a compressible full resistive MHD plasma can support in a tokamak is the compressional Alfvén wave that propagates in the direction perpendicular to the equilibrium magnetic field. By analytically or numerically removing the step size restriction imposed by this wave in a tokamak geometry, we can expect to improve the code efficiency dramatically. We will focus on this point in the next section.

3-3-2. Options to increase the temporal step size

3-3-2-a. Reduced MHD model[35]

In a large-aspect-ratio tokamak ($\epsilon \equiv 1/A_r << 1$) the full resistive MHD equations can be expanded in powers of ϵ. By ordering the pressure ($\beta \sim \epsilon^2$ for a low beta tokamak and $\beta \sim \epsilon$ for a high beta tokamak) and retaining terms up to a specified order in ϵ we obtain the reduced resistive MHD equations that are correct to that order. For example, the low-β second-order equations in dimensionless form are

$$\frac{\partial \Psi}{\partial t} = -\mathbf{v}_\perp \cdot \nabla \Psi - \frac{\partial \Phi}{\partial \zeta} + \frac{1}{S}(\eta J_\zeta - E^W), \tag{3.37}$$

$$\frac{\partial U}{\partial t} = -\mathbf{v}_\perp \cdot \nabla U - \hat{\zeta} \cdot (\nabla \Psi \times \nabla J_\zeta) - \frac{\partial J_\zeta}{\partial \zeta} + \frac{1}{R} \nabla_\perp^2 U, \tag{3.38}$$

where Ψ is the poloidal flux function, Φ the velocity stream function, U the toroidal component of the vorticity, E^W the toroidal component of the electric field at the wall, S the magnetic Reynolds number, and R the fluid Reynolds number. The subscript $\perp$ denotes the constant toroidal angle plane. The velocity, the stream function and the toroidal component of vorticity are related by

$$\mathbf{v}_\perp = \nabla \Phi \times \hat{\zeta}, \tag{3.39}$$

$$U = \nabla_\perp^2 \Phi, \tag{3.40}$$

and the toroidal current density is given by

$$J_\zeta = \nabla_\perp^2 \Psi. \tag{3.41}$$

The normalization convention here follows that of Ref. 54 instead of that in section 3-2-2.

In addition to its simplicity in containing fewer equations and dependent variables than in the full set, the lower-order reduced set of equations has the very attractive numerical feature of eliminating the fast compressional waves from a tokamak plasma. The maximum temporal step size for numerical stability is no longer limited by the fastest time scale

but by the less restrictive shear Alfvén time scale. It has been shown that such a simplication does not modify significantly the tearing mode evolution, even at an aspect ratio of five.[60]

When a 1-D spectral, 2-D finite difference representation is employed in spatially discretizing the reduced set of equations, however, the solution of Eq.(3.40) for Φ requires much more work space and CPU time than the case with a 2-D spectral, 1-D finite difference code. Because of finite differencing in two directions the matrix problem is not a set of small, simple tridiagonal systems. Instead, for each toroidal Fourier component a very large band matrix (tridiagonal matrix with fringes) needs to be solved using a fast iterative method or an operator splitting method.

Furthermore, to study a tokamak that departs greatly from the standard ordering assumptions, higher order terms in ϵ must be kept in the reduced set of equations. R. Izzo and coworkers at Princeton Plasma Physics Laboratory extended the reduced set to fifth-order in ϵ.[62] Not only are such equations more complicated, but the step size restriction due to the fast compressional wave will reappear unless parts of the magnetic field and the velocity responsible for this wave are advanced implicitly.

Although a formalism utilizing a small inverse aspect ratio expansion has the advantage of revealing the physical

contributions of various terms for a wide range of MHD instabilities, the reduced model as applied to noncircular and poloidal divertor tokamaks including toroidal and separatrix effects seems to defeat its purpose. From a pragmatic viewpoint, an implementation of the reduced MHD model in our RPD code clearly represents an unnecessary duplication of effort since the CART code,[58,59] although limited to a linear version of the third-order accurate reduced model, has already been developed.

3-3-2-b. Incompressible model

When an MHD plasma is assumed to be incompressible by imposing a $\nabla\cdot\mathbf{v} = 0$ condition, all the compressional waves are eliminated. This includes elimination of the fast compressional Alfven wave that propagates approximately in the poloidal plane, and thereby, as in the lower-order reduced resistive MHD model, the severe step size restriction for numerical stability due to the fast wave can be removed.

A novel feature of this analytic simplification is that it can be applied to the full set of equations in which no ordering assumption is made. If the equation of state is chosen to be

$$\nabla^2 P = \nabla\cdot[-(\mathbf{v}\cdot\nabla)\mathbf{v} + (\nabla\times\mathbf{B})\times\mathbf{B} + \nu\nabla^2\mathbf{v}] \qquad (3.42)$$

instead of that described by Eq.(3.12), the velocity will remain

divergence-free at all time if it is so initially. This can be readily seen by noting

$$\frac{\partial}{\partial t}(\nabla\cdot\mathbf{v}) = \nabla\cdot\left(\frac{\partial \mathbf{v}}{\partial t}\right)$$
$$= \nabla\cdot[-(\mathbf{v}\cdot\nabla)\mathbf{v} + (\nabla\times\mathbf{B})\times\mathbf{B} + \nu\nabla^2\mathbf{v}] - \nabla^2 P. \qquad (3.43)$$

The incompressible model has been implemented, at least as an option, in several full resistive MHD initial value codes; a partial list includes the full resistive MHD code at the Institute of Fusion Studies of the University of Texas-Austin[63] and the incompressible versions of CYL[60] and FAR[55,56] of ORNL.

These codes use a 2-D spectral, 1-D finite difference representation and the solution of Eq. (3.42) can be essentially reduced to a set of small tridiagonal matrices. On the other hand, the RPD code is finite differenced in two directions and Eq. (3.42) poses a very large band matrix problem as Eq. (3.40) does in the reduced MHD model. This makes the compressional model less attractive for RPD.

Furthermore, as an application of RPD, it is of considerable interest to study in future work implications of the divertor separatrix for H mode operation.[64] To this end, it is desirable, if ever possible, to retain compressibility in improving the code efficiency.

3-3-2-c. Fully implicit scheme

A fully implicit scheme in MHD calculations usually refers to a time advancement algorithm in which all the linear parts of the right hand side of the magnetic field, velocity, and pressure advancement equations are evaluated at the new time level $t+\Delta t$.[56,65] (A truly fully implicit scheme should evaluate everything on the right hand side at $t+\Delta t$, but such a scheme would result in an extremely large set of nonlinear equations that cannot be solved in general.) The way the plasma quantities at a grid point evolve from t to $t+\Delta t$, therefore, depends not only on their old values at that point and its nearest neighbors but on how they evolve at all other grid points from t to $t+\Delta t$. Information about a plasma disturbance can propagate instantaneously from one grid point to the rest of the computational domain. As a result, the step size for time advancement can be made arbitrarily large without numerical instabilities while all the modes are retained in the plasma including the fast compressional and the shear Alfven waves.

The fully implicit scheme has been successfully implemented in the 2-D spectral, 1-D finite difference full MHD code FAR[55,56] that makes no analytic ordering assumption. The linear eigenvalue (linear growth rate) requires only a few time steps when a reasonable initial perturbation is chosen. Efficiency of the nonlinear simulation is also improved dramatically although the nonlinear part is treated explicitly in

the code.

Unfortunately, the fully implicit scheme requires the solution of very large and complicated matrices. Setting up such matrices involves a considerable amount of bookkeeping and the matrix inversion calls for significant work space and computer time. The FAR code circumvented these problems by developing a routine that automatically generates the matrix elements and by performing an LU decomposition, the expensive part of a direct solver, only at the outset of a simulation.[56]

Although this approach can be extended in principle to a 1-D spectral, 2-D finite difference code, it is not practical to implement in RPD presently due to the CPU memory limitation of the current generation of supercomputers. Even with a moderate grid size of 60x60 the executable file cannot be fit into the CPU memory of the Cray-2.

3-3-2-d. New semi-implicit scheme

The semi-implicit scheme in MHD refers to a new class of time advancement algorithms that was first proposed by Harned and Kerner[38] for a compressible full MHD plasma. By adding a simple semi-implicit term to the full set of equations and treating the part of the equations responsible for linear parasitic waves implicitly or approximately implicitly, we can remove the step size restriction imposed by such waves without altering the physics of the MHD plasma.

To illustrate this point, consider a fully explicit time advancement of the velocity as given by Eq.(3.32). The maximum step size for numerical stability is limited by the fast compressional waves in a poloidal plane. Let $\boldsymbol{C}\cdot\mathbf{v}$ be the linear term that is responsible for these waves. ($\boldsymbol{C}$ is a matrix.) A semi-implicit scheme that eliminates the fast wave temporal step size restriction can be constructed by making implicit only the term $\boldsymbol{C}\cdot\mathbf{v}$ in Eq.(3.32). This can be achieved by subtracting $\boldsymbol{C}\cdot\mathbf{v}$ at the new time level from the left hand side of Eq.(3.32) and $\boldsymbol{C}\cdot\mathbf{v}$ at the old time from the right hand side. In this procedure, however, the fast compressional wave itself is retained in the plasma.

In general, the semi-implicit scheme for the velocity advancement can be written as

$$\frac{\partial \mathbf{v}}{\partial t} = \mathbf{F} + \alpha\,\Delta t\;\boldsymbol{G}\cdot\frac{\partial \mathbf{v}}{\partial t}\,, \qquad (3.44)$$

where $\boldsymbol{G}$ is the semi-implicit operator, Δt is the temporal step size, and α is a positive constant. The case where $\boldsymbol{G} = \boldsymbol{C}/\alpha$ corresponds to the previous example.

The real advantage of the semi-implicit scheme comes from the great flexibility in choosing the semi-implicit operator $\boldsymbol{G}$. We need not choose the semi-implicit operator so that it exactly matches the term that limits the maximum step size for numerical stability. As long as the semi-implicit operator contains the dominant part of the exact term, a significant step

size increase can be attained over the mostly explicit scheme without numerical instabilities. By making a judicious choice for the operator form, we can keep each time advancement step with a much larger step size almost as simple and fast as that with a much smaller step size for the explicit scheme. This would yield a very efficient code. On the other hand, an exact choice would almost invariably result in a very complicated matrix problem as in the fully implicit scheme. The exact choice, therefore, is most likely couterproductive.

A simple semi-implicit operator that removes the fast wave step size restriction was successfully implemented in a 2-D spectral, 1-D finite difference resistive MHD code.[38,66] The semi-implicit scheme was then extended to remove the shear Alfvén step size restriction as well.[67] Later a very simple isotropic operator was shown to be adequate to remove both step size restrictions although the accuracy tends to degrade for a larger step size.[68]

Being encouraged by the novel features of the semi-implicit scheme, we decided to develop for and implement in RPD a new numerical procedure that is based on it.

3-4. Implementation of the New, Efficient Semi-Implicit Scheme

3-4-1. A simplified semi-implicit operator

The linearized ideal MHD equations without an equilibrium flow in a dimensionless form are

$$\frac{\partial \mathbf{v}_1}{\partial t} = (\nabla \times \mathbf{B}_o) \times \mathbf{B}_1 + (\nabla \times \mathbf{B}_1) \times \mathbf{B}_o - \nabla P_1 , \tag{3.45}$$

$$\frac{\partial \mathbf{B}_1}{\partial t} = \nabla \times (\mathbf{v}_1 \times \mathbf{B}_o) , \tag{3.46}$$

$$\nabla \cdot \mathbf{B}_1 = 0 , \tag{3.47}$$

$$\frac{\partial P_1}{\partial t} = -(\mathbf{v}_1 \cdot \nabla) P_o - \Gamma P_o (\nabla \cdot \mathbf{v}_1) , \tag{3.48}$$

where the subscripts o and 1 denote equilibrium and perturbed quantities. Taking a time derivative of Eq. (3.45) and combining it with Eqs. (3.46) and (3.48), we obtain

$$\frac{\partial^2 \mathbf{v}_1}{\partial t^2} = (\nabla \times \mathbf{B}_o) \times [\nabla \times (\mathbf{v}_1 \times \mathbf{B}_o)] + \{\nabla \times [\nabla \times (\mathbf{v}_1 \times \mathbf{B}_o)]\} \times \mathbf{B}_o + \nabla [(\mathbf{v}_1 \cdot \nabla) P_o + \Gamma P_o (\nabla \cdot \mathbf{v}_1)] . \tag{3.49}$$

This equation contains the kink and interchange modes in addition to the fast compressional and shear Alfvén waves. To extract the latter part we take B_o and P_o to be spatially uniform. Then, Eq. (3.49) becomes

$$\frac{\partial^2 \mathbf{v}_1}{\partial t^2} = \{\nabla \times [\nabla \times (\mathbf{v}_1 \times \mathbf{B}_o)]\} \times \mathbf{B}_o + \Gamma P_o \nabla (\nabla \cdot \mathbf{v}_1) . \tag{3.50}$$

The right hand side of this equation is still much too complicated to implement in the semi-implicit scheme.

By assuming that the magnetic field is predominantly in

the toroidal direction, however, the part that is responsible for the compressional waves with the wave vector perpendicular to the equilibrium magnetic field can be approximately written as

$$\frac{\partial^2 \mathbf{v}_{1\perp}}{\partial t^2} = (B_o^2+\Gamma P_o)\,\nabla_\perp(\nabla\cdot\mathbf{v}_{1\perp})\,. \qquad (3.51)$$

This leads us to propose a semi-implicit term $\alpha\Delta t(\partial/\partial t)[\nabla_\perp(\nabla\cdot\mathbf{v}_\perp)]$ which is the same as that used by Harned and Kerner.[38]

Three components of the velocity advancement equation are

$$\frac{v_R^{t+\Delta t}-v_R^t}{\Delta t} - \alpha\frac{\partial}{\partial R}\left[\frac{1}{R}\frac{\partial}{\partial R}(Rv_R^{t+\Delta t})\right] - \alpha\frac{\partial^2}{\partial R\partial y}v_y^{t+\Delta t}$$

$$= F_R^t - \alpha\frac{\partial}{\partial R}\left[\frac{1}{R}\frac{\partial}{\partial R}(Rv_R^t)\right] - \alpha\frac{\partial^2}{\partial R\partial y}v_y^t\,, \qquad (3.52)$$

$$\frac{v_y^{t+\Delta t}-v_y^t}{\Delta t} - \alpha\frac{\partial}{\partial y}\left[\frac{1}{R}\frac{\partial}{\partial R}(Rv_R^{t+\Delta t})\right] - \alpha\frac{\partial^2}{\partial y^2}v_y^{t+\Delta t}$$

$$= F_y^t - \alpha\frac{\partial}{\partial y}\left[\frac{1}{R}\frac{\partial}{\partial R}(Rv_R^t)\right] - \alpha\frac{\partial^2}{\partial y^2}v_y^t\,, \qquad (3.53)$$

$$\frac{v_\zeta^{t+\Delta t}-v_\zeta^t}{\Delta t} = F_\zeta^t\,, \qquad (3.54)$$

where $F_R{}^t$, $F_y{}^t$, and $F_\zeta{}^t$ are three components of $\mathbf{F}^t = -(\mathbf{v}^t\cdot\nabla)\mathbf{v}^t + (\nabla\times\mathbf{B}^t)\times\mathbf{B}^t - \nabla P^t + \nu\nabla^2\mathbf{v}^t$.

It is very important to note that no approximation has been made to $\mathbf{F}$; all the physics in the original set of compressional, full resisitive MHD equations are kept except for a small dispersive effect introduced by the semi-implicit term. All the approximations are applied only to the semi-implicit term.

The simplified semi-implicit term of our choice should work best in a large aspect ratio tokamak without a poloidal divertor. In the case of a poloidal divertor tokamak the simplifying assumption breaks down in the vicinity of the divertor ring where the poloidal magnetic field is comparable to the toroidal field. The stabilizing properties of the semi-implicit scheme are expected to degrade there considerably. The simplifying assumption also tends to break down in a small aspect ratio tokamak. Despite such limitations, however, we can justify the use of such a semi-implicit term by noting that even a modest increase of the step size would represent a considerable saving of computer resources in a large scale numerical simulation. Furthermore, the extent to which such simplifications affect the stability of the scheme has to be determined from numerical experiments.

3-4-2. Operator splitting method

Despite gross simplifications, a direct solution of Eqs. (3.52) and (3.53) as applied to our RPD code would still involve a large matrix problem because of the coupling of v_R and v_Y and

the mixed partial derivative terms. This essentially stems from a finite-difference representation in two directions. Were the dependent variables Fourier analyzed in one more direction, Eqs. (3.52) and (3.53) could be combined into a single equation that includes only one dependent variable, say v_R. This can be solved for $v_R^{t+\Delta t}$ by a simple tridiagonal matrix solver and $v_y^{t+\Delta t}$ can be found by a simple substitution into the equation that relates $v_R^{t+\Delta t}$ and $v_y^{t+\Delta t}$.

To alleviate the large matrix problem, we proposed to split the semi-implicit operator as follows.[37,41] For odd-numbered time steps v_R and v_y are advanced as

$$\frac{v_R^{t+\Delta t}-v_R^t}{\Delta t}-\alpha\frac{\partial}{\partial R}\left[\frac{1}{R}\frac{\partial}{\partial R}(Rv_R^{t+\Delta t})\right]=F_R^t-\alpha\frac{\partial}{\partial R}\left[\frac{1}{R}\frac{\partial}{\partial R}(Rv_R^t)\right], \quad (3.55)$$

$$\frac{v_y^{t+\Delta t}-v_y^t}{\Delta t}-2\alpha\frac{\partial}{\partial y}\left[\frac{1}{R}\frac{\partial}{\partial R}(Rv_R^{t+\Delta t})\right]-\alpha\frac{\partial^2}{\partial y^2}v_y^{t+\Delta t}$$

$$=F_y^t-2\alpha\frac{\partial}{\partial y}\left[\frac{1}{R}\frac{\partial}{\partial R}(Rv_R^t)\right]-\alpha\frac{\partial^2}{\partial y^2}v_y^t. \quad (3.56)$$

$V_R^{t+\Delta t}$ is first found from Eq. (3.55); it is then substituted into Eq. (3.56) to solve for $V_y^{t+\Delta t}$. For even-numbered time steps they are advanced in reverse order as

$$\frac{v_y^{t+\Delta t}-v_y^t}{\Delta t}-\alpha\frac{\partial^2}{\partial y^2}v_y^{t+\Delta t}=F_y^t-\alpha\frac{\partial^2}{\partial y^2}v_y^t, \quad (3.57)$$

$$\frac{v_R^{t+\Delta t}-v_R^t}{\Delta t}-\alpha\frac{\partial}{\partial R}\left[\frac{1}{R}\frac{\partial}{\partial R}(Rv_R^{t+\Delta t})\right]-2\alpha\frac{\partial^2}{\partial R\partial y}v_y^{t+\Delta t}$$

$$=F_R^t-\alpha\frac{\partial}{\partial R}\left[\frac{1}{R}\frac{\partial}{\partial R}(Rv_R^t)\right]-2\alpha\frac{\partial^2}{\partial R\partial y}v_y^t. \quad (3.58)$$

$v_y^{t+\Delta t}$ is first found from Eq. (3.57); it is then substituted into Eq. (3.58) to solve for $v_R^{t+\Delta t}$. The mixed partial derivative terms of the semi-implicit operator in Eqs. (3.56) and (3.58) are multiplied by a factor of two to make up for the fact that they appear half as often as other second derivative terms.

All four equations require only a simple tridiagonal matrix solver. Our new scheme, therefore, is very fast to execute; it results in only about a ten percent increase of computer time per single time step compared with the original scheme that is mostly explicit. The size of the executable file remains essentially unchanged because the tridiagonal solver requires very little work space and it has already been introduced in the code to handle the resistivity term using the ADI method.

The numerical stability of the code, on the other hand, improves dramatically with our new scheme that approximately

removes the fast compressional wave step size restriction. The maximum step size can be typically increased by a factor of one to three times the aspect ratio for a divertorless tokamak and by a factor of somewhat less than the aspect ratio for a poloidal divertor tokamak. Because the increase in the CPU time requirement per single time step is so small, the overall code efficiency increases tremendously.

Stability alone does not ensure a good numerical scheme, however. Both accuracy and consistency need to be examined. To this end, we have conducted very extensive numerical tests comparing the mostly explicit scheme and the new, efficient semi-implicit scheme. Grid convergence, step size convergence, linear and nonlinear evolution of m=2, n=1 and m=1, n=1 resistive modes were all found to be satisfactory. Detailed comparisons in a divertorless geometry and in a poloidal divertor geometry are presented in chapters 4 and 5, respectively.

3-4-3. Attempts to further improve code efficiency

A natural extension of the above work would be to apply an operator splitting method to a semi-implicit term that removes the shear Alfven step size restriction as well. The simplest choice for the semi-implicit term would be an isotropic operator $\nabla^2\mathbf{v}$ as in Ref.68. We simplified this further by ignoring the weak couplings of v_R and v_ζ due to the toroidal

curvature. This allows us to decouple the R and ζ components of the velocity advancement equation.

To avoid a large band matrix problem that results from partial derivatives in both the R and y directions, we tried several operator splitting methods. One such method advances v_R in two steps as

$$\frac{v_R^{t^*}-v_R^t}{\Delta t} - \alpha\frac{1}{R}\frac{\partial}{\partial R}\left(R\frac{\partial v_R^{t^*}}{\partial R}\right) = F_R - \alpha\frac{1}{R}\frac{\partial}{\partial R}\left(R\frac{\partial v_R^t}{\partial R}\right), \qquad (3.59)$$

$$\frac{v_R^{t+\Delta t}-v_R^{t^*}}{\Delta t} - \alpha\left[\frac{\partial^2 v_R^{t+\Delta t}}{\partial y^2} - \frac{n^2}{R^2}v_R^{t+\Delta t}\right] = -\alpha\left[\frac{\partial^2 v_R^t}{\partial y^2} - \frac{n^2}{R^2}v_R^t\right], \qquad (3.60)$$

where n is the toroidal mode number. v_y and v_ζ are advanced similarily.

Unfortunately, all the methods tried for the semi-implicit operator were found to be highly dispersive and impractical to use. Throughout this thesis research the semi-implicit scheme described in sections 3-4-1 and 3-4-2 was used very extensively and benchmarked against the results obtained with the mostly explicit scheme.

3-5. Code Diagnostics

A numerical experiment conducted with the RPD code yields an enormous amount of data and it is not practical to store it all, not to mention subjecting it to a thorough examination. Proper diagnostic routines are indeed a crucial

part of the code to facilitate efficient production runs.

During a run RPD keeps track of the temporal evolution of the toroidal, nontoroidal(poloidal plus radial), and total energies of the magnetic and kinetic energy components for each Fourier component. The volume integral for each component can be reduced to a 2-D integral on a constant toroidal angle plane because of a spectral representation in the toroidal direction. RPD also computes the 'instantaneous' growth rates of magnetic and kinetic components of each toroidal mode on time intervals of a few Alfven times. This is done by assuming an exponential growth of the mode as B (or v) $\propto e^{\gamma t}$ over the time interval from t to $t+\Delta t$ and solving for the growth rate γ using the energy of the mode at time t and $t+\Delta t$.

The individual Fourier components of the magnetic field, plasma current density, flow velocity and pressure, and their total values can be plotted on various toroidal angle cross sections in the course of a simulation run. To keep the size of the graphics files manageable, however, we usually plot them only on the midplane at $\zeta = 0$ at the end of each run segment.

To efficiently unravel the global structure of the instabilities, we have developed two diagnostic routines, FLOW and HFLUX, that are separate from RPD. FLOW plots a 2-D flow pattern of the plasma at a desired constant toroidal angle plane. This helps us visualize the global dynamic structure of the instabilities. HFLUX plots an approximate helical flux

function by subtracting from the calculated magnetic field a shearless field that is resonant at the mode rational surface of interest. (The exact helical flux function cannot be constructed because of the truly 3-D nature of the code.) This allows us to make a quick examination of the island structure.

A distinguishing feature of a 3-D magnetic geometry, however, lies in the interactions of modes of incommensurate helicity. This could lead to stochasticity of the magnetic field lines when the magnetic perturbations are sufficiently large. To properly identify such regions and to understand the exact magnetic field structure, we need to follow the field lines and generate puncture (Poincaré) plots. It turns out that one of three input options of the field line tracing code TUBE[69] is a 1-D spectral representation of the magnetic field. We have successfully interfaced TUBE with RPD outputs and used it extensively to study the development of stochasticity in nonlinear simulations of both divertorless and poloidal divertor tokamak plasmas with RPD.[43]

Chapter 4. RESISTIVE MHD INSTABILITIES IN A DIVERTORLESS TOKAMAK

4-1. Introduction

A square cross-section divertorless tokamak is a simple and convenient choice for testing our 3-D resistive MHD initial value code RPD. The shape of the wall boundary matches perfectly with the arrangement of the grid points. By not including a poloidal divertor we eliminate a potential source of numerical error that could contaminate the code results. Noncircularity does change the details of the linear and nonlinear behavior of resistive instabilities by modifying the equilibrium and/or by coupling modes with the same toroidal but different poloidal mode numbers.[57,70,71] Nevertheless, the basic characteristics of an instability should conform to those in a circular cross-section tokamak if the mode rational surface is moved sufficiently far away from the region where the flux surface is considerably noncircular. This suggests that by making a judicious choice for the equilibrium the standard theoretical and numerical results in a circular cross-section tokamak,[54,60,72,73] such as the resistivity scaling of the linear growth rate, can be used to check the correctness of RPD.

A rigorous test of RPD requires detailed comparisons of the RPD results with the results obtained with other resistive MHD codes for the same equilibrium input. Unfortunately, we did

not have access to other initial value codes that were designed for a square cross-section tokamak including toroidal effects. Another possibility was to develop a linear boundary-layer code using a Δ' formalism.[1,72] Although this option would allow us to check the linear behavior of the tearing modes with $m > 1$ for sufficiently high S, it cannot be extended to a nonlinear regime or to a poloidal divertor geometry. In view of our main objective of understanding the resistive instabilities in a divertor geometry and the great complexities of developing such a code in a toroidal and noncircular geometry, we did not pursue this option either.

Instead, RPD was run for a large number of cases with different equilibria and input parameters. The code reproduced the standard theoretical and numerical results pertaining to the tearing and resistive kink modes in a divertorless tokamak. Significant efforts were made to demonstrate the convergence of the solution by changing the grid size, the time step size and a number of Fourier harmonics for selected cases. The new semi-implicit scheme was compared very extensively with the mostly explicit scheme to check stability, accuracy, and consistency of the scheme. All these allowed us to collect a sufficient data base to conclude that our RPD code is essentially correct and that our semi-implicit scheme is indeed a powerful numerical method for dramatically improving the code efficiency.

In sections 4-2 and 4-3 we present the simulation results for the cases in which either the m=2,n=1 tearing mode is dominant or the m=1,n=1 resistive kink mode is dominant. Each section is broken up into three parts: description of MHD equilibrium inputs, linear results, and nonlinear results.

4-2. m=2,n=1 Tearing Mode Dominant Case

4-2-1. MHD equilibria

Over a dozen divertorless tokamak equilibria with $1 < q_{axis} < 2$ have been considered in our study. (This number does not include equilibria with the same machine and plasma parameters but different grid size.) In Table 4-1 we list some key parameters of five equilibria whose linear and/or nonlinear results are discussed in sections 4-2-2 and/or 4-2-3.

In all five cases the toroidal current density is parameterized[73] approximately as $(1/R)\,[1+(\rho_\psi/\rho_c)^{2\lambda}]^{-(1/\lambda)}$, where ρ_ψ is the distance from the magnetic axis and it is normalized to a, one half the width of the square cross section. ρ_c is the distance between the magnetic axis and a particular flux surface. We choose this flux surface to be the one that crosses the midplane at the halfway point between the magnetic axis and the outer wall. λ is set equal to 3.24 to permit a fairly broad profile with a steep J_ζ gradient in the vicinity of the q=2 surface. The plasma beta is chosen to be less than 0.01 percent in all five cases; this makes the plasma essentially

force free.

	aspect ratio	q_{axis}	axis shift	$\left.\frac{dq}{d\psi}\right\|_{q=2}$
Equil.#1	5.0	1.80	0.053	11.1
Equil.#2	1.5	1.52	0.18	16.4
Equil.#3	5.0	1.52	0.053	15.6
Equil.#4	15.0	1.54	0.018	15.9
Equil.#5	50.0	1.54	0.0053	16.0

Table 4-1. Five equilibria with $1 < q_{axis} < 2$. The axis shift and $dq/d\psi$ at the q=2 surface are normalized to a(one half the width of the square) and $(B_{\zeta 0}\,aR)^{-1}$.

The contour plots of the poloidal flux function ψ and the plots of J_ζ and q profiles on the midplane of these five equilibria are shown in Figs. 4-1 to 4-5. The q=2 surface is placed sufficiently far away from the square wall to lessen the noncircularity effect. The primary difference between Equil.#1 and Equil.#3 is the q value on the magnetic axis. This affects the proximity of the q=2 surface to the central region where the J_ζ and q profiles are flat. Equil.#2, #3, #4, and #5 constitute a sequence of MHD equilibria with increasing aspect ratio but almost identical $q = q(\psi)$.

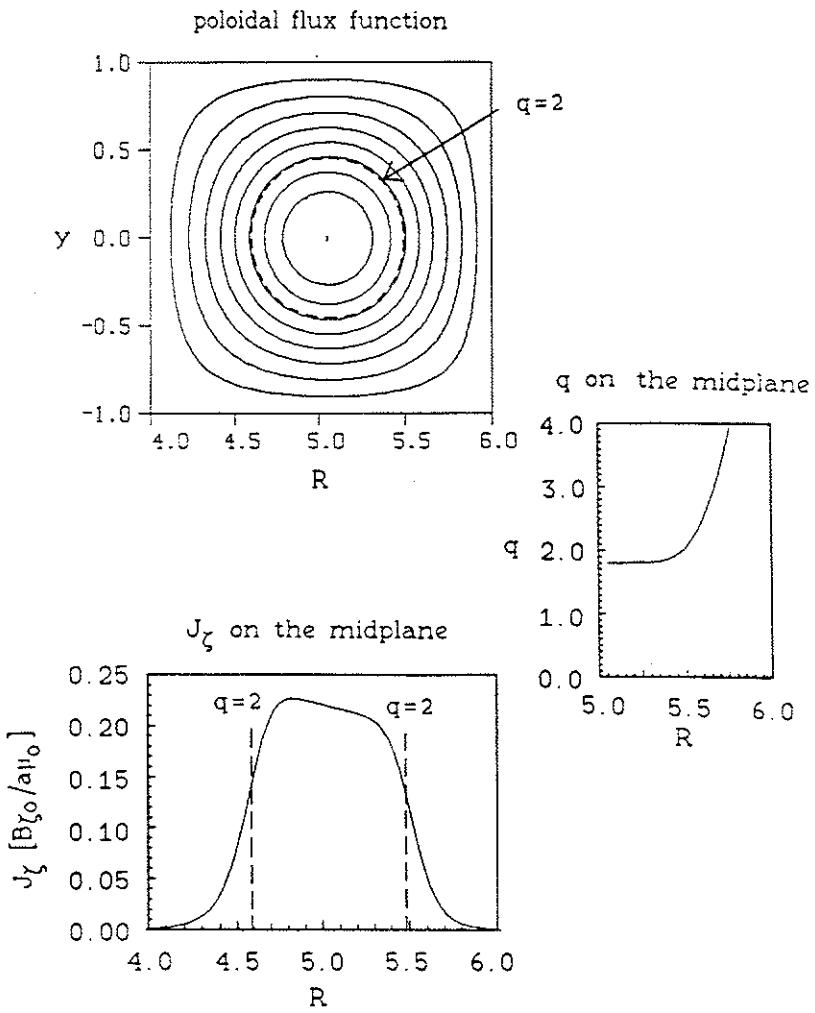

Fig. 4-1. Contour plot of ψ and plots of J_ζ and q on the midplane for Equil. #1. ψ contour levels are equally spaced between their minimum and maximum values.

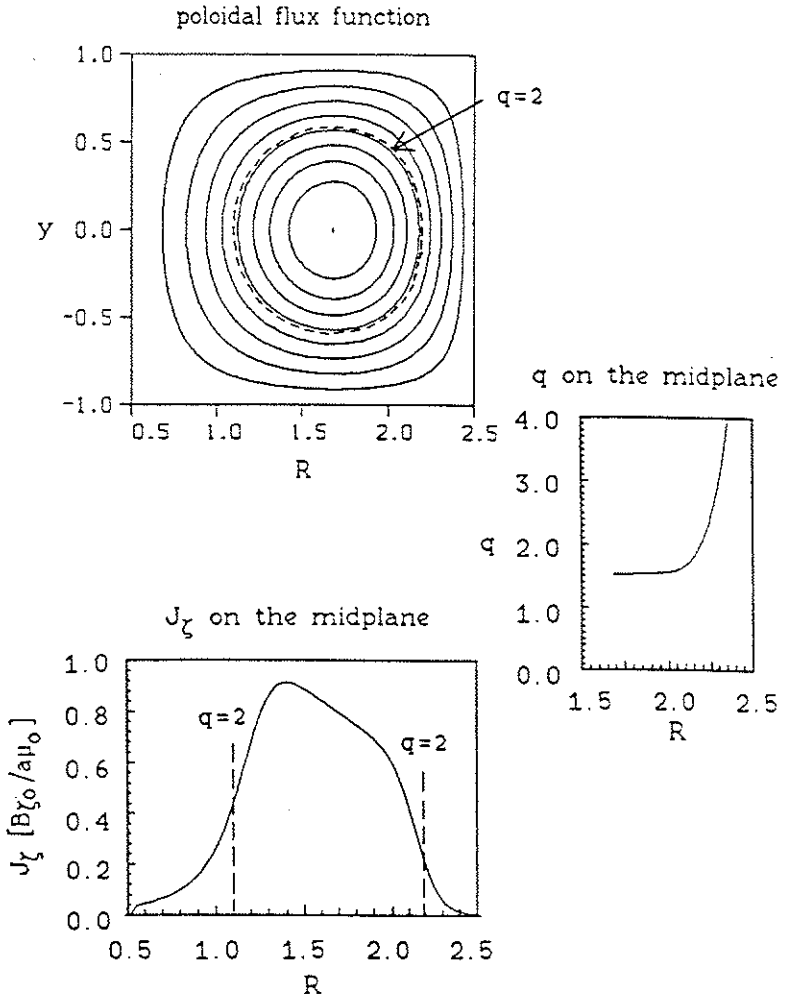

Fig. 4-2. Contour plot of ψ and plots of J_ζ and q on the midplane for Equil. #2. ψ contour levels are equally spaced between their minimum and maximum values.

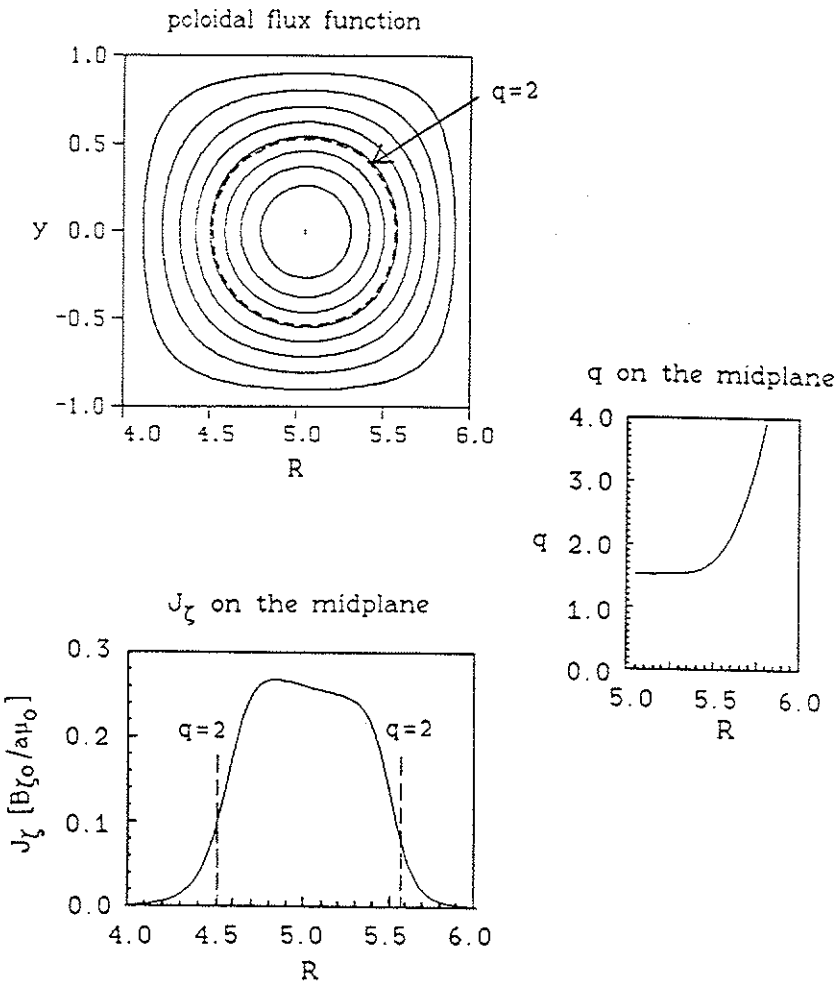

Fig.4-3. Contour plot of ψ and plots of J_ζ and q on the midplane for Equil.#3. ψ contour levels are equally spaced between their minimum and maximum values.

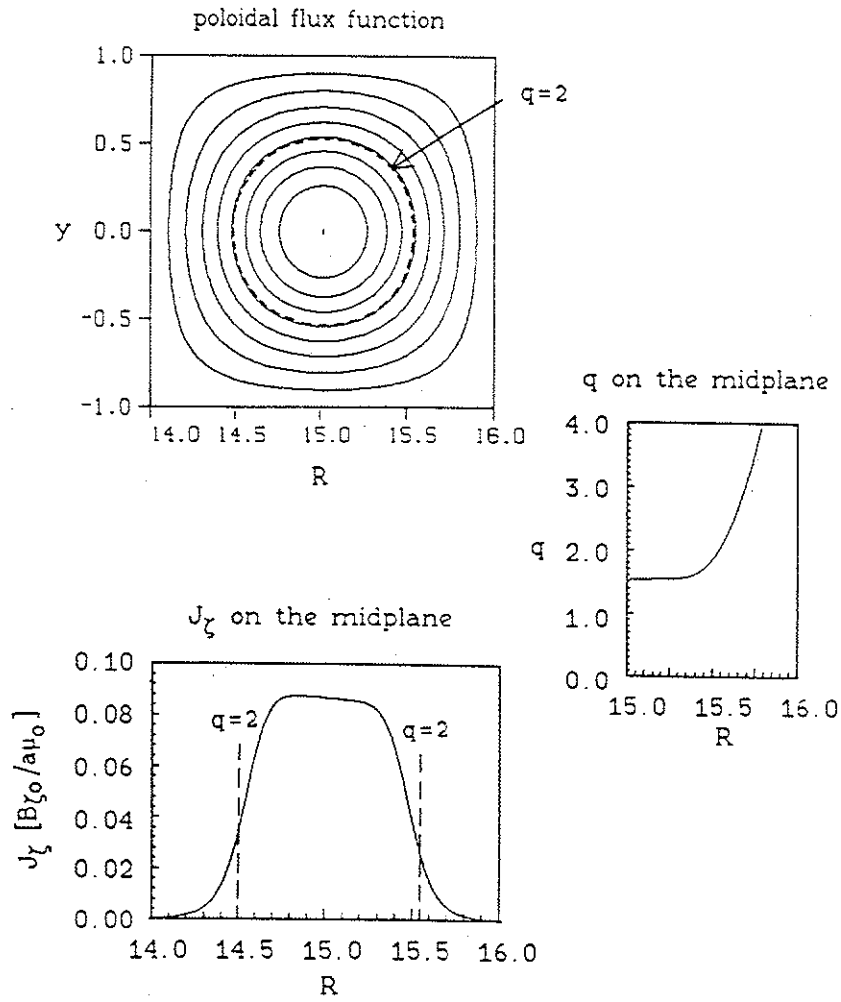

Fig.4-4. Contour plot of ψ and plots of J_ζ and q on the midplane for Equil.#4. ψ contour levels are equally spaced between their minimum and maximum values.

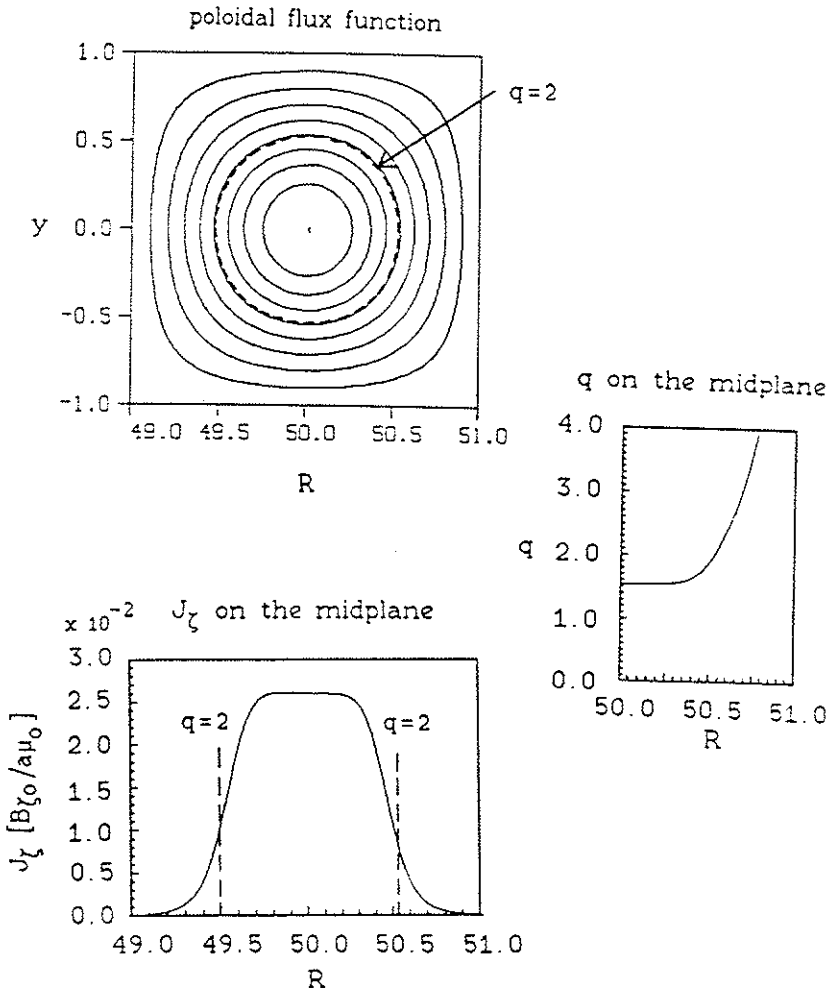

Fig.4-5. Contour plot of ψ and plots of J_ζ and q on the midplane for Equil.#5. ψ contour levels are equally spaced between their minimum and maximum values.

4-2-2. Linear results

For a linear simulation we keep only the linear terms of the n=1 component (both the $n=1^+$ and 1^- terms which correspond to Fourier cosine and sine terms) in addition to the axisymmetric (n=0) component that is frozen in time. Because of our 1-D spectral, 2-D finite-difference spatial representation, all the helical modes with $|m| \geq 2$ and n=1 are effectively included in the calculations. The cut-off at high m depends on the number of spatial grid points included in the calculation. For our choice of equilibria, however, the m=2, n=1 tearing mode is found to be invariably dominant and the linear results can be used to extract the behavior of the m=2, n=1 tearing mode.

Equil.#1 was used very extensively to test our RPD code and to compare the mostly explicit and the new semi-implicit schemes. The eigenfunctions obtained with the two numerical schemes are found to be in very good agreement except for the somewhat smoother fine structure in the case of the semi-implicit scheme.

To illustrate this, we present in Figs.4-6 to 4-8 the plots of the perturbed J_ζ on the midplane at ζ=0 degree and the plasma flow patterns at ζ=0 and 90 degrees as examples. The temporal step sizes used in the two runs are 0.0125 τ_A (= 0.0025 τ_{Hp}) for the mostly explicit scheme and 0.1 τ_A (=0.02 τ_{Hp}) for the new semi-implicit scheme. The semi-implicit

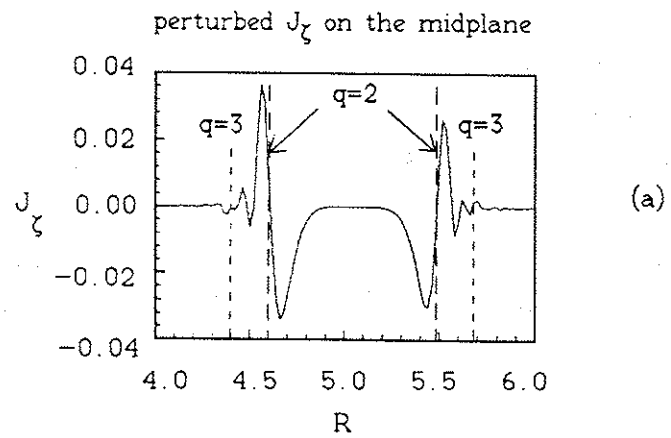

(a)

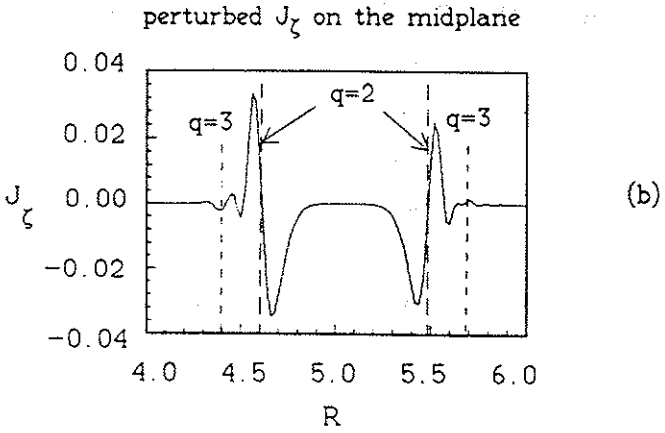

(b)

Fig. 4-6. Plots of the perturbed J_ζ on the midplane calculated with (a) the mostly explicit scheme and (b) the new semi-implicit scheme. In addition to the m=2, n=1 tearing mode that is dominant, a small but finite m=3, n=1 mode is excited.

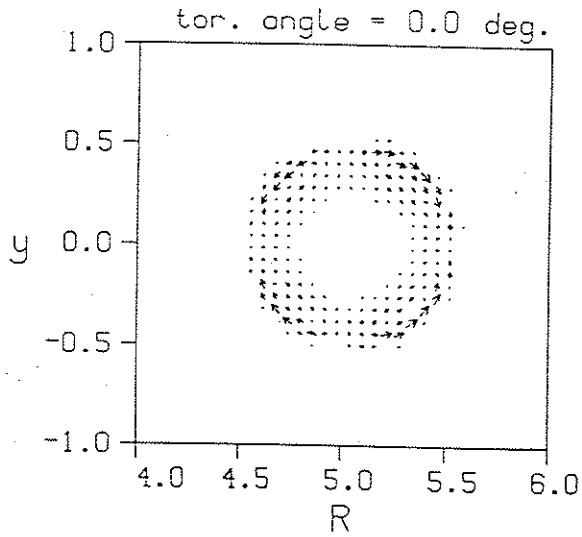

(a)

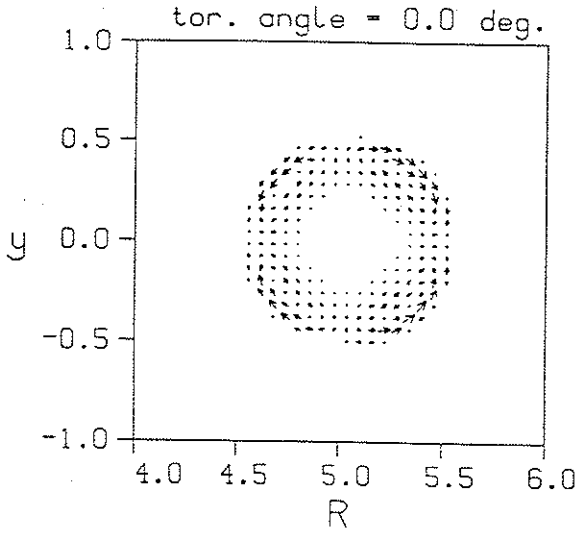

(b)

Fig. 4-7. Plasma flow patterns at ζ=0 calculated with (a) the mostly explicit scheme and (b) the semi-implicit scheme. A vector is plotted at the point where the flow magnitude is greater than three percent of the maximum value.

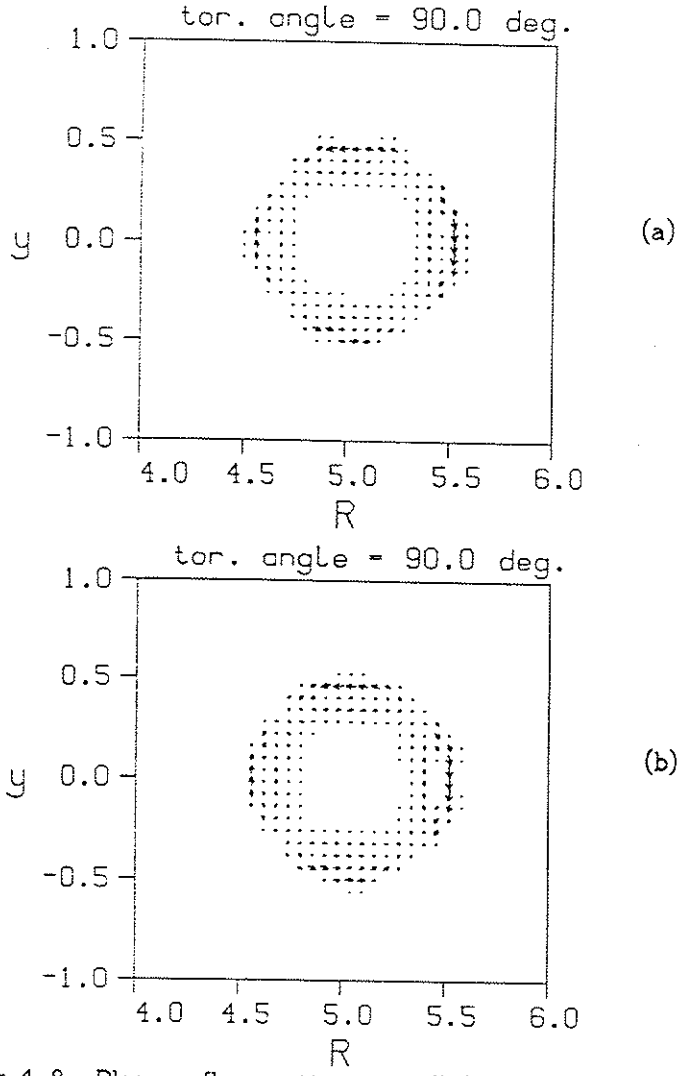

Fig. 4-8. Plasma flow patterns at ζ=90 degrees calculated with (a) the mostly explicit scheme and (b) with the new semi-implicit scheme. Along with Fig. 4-7, the force on the plasma is shown to be that of the m=2, n=1 tearing mode.

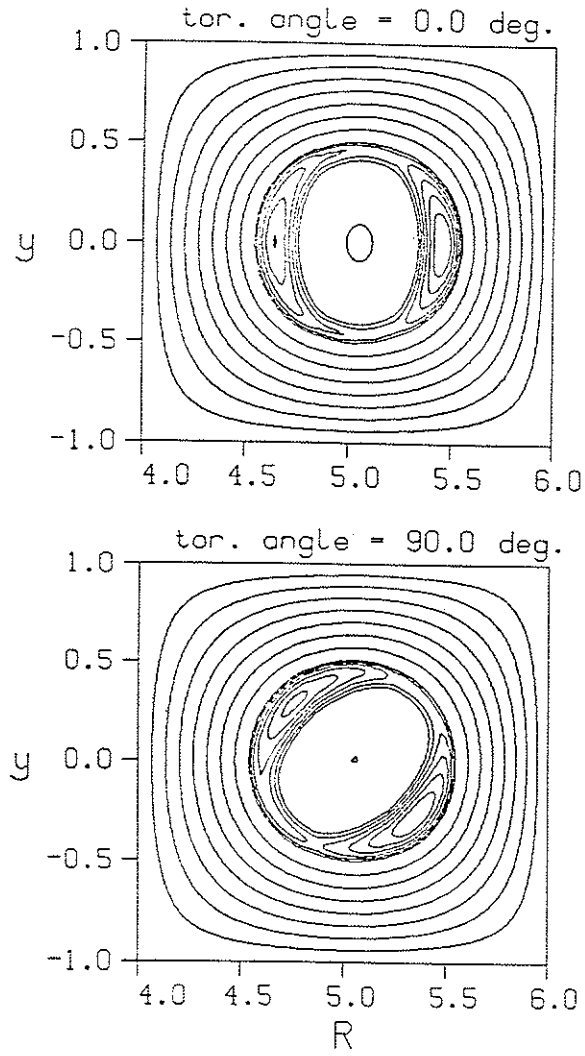

Fig. 4-9. m=2, n=1 magnetic island at ζ=0 and 90 degrees calculated with the mostly explicit scheme. The semi-implicit run yields virtually identical results.

coefficient α is chosen to be 0.05. In both cases the grid size of 100 by 100 is used and the magnetic Reynolds number S is assumed to be 10^4 everywhere. The m=2, n=1 helical flux function at ζ=0 and 90 degrees is shown in Fig. 4-9 to illustrate that an m=2, n=1 magnetic island is indeed present. Here, we only include the case with the mostly explicit scheme because the results obtained with the two schemes are virtually identical. It must be emphasized that the temporal step size $\Delta t = 0.1\tau_A$ for the semi-implicit run exceeds the numerical stability limit of the mostly explicit run by about a factor of seven.

As for the eigenvalue, the semi-implicit scheme has a tendency to reduce the linear growth rate of the n=1 component as the time step size is increased. Equil.#1 with a coarse grid of 60 by 60 was used extensively to examine this effect. A rule of thumb for the reduction in the growth rate is that it is within 15 to 20 percent of that calculated by the explicit scheme as long as the product $\alpha\Delta t$ is kept smaller than 0.01 in fast Alfvén units.

Fig. 4-10 compares the mostly explicit scheme and the semi-implicit scheme with α=0.05 for different temporal step sizes. The maximum step size for numerical stability is increased from $0.027\tau_A$ ($=0.0054\tau_{Hp}$) to $0.15\tau_A$ ($=0.029\tau_{Hp}$) with only a modest sacrifice in accuracy. Because the semi-implicit scheme requires only about 10 percent more

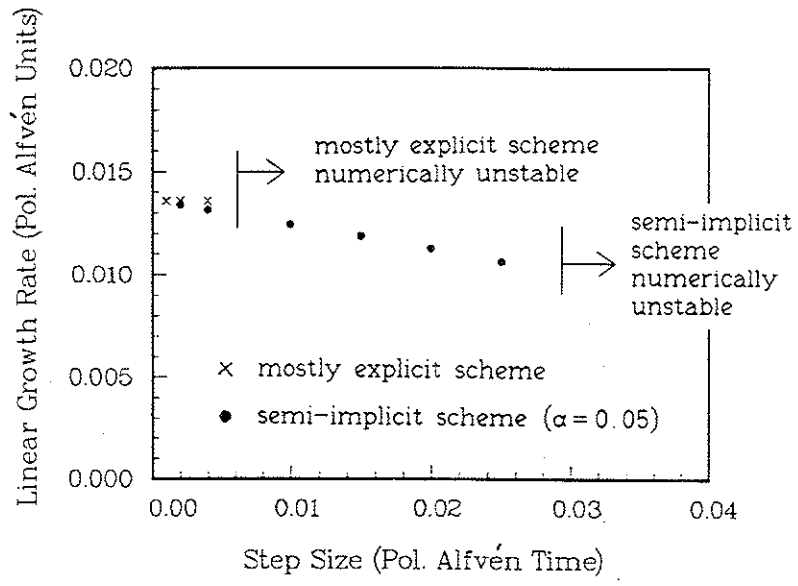

Fig. 4-10. Effect of temporal step size on the linear growth rate of the n=1 component (m=2, n=1 tearing mode dominant) for Equil.#1. Results with the mostly explicit and the semi-implicit schemes are compared.

computer time per time step than the mostly explicit scheme this represents a saving of computer time by about a factor of the aspect ratio. In the case of a larger grid size the saving is even greater; the maximum step size for numerical stability with the mostly explicit scheme decreases linearly with the grid spacing while it remains almost unchanged with the semi-implicit scheme. In fact, for large grids the semi-implicit scheme becomes a necessity rather than merely a time saving

measure. With the mostly explicit scheme, a typical linear run using the grid size of 100 by 100 would require over six hours of computer time. With the semi-implicit scheme, the computer time can be reduced to under one hour. The program size of such runs is about 3.2 million words in octal.

One way of testing the code and its numerical scheme is to examine the effect of grid size. Fig. 4-11 shows the grid

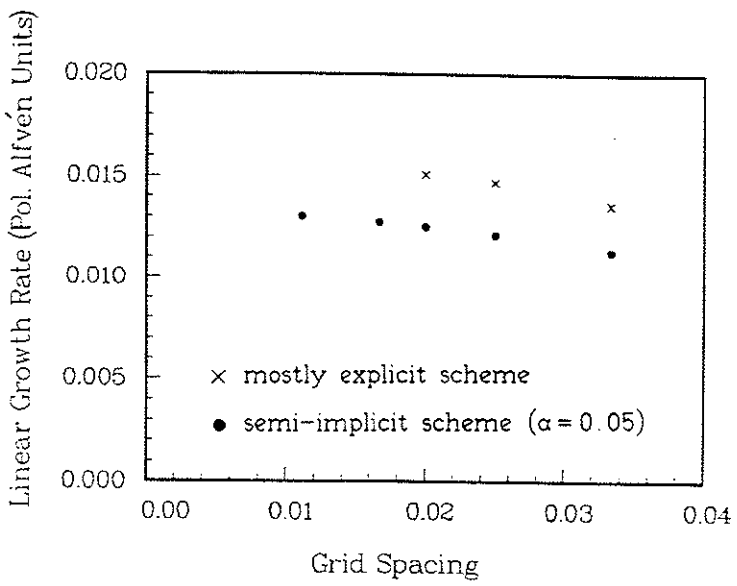

Fig. 4-11. Effect of grid spacing (or reciprocal of one half the grid size) on the linear growth rate of the n=1 component (m=2, n=1 tearing mode dominant) for Equil. #1. Results with the mostly explicit and the semi-implicit schemes are compared.

convergence of the linear growth rate of the n=1 component for Equil. #1 using the mostly explicit and semi-implicit schemes. The grid sizes used are 60 by 60, 80 by 80, and 100 by 100 for both schemes, and 120 by 120 and 180 by 180 for the semi-implicit scheme. Although the linear growth rate increases modestly as the grid resolution improves, its increase tends to level off as the grid spacing go to zero. We conclude that the grid convergence of the code is satisfactory for both numerical schemes.

Next the scaling of the linear growth rate with resistivity is tested using Equil. #1 with a grid size of 60 by 60. Simulations are conducted for both explicit and semi-implicit schemes. (See Fig. 4-12.) At a sufficient high S value of 3×10^4 or larger, the linear growth rate is shown to follow the standard analytic scaling[1,60,73] of $S^{-3/5}$. However, the numerical scaling obtained with RPD deviates greatly from the analytic scaling at low S. This is due to the fact that the assumption that goes into the boundary layer analysis (Δ' formalism) fails as resistivity increases. The deviation is very large in this regime for this equilibrium because of the nearness of the q=2 surface to the region where J_ζ and q are flat. As the resistivity increases, the resistive layer widens and extends to such a region. This results in a reduction of the effective Δ' and the growth rate.

To support this interpretation, the resistivity scaling study

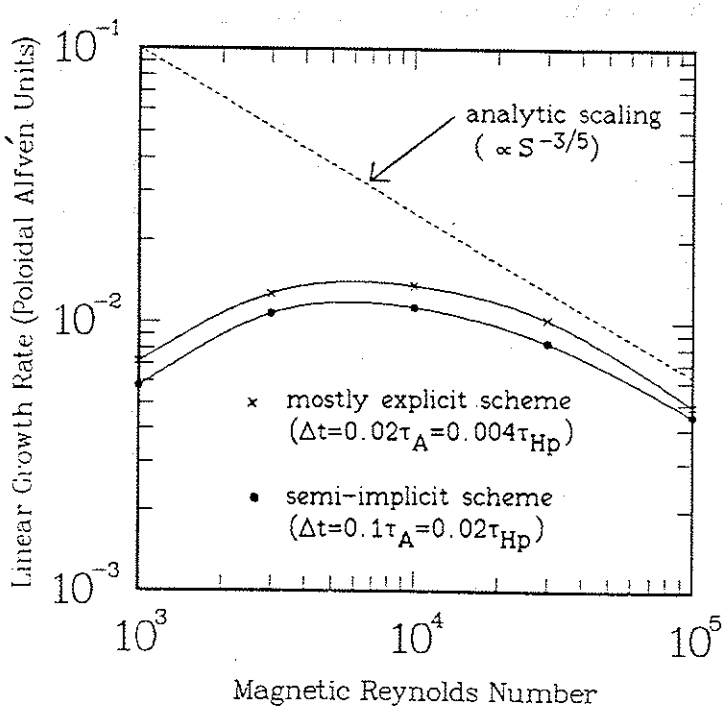

Fig.4-12. Scalings of the linear growth rate of the n=1 component (m=2,n=1 tearing mode dominant) with plasma resistivity. The numerical results of RPD are compared with the standard analytic scaling.

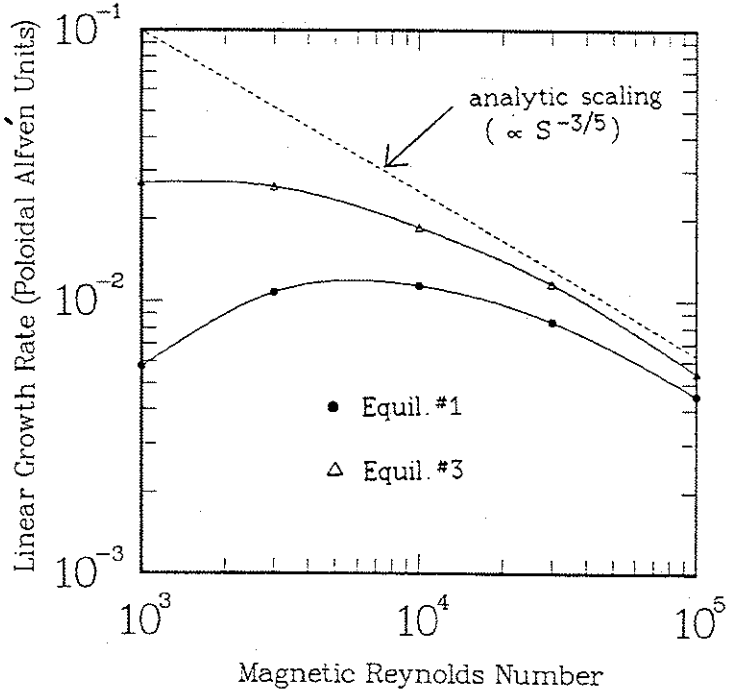

Fig.4-13. Effect of equilibrium profiles on the resistivity scaling of the linear growth rate of the n=1 component (m=2,n=1 tearing mode dominant). RPD results for Equil.#1 and #3 are compared against the standard analytic scaling.

is repeated using Equil.#3 in which the q=2 surface is placed further away from the region where J_ζ and q are flat. The resistivity scalings for the linear growth rates using Equil.#1 and #3 are compared in Fig.4-13. As expected, the analytic and numerical scalings are in good agreement over a wider range of S in the case of Equil.#3.

One of the novel features of our RPD code is that it can be used to study the toroidal effects on resistive instabilities without an ordering assumption. To test the toroidal terms in RPD, we conduct the linear simulations for a sequence of equilibria (Equil.#2 to #5) for which the aspect ratio ranges from

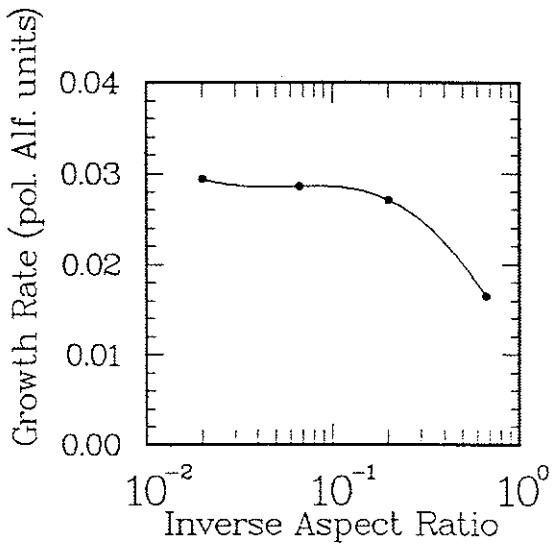

Fig.4-14. Effect of toroidicity on the linear growth rate of the n=1 component (m=2, n=1 tearing mode dominant).

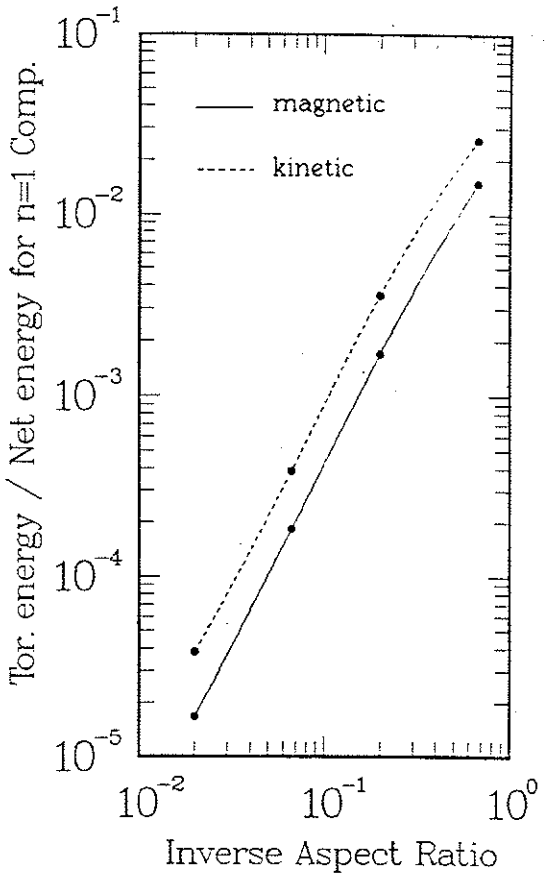

Fig.4-15. Effect of toroidicity on the magnitude of the toroidal component of the perturbation relative to the total perturbation. The ratios of perturbation energies are plotted for both the magnetic and kinetic parts.

1.5 to 50. A significant reduction in the linear growth rate is observed at tighter aspect ratios. (See Fig. 4-14.) This is in agreement with the previously obtained toroidal results.[60,70,74,75] Furthermore, the ratio of the toroidal component of the perturbation to the total perturbation is examined for both the magnetic and kinetic parts. (See Fig. 4-15.) It can be seen that $\tilde{B}_\zeta \sim \epsilon \tilde{B}_{total}$ and $v_\zeta \sim \epsilon v_{total}$, where ϵ is the inverse aspect ratio. This is also in good agreement with the previously obtained toroidal results using the full set of resistive MHD equations,[60] and it confirms the analytic ordering of the reduced set of resistive MHD equations.

4-2-3. Nonlinear results

For a nonlinear simulation we keep both linear and nonlinear terms. As the perturbation amplitude of the n=1 component increases and some of the nonlinear terms become comparable to the linear terms in magnitude, the dynamic evolution of the resistive MHD plasma begins to deviate considerably from that of a linear calculation.[76] When the perturbation increases further, the nonlinear terms can significantly modify the original axisymmetric equilibrium.[8] Not only does this change the growth rate of the n=1 component but it could destabilize the modes that were linearly stable initially.[2] Furthermore, the nonlinear terms can excite directly modes with shorter wavelengths. By the time the

major disruption[7] sets in the plasma becomes almost turbulent. In order to properly simulate the resistive instabilities in a highly nonlinear regime, it is sometimes necessary to include a large number of grid points(~240 by 240) and toroidal Fourier harmonics(~21). Such a run would be beyond the scope of the Cray 2 computer.

Our choice of equilibria allows us to keep physically meaningful nonlinear simulations manageable. By choosing q on the magnetic axis to be greater than 1.50, we can remove the m=3, n=2 tearing mode. This eliminates the possibility of a major disruption of the type proposed in the standard theoretical senario,[16-18] and the m=2, n=1 magnetic island is expected to merely saturate.[8] To test the nonlinear option of our RPD code and the semi-implicit scheme as applied to such a case, we conduct a number of nonlinear simulations using Equil. #1.

Fig. 4-16 summarizes the results of three nonlinear runs each of which includes only three toroidal Fourier harmonics (n=0, 1^+, and 1^-). Equil. #1 is perturbed initially using the result of the linear run. Although the exact paths to the 'final' states are different depending on the numerical scheme, grid size, and viscosity used, the energies of the n=1 component at saturation agree within 15 percent. This translates into a difference of no more than two percent in the width of the magnetic island.

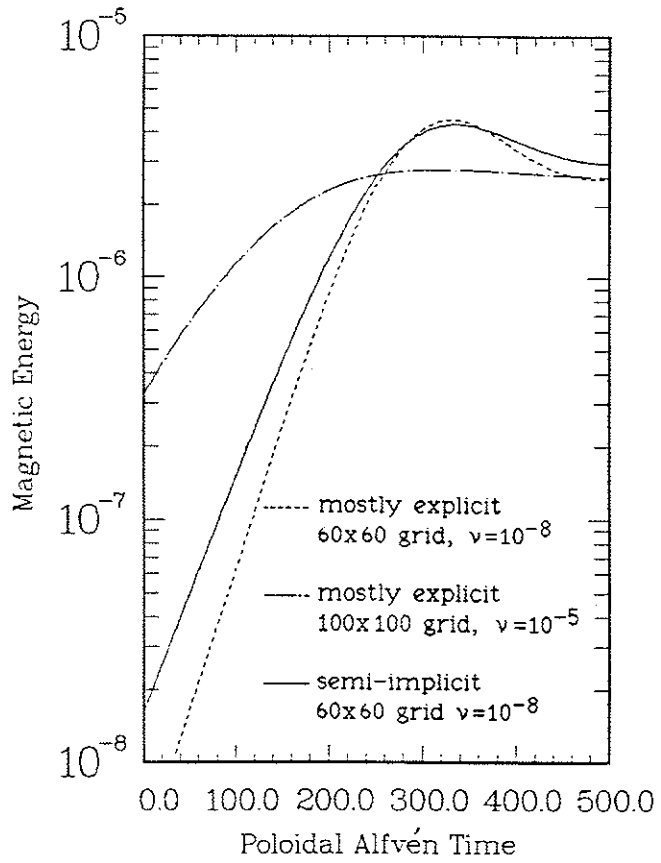

Fig. 4-16. Temporal evolution of the n=1 component (m=2, n=1 tearing mode dominant) of the magnetic energy for three nonlinear runs which each include only three toroidal Fourier harmonics (n=0, 1^+, and 1^-). The magnetic energy is measured in units of $a^3(B_\zeta)^2/2\mu_o$.

Figs. 4-17 and 4-18 show the temporal evolution of the magnetic and kinetic energies for two nonlinear runs which includes five toroidal Fourier harmonics (n=0, 1^+, 1^-, 2^+, and 2^-). The grid size is 60 by 60. The exact paths to the 'final' states are again different. Because the linear growth rate with the explicit scheme is greater than that with the semi-implicit scheme, the run with the explicit scheme reaches the nonlinear saturation sooner. (In terms of computer time, the run with the mostly explicit scheme is much slower. It takes nearly 12 hours of computer time while the run with semi-implicit scheme can be completed in about 2.5 hours.) When the 'final' states are compared, however, the results of the two runs are in very good agreement. This justifies the use of the semi-implicit scheme for nonlinear simulations as well.

Fig. 4-19 on page 113 illustrates the magnetic field structure of the plasma at saturation. The result of our RPD code at 400 τ_{Hp} calculated with a 60 by 60 grid and five Fourier harmonics is used as an input for the magnetic field line tracing code TUBE. The puncture plots at ζ=0 and 90 degrees clearly show a fairly wide m=2, n=1 magnetic island. In addition, an m=3, n=1 magnetic island is revealed near the q=3 surface. Fig. 4-20 shows J_ζ on the midplane. The total and the axisymmetric component of J_ζ are plotted separately. The latter shows the flattening of the current profile in the vicinity of the q=2 surface due to the nonlinear terms.

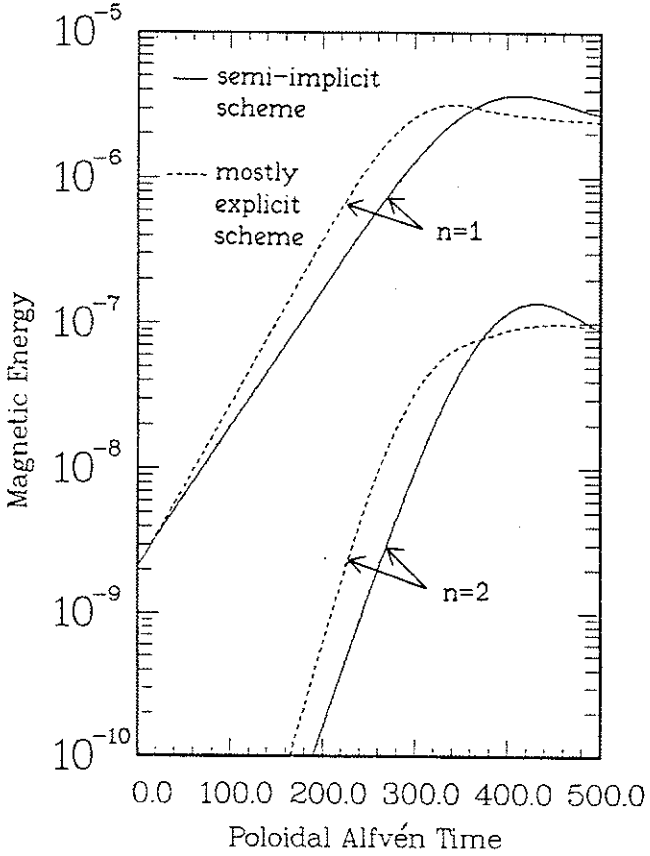

Fig. 4-17. Temporal evolution of the n=1 and 2 components (m=2, n=1 tearing mode dominant) of the magnetic energy. Five Fourier harmonics are included in both runs. The magnetic energy is measured in units of $a^3(B_\zeta)^2/2\mu_o$.

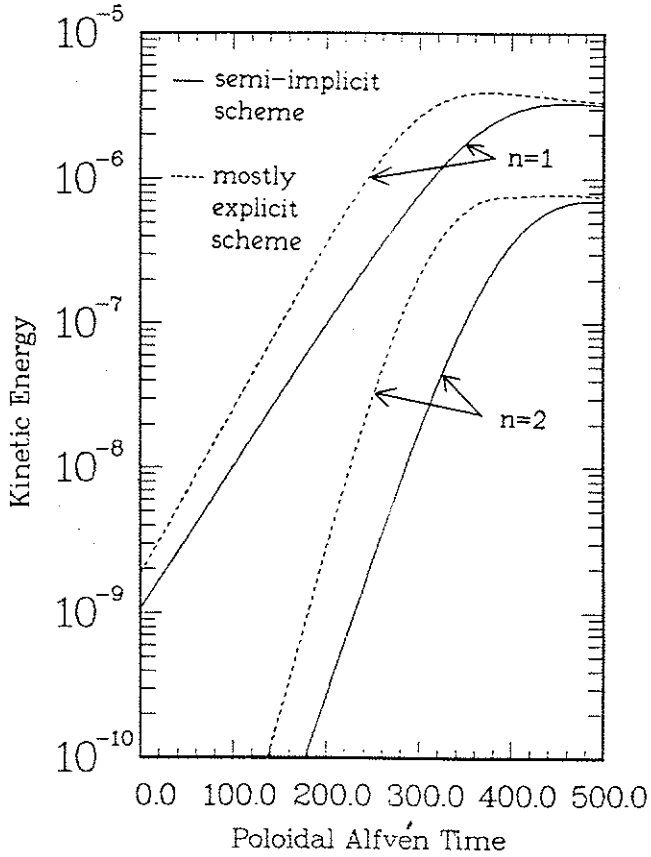

Fig. 4-18. Temporal evolution of the n=1 and 2 components (m=2, n=1 tearing mode dominant) of the kinetic energy. Five Fourier harmonics are included in both runs. The kinetic energy is measured in units of $a^3\rho_o(v_A)^2/2$.

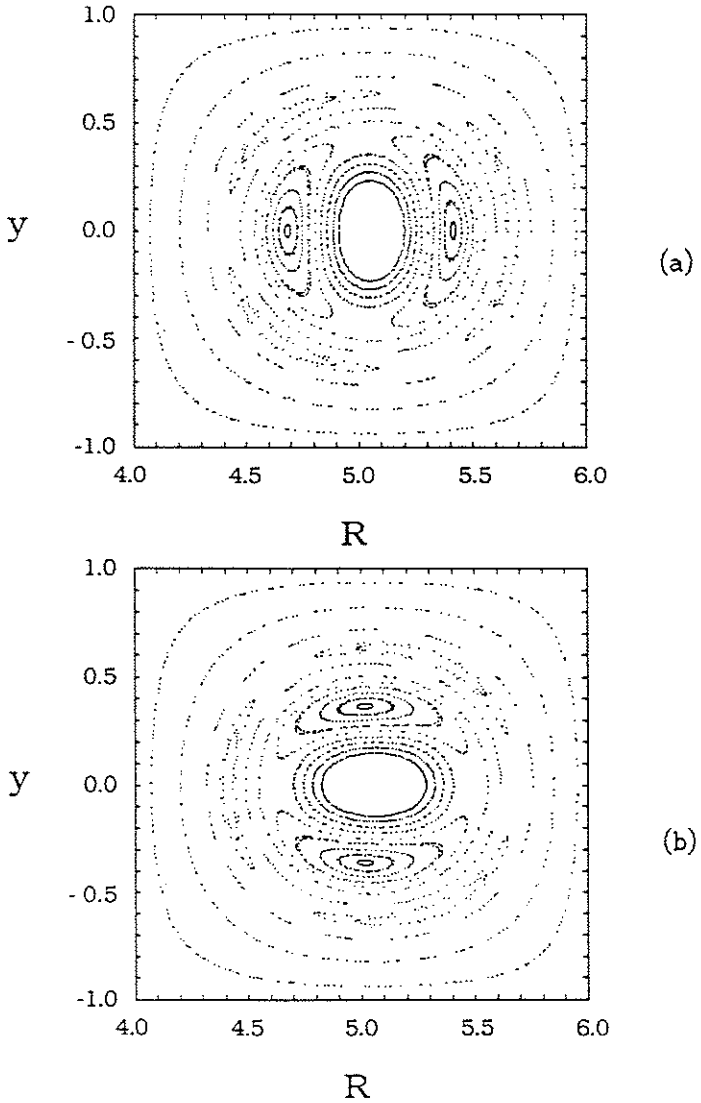

Fig.4-19. Puncture plots of the magnetic field at (a) ζ=0 and (b) 180 degrees at t=400 τ_{Hp}.

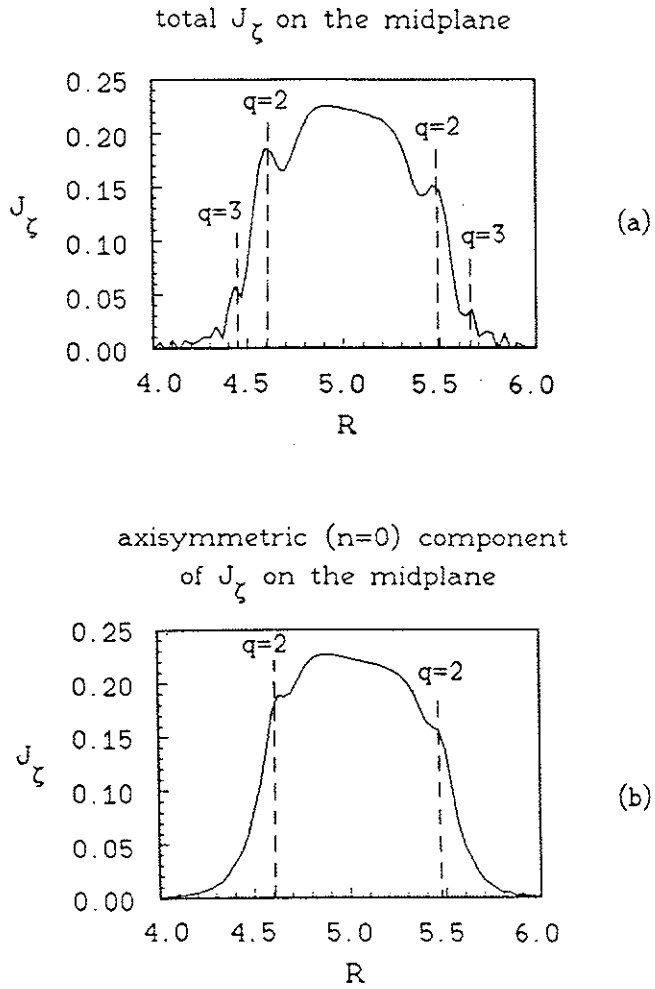

Fig.4-20. (a) The total J_ζ at ζ=0 and (b) the axisymmetric component (n=0) of J_ζ, both on the midplane.

Finally, we comment on the reliability of the above results. It is encouraging to note that the n=1 components are greater than the n=2 components by a factor of 30 for the magnetic energy and by a factor of 3 for the kinetic energy. (See Figs. 4-17 and 4-18.) This suggests fairly good convergence with the number of toroidal Fourier harmonics, especially for the magnetic part. This is also supported by Figs. 4-16 and 4-17; a comparison of the two figures suggests that the n=1 component of the magnetic energies at saturation agrees within 15 percent whether we include three or five Fourier harmonics. Although a highly converged result would undoubtedly require more toroidal Fourier harmonics as well as a finer grid, we believe that the results obtained here are at least qualitatively correct.

4-3. m=1, n=1 Resistive Kink Mode Dominant Case

4-3-1. MHD equilibria

Of a half dozen equilibria that were considered in our studies we focus on only two equilibria. Table 4-2 on page 118 lists some of the key parameters for the two equilibria.

The toroidal current density J_ζ is parametrized in the same way as in Equil. #1 to #5. ρ_c is chosen to be 0.5 on the midplane. To make the gradient of J_ζ near the q=1 surface steeper, however, λ is set to 2.0 and 1.0 for Equil. #6 and #7, respectively. The plasma is essentially force free because the

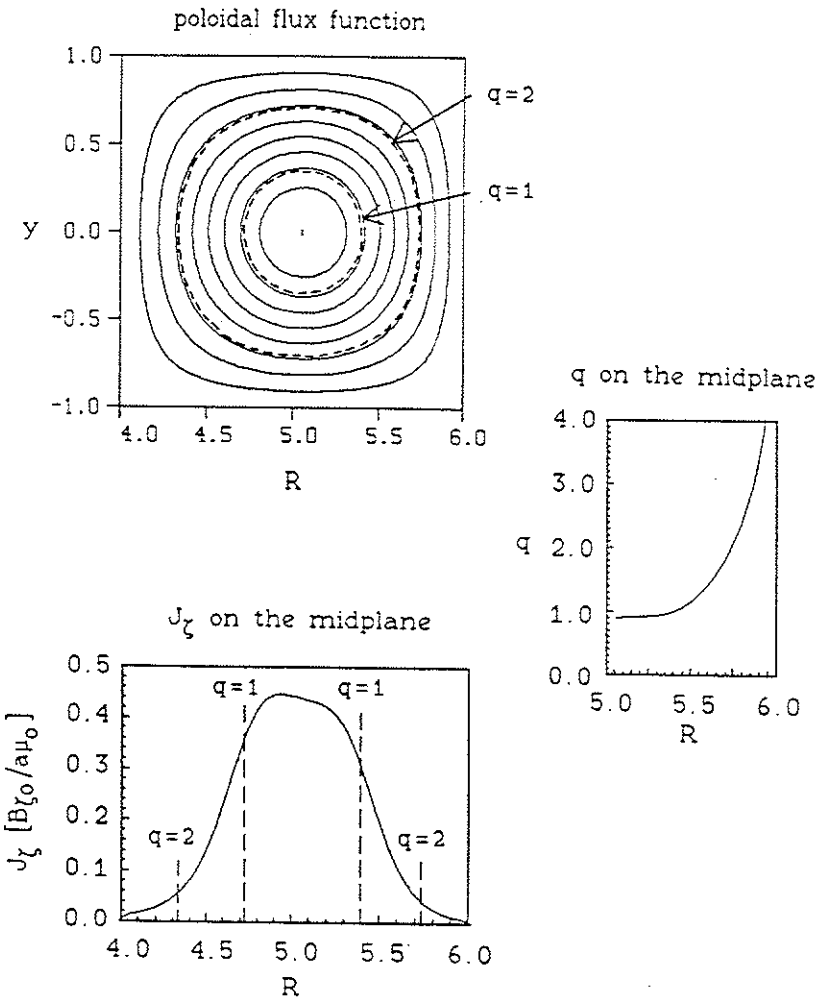

Fig. 4-21. Contour plot of ψ and plots of J_ζ and q on the midplane for Equil. #6. ψ contour levels are equally spaced between their minimum and maximum values.

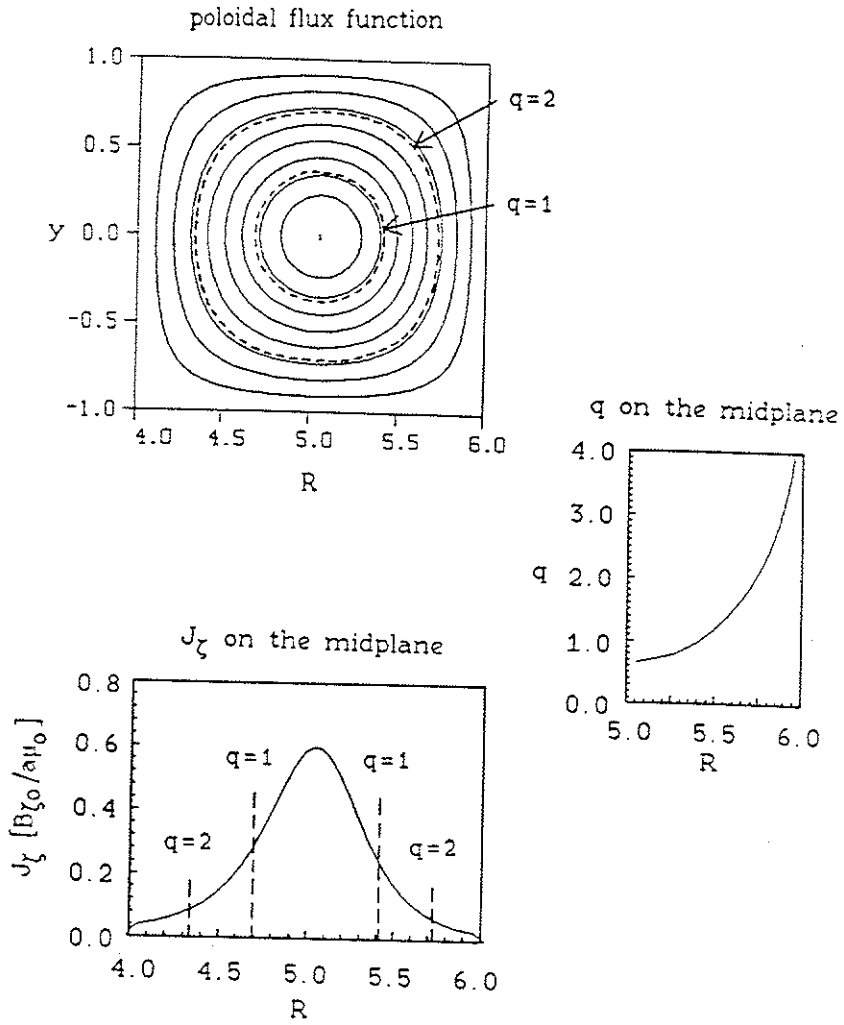

Fig. 4-22. Contour plot of ψ and plots of J_ζ and q on the midplane for Equil.#7. ψ contour levels are equally spaced between their minimum and maximum values.

plasma beta is chosen to be less than 0.01 percent.

	aspect ratio	q_{axis}	axis shift	$\frac{dq}{d\psi}\Big\|_{q=1}$	$\frac{dq}{d\psi}\Big\|_{q=2}$
Equil.#6	5.0	0.90	0.058	2.97	12.8
Equil.#7	5.0	0.66	0.055	5.12	10.8

Table 4-2. Two equilibria with $q_{axis} < 1$. The axis shift and $dq/d\psi$ are normalized as in Table 4-1.

Figs. 4-21 and 4-22 show the contour plots of the poloidal flux function ψ and the plots of J_ζ and q profiles on the midplane. The q=1 surface is deep inside the plasma and the noncircularity effect on the m=1, n=1 resistive kink mode is believed to be negligible. The main differences between Equil.#6 and #7 are the q value on the magnetic axis and the slope of J_ζ and q at the q=1 surface.

4-3-2. Linear results

For a linear simulation we keep the n=0, 1^+, and 1^- components and advance the linear terms of the n=1^+ and 1^- components only. Because of our spatial representation that is spectral in the toroidal direction only, all the helical modes with $|m| \geq 1$ and n=1 are included in our calculation. This includes the m=2, n=1 tearing mode which is fairly robust. Fortunately, the ideal counterpart of the m=1, n=1 resistive kink mode is

neutrally unstable. As a result, the linear growth rate of the m=1,n=1 resistive kink mode is significantly greater than that of the m=2,n=1 tearing mode unless the J_ζ and q profiles are extremely flat near the q=1 surface. This allows us to easily extract the behavior of the m=1,n=1 resistive kink mode.

The mostly explicit and the semi-implicit schemes are compared using Equil.#6. The eigenfunctions obtained with the two schemes are found to be in very good agreement as in the case of Equil.#1 in which the m=2,n=1 tearing mode is dominant. Figs.4-23, 4-24, and 4-25 compare plots of the perturbed J_ζ on the midplane at ζ=0 and the plasma flow patterns at ζ=0 and 90 degrees, respectively. Fig.4-23 shows a small but finite m=2,n=1 mode near the q=2 surface in addition to the dominant m=1,n=1 resistive kink mode. The time step sizes used in the two runs are 0.02 τ_A ($=0.004\tau_{Hp}$) for the most explicit scheme and 0.1 τ_A ($=0.02\tau_{Hp}$) for the semi-implicit scheme. The semi-implicit coefficient α is chosen to be 0.05. In both cases the grid size of 60 by 60 is used and S is assumed to be 10^3 everywhere. The m=1,n=1 helical flux function at ζ=0 and 90 degrees clearly reveals the m=1,n=1 magnetic island. (See Fig.4-26.) The agreement between the two numerical schemes are so good that we omitted the plots of the semi-implicit run results.

Fig.4-27 compares the linear growth rates of the n=1 component calculated with the two numerical schemes over a

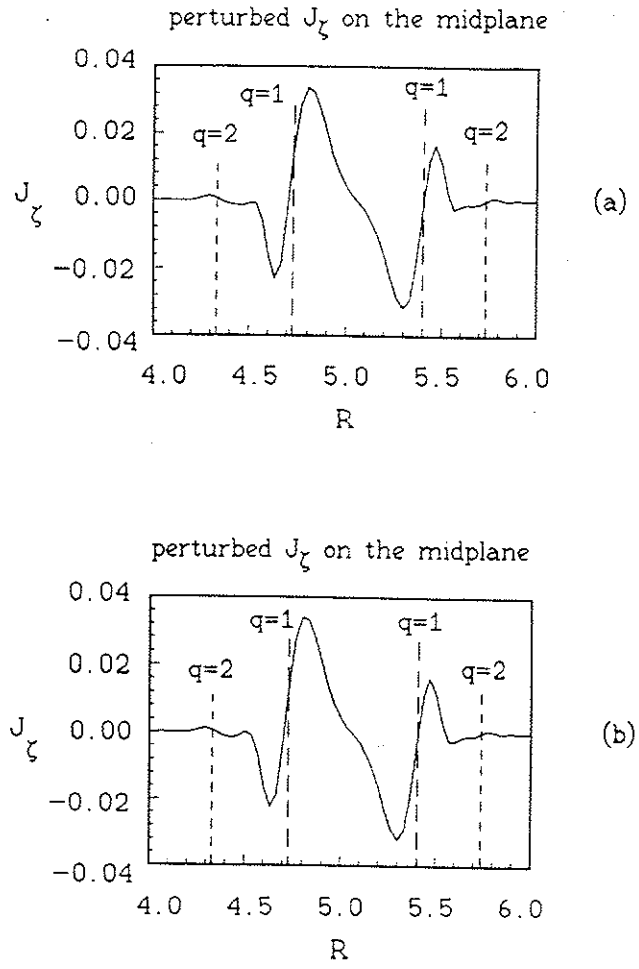

Fig.4-23. Plots of the perturbed J_ζ on the midplane calculated with (a) the mostly explicit scheme and (b) the semi-implicit scheme. In addition to the m=1,n=1 resistive kink mode that is dominant, the m=2,n=1 tearing mode is excited.

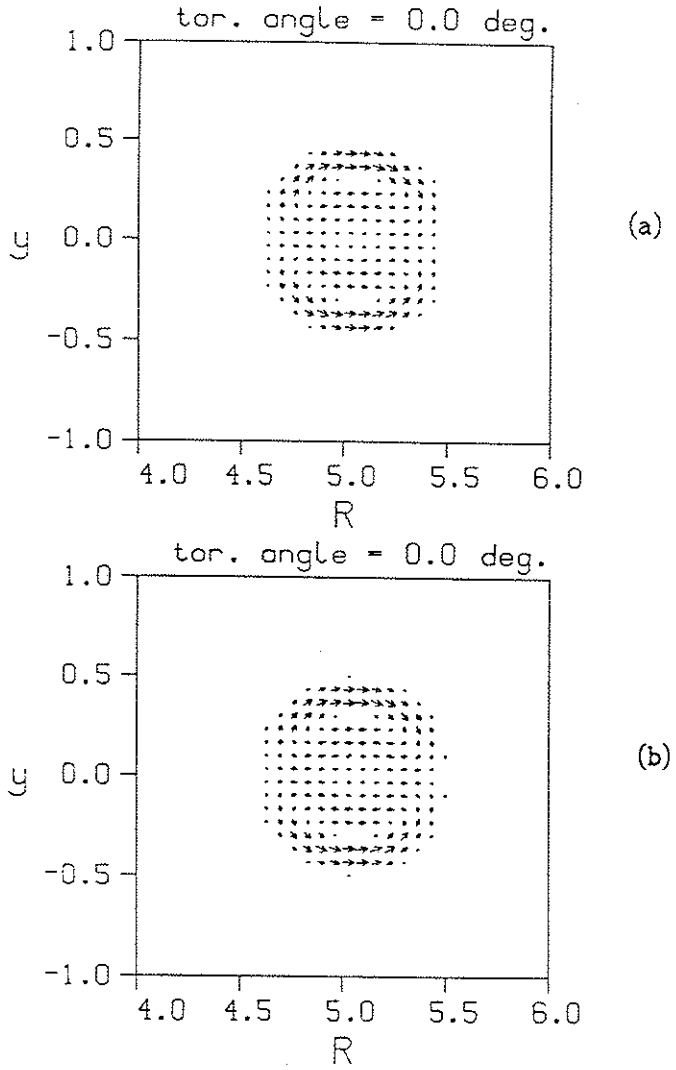

Fig. 4-24. Plasma flow patterns at ζ=0 calculated with (a) the mostly explicit scheme and (b) the semi-implicit scheme. A vector is plotted at the point where the flow magnitude is greater than three percent of the maximum value.

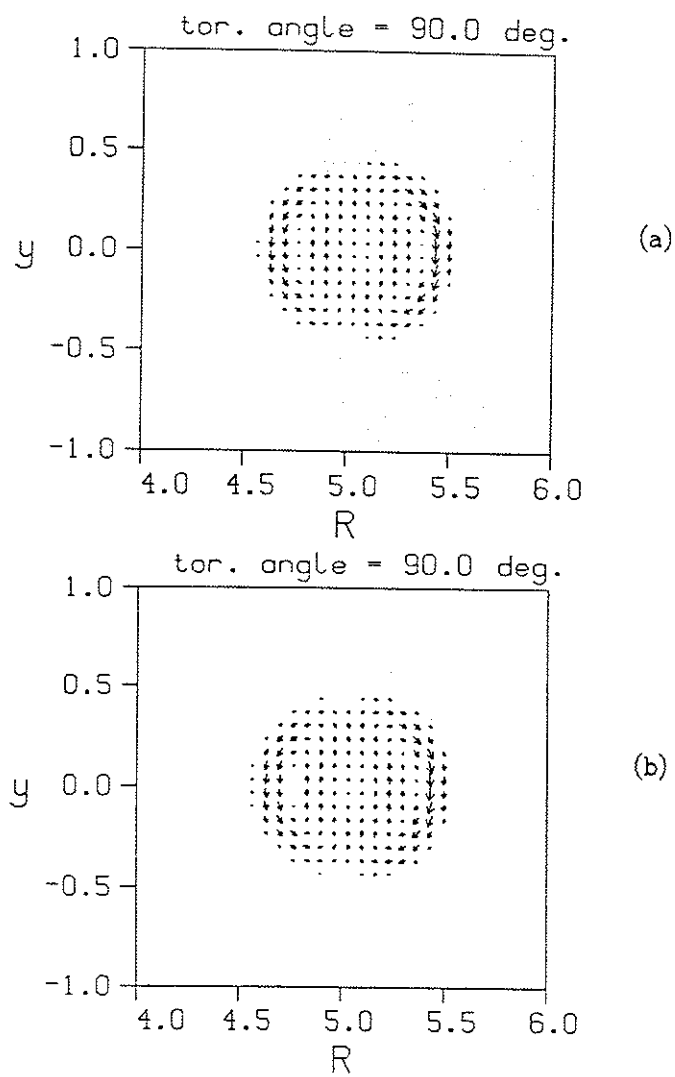

Fig. 4-25. Plasma flow patterns at ζ=90 degrees calculated with (a) the mostly explicit scheme and (b) the semi-implicit scheme. Along with Fig. 4-24, the force on the plasma is shown to be predominantly that of the m=1, n=1 resistive kink mode.

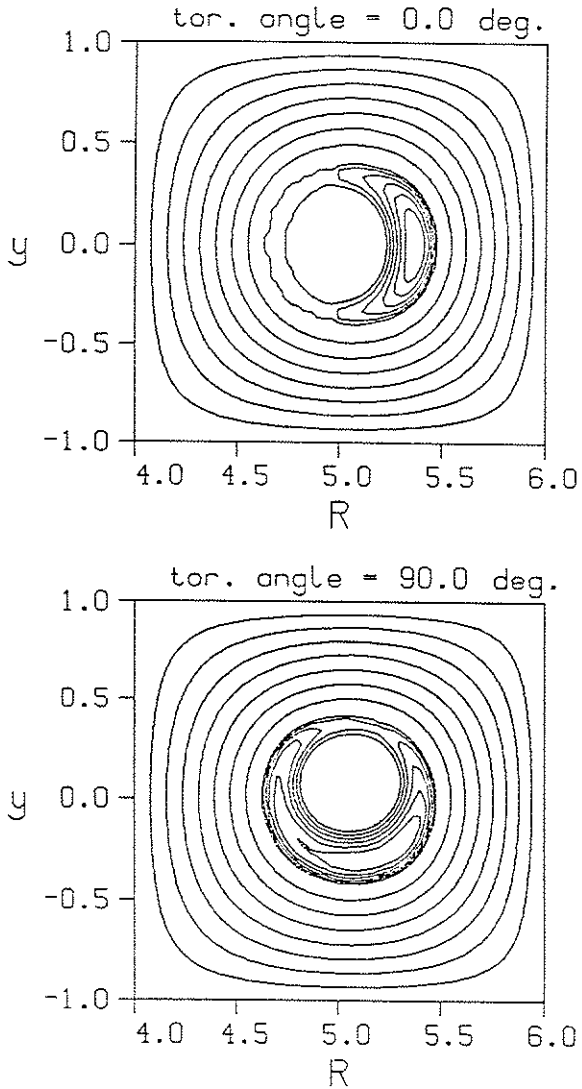

Fig. 4-26. m=1, n=1 magnetic island at ζ=0 and 90 degrees calculated with the mostly explicit scheme. The semi-implicit run yields virtually identical results.

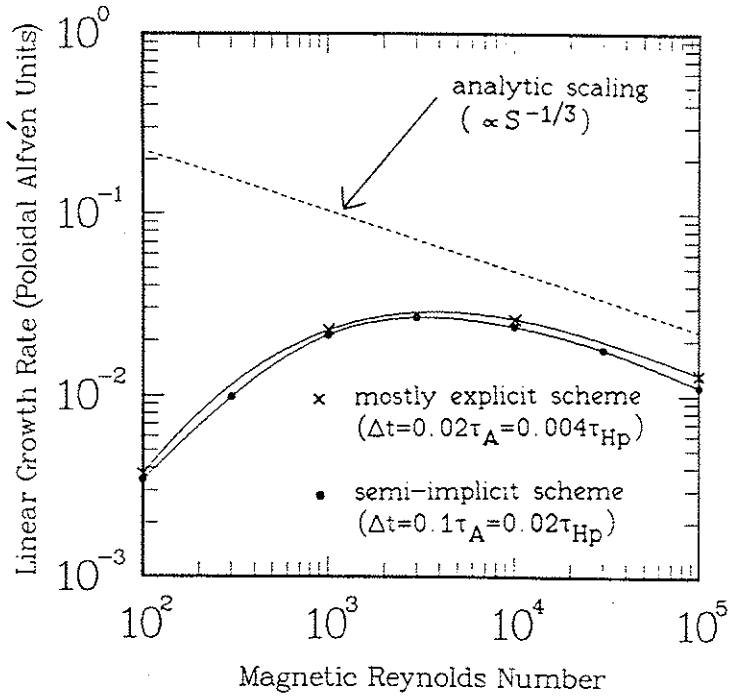

Fig. 4-27. Scalings of the linear growth rate of the n=1 component (m=1, n=1 resistive kink mode dominant) with plasma resistivity. Numerical results of RPD are compared with the standard analytic scaling. Equil. #6 is used.

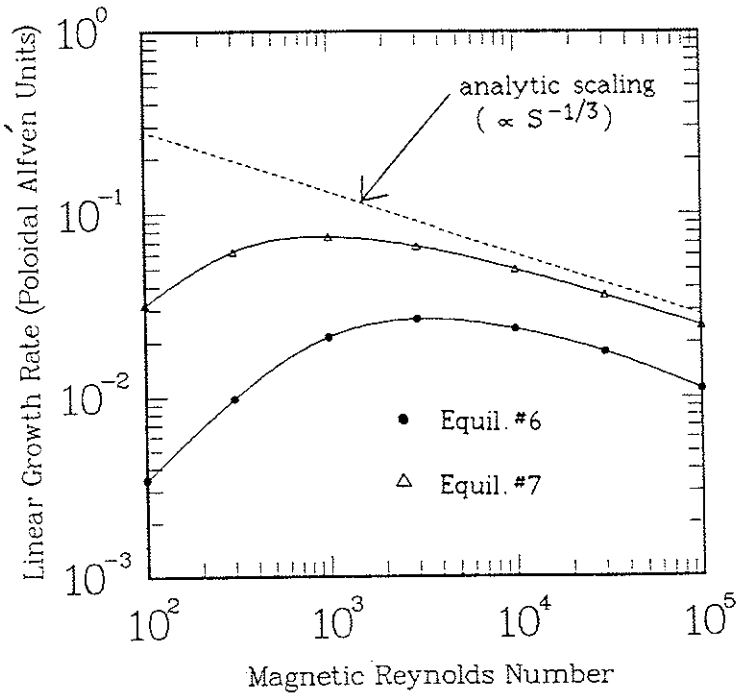

Fig. 4-28. Effect of equilibrium profiles on the resistivity scaling of the linear growth rate of the n=1 component (m=1, n=1 resistive kink mode dominant). RPD results for Equil. #6 and #7 are compared against the standard analytic scaling.

wide range of plasma resistivity. Although the semi-implicit scheme has a tendency to reduce the linear growth rate, the growth rates agree within 10 percent for $\alpha\Delta t = 0.005\ \tau_A$. Furthermore, the growth rate calculated with our RPD code scales as $S^{-1/3}$ for sufficiently high S as predicted by the analytic theory.[77] We can attribute the discrepancies between our numerical scaling and the standard analytic scaling to the way the assumption that goes into the analytic theory breaks down depending on the plasma profile. When the q=1 surface is moved further away from the region where the q and J_ζ profiles are flat, the analytic scaling works better even at smaller S. (See Fig. 4-28.)

4-3-3. Nonlinear results

It is well known that the m=1, n=1 magnetic island continues to grow well into the nonlinear regime at a rapid rate that is comparable to the linear growth rate.[14,15] In a standard tokamak plasma (e.g. $A_r \sim 5$, $S \sim 10^5$, and $\beta \sim \epsilon^2$) the m=1, n=1 magnetic island does not saturate but grows until it completely takes over the original magnetic axis. Partly because of a drastic topological change that is involved in this total reconnection process, the nonlinear simulation of the m=1, n=1 resistive kink mode usually requires a large number of toroidal Fourier components and grid points to encompass a broadened energy spectrum.

Because of the limitation on the available computer resources, however, we chose to conduct nonlinear simulations using a fairly coarse grid of 60 by 60 and including only three ($n=0, 1^+$, and 1^-) and five Fourier harmonics ($n=0, 1^+, 1^-, 2^+$, and 2^-). Both Equil.#6 and #7 are considered with a uniform S of 10^4. The new semi-implicit scheme with $\alpha=0.05$ is used for better code efficiency. Although the simulation results are not well converged, our RPD code demonstrates the total reconnection of the m=1, n=1 magnetic island in all the cases. In view of the machine and plasma parameters used, it is reasonable to assume that our results are qualitatively correct.

As examples we present the results with five Fourier harmonics. Fig.4-29 shows the temporal evolution of the n=1 and n=2 components of the magnetic energy for Equil.#6. The magnetic puncture plot at the $\zeta=0$ plane and the plot of the total J_ζ on the midplane at $\zeta=0$ are given for t=200, 250, 265, and 300 τ_{Hp} in Figs.4-30 to 4-33. Fig.4-34 shows the temporal evolution of the n=1 and n=2 components of the magnetic energy for Equil.#7. Figs.4-35 and 4-36 show the magnetic puncture plot and J_ζ plot on the midplane both at $\zeta=0$ for t=190 and 250 τ_{Hp}. In both cases the q value rises above unity everywhere upon total reconnection.

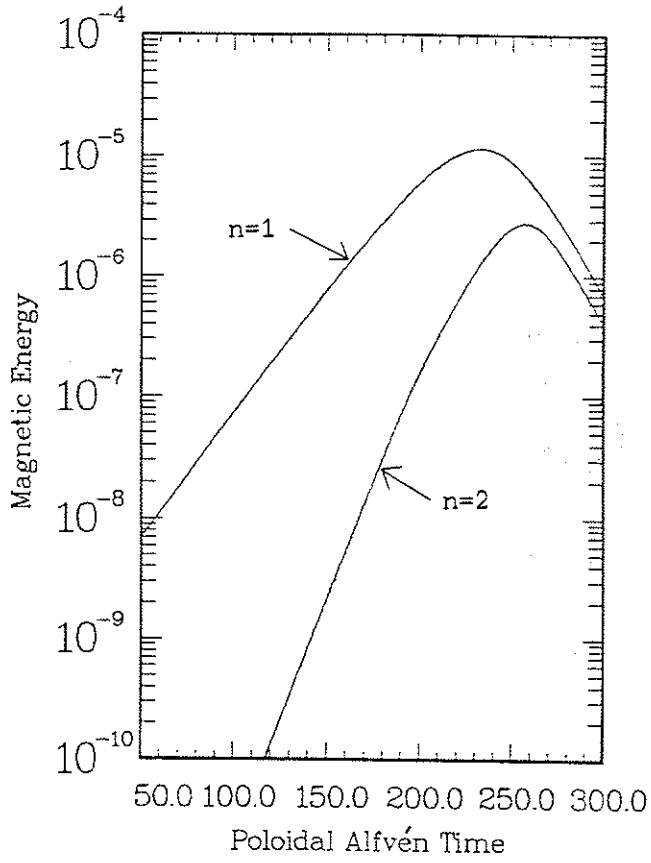

Fig.4-29. Temporal evolution of the n=1 and 2 components (m=1, n=1 resistive kink mode dominant) of the magnetic energy for Equil.#6. Five Fourier harmonics are included in this run. The magnetic energy is measured in units of $a^3(B_\zeta)^2/2\mu_o$.

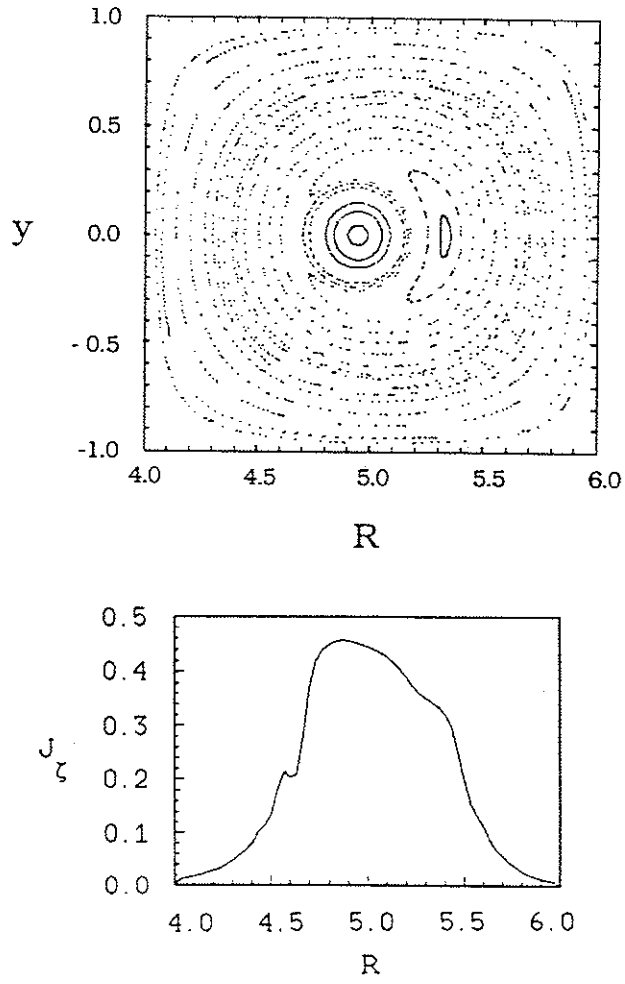

Fig. 4-30. Puncture plot of the magnetic field and the total J_ζ on the midplane both at ζ=0 for t=200τ_{Hp} with Equil. #6. In addition to a large m=1, n=1 magnetic island, a small m=2, n=1 magnetic island is present.

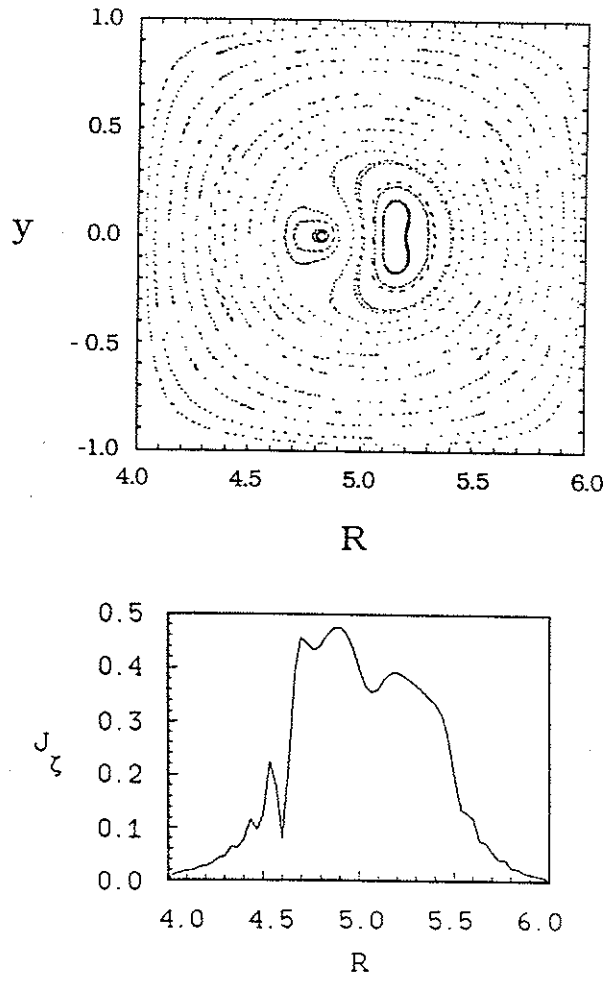

Fig. 4-31. Puncture plot of the magnetic field and the total J_ζ on the midplane both at ζ=0 for t=250τ_{Hp}. The width of the m=1, n=1 magnetic island continues to increase.

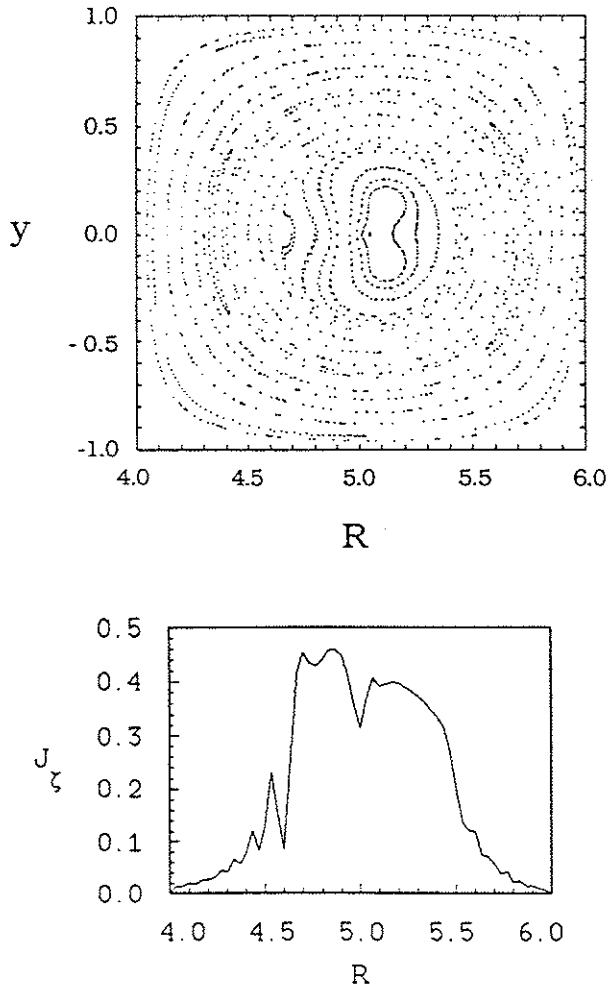

Fig. 4-32. Puncture plot of the magnetic field and the total J_ζ on the midplane both at ζ=0 for t=265τ_{Hp}. The original magnetic axis is about to be taken over by the ever growing m=1, n=1 magnetic island.

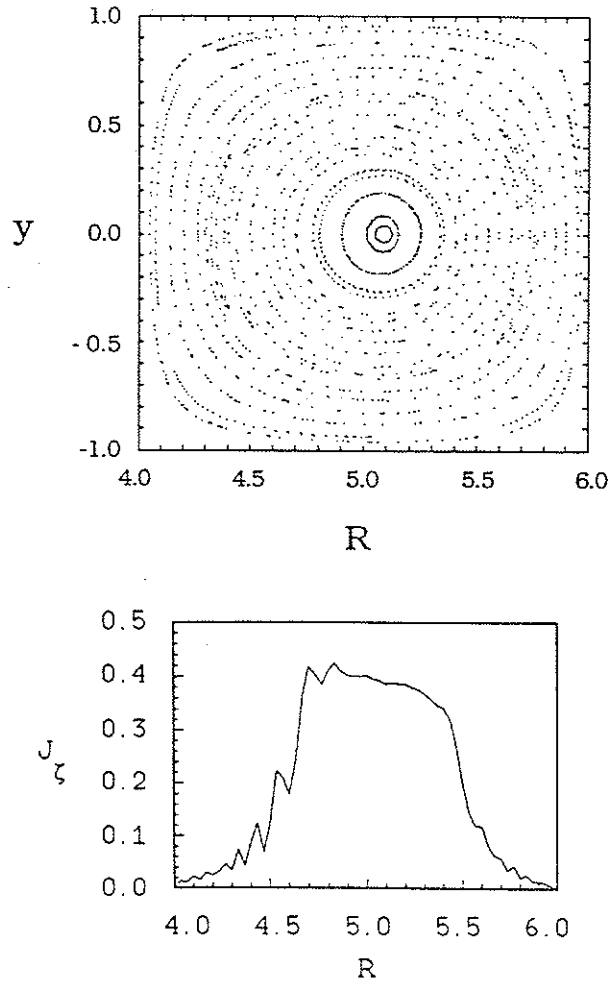

Fig. 4-33. Puncture plot of the magnetic field and the total J_ζ on the midplane both at ζ=0 for t=300τ_{Hp}. Total reconnection has taken place.

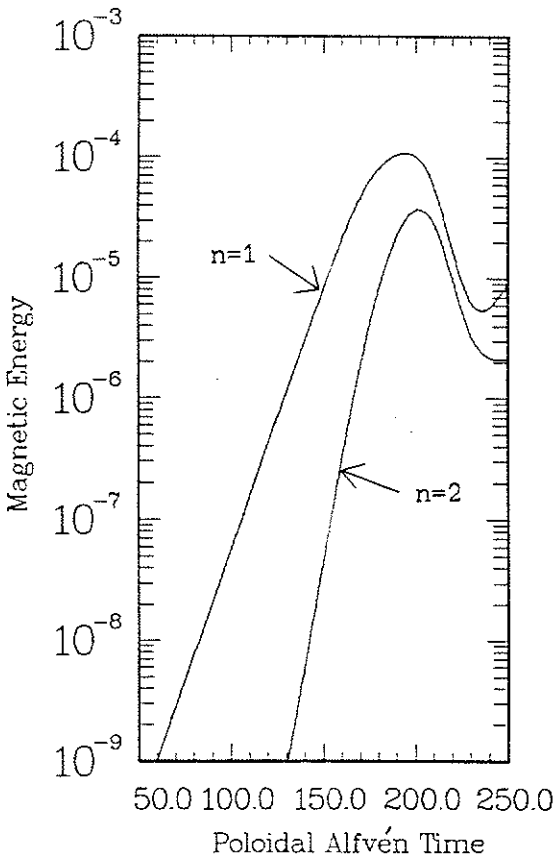

Fig.4-34. Temporal evolution of the n=1 and 2 components (m=1,n=1 resistive kink mode dominant) of the magnetic energy for Equil.#7. Five Fourier harmonics are included in this run. The magnetic energy is measured in units of $a^3(B_\zeta)^2/2\mu_o$.

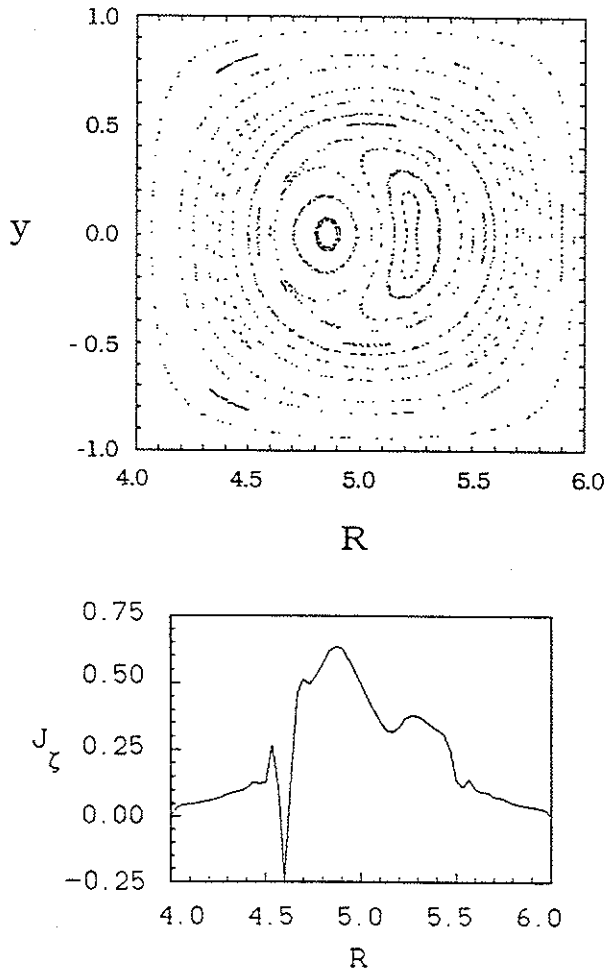

Fig.4-35. Puncture plot of the magnetic field and the total J_ζ on the midplane both at ζ=0 for t=190τ_{Hp}. In addition to a very large m=1,n=1 magnetic island, a small m=2,n=1 magnetic island is clearly visible.

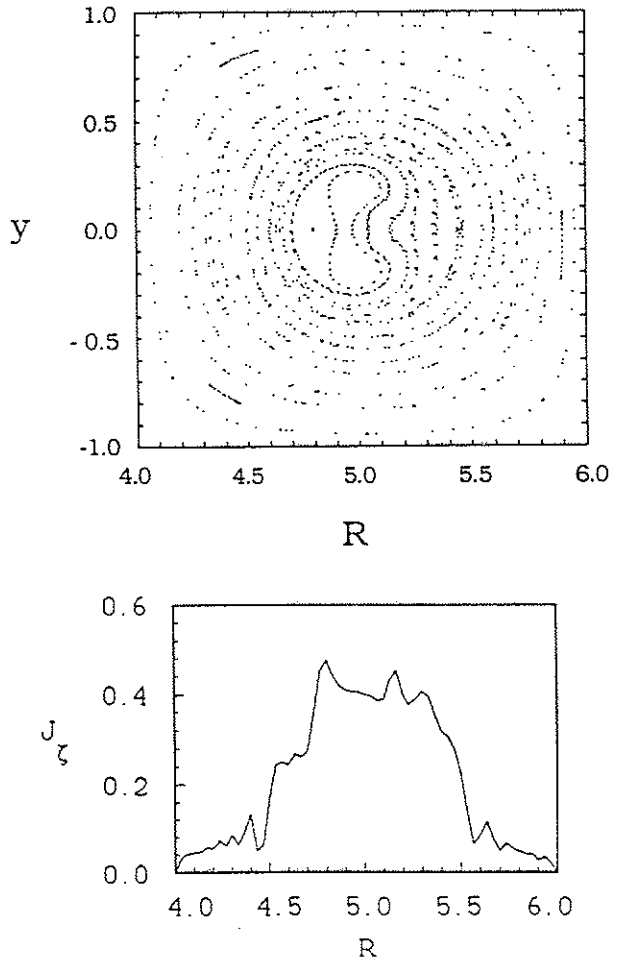

Fig.4-36. Puncture plot of the magnetic field and the total J_ζ on the midplane both at ζ=0 for t=250τ_{Hp}. Total reconnection has taken place. The oscillations in J_ζ are primarily due to a lack of grid resolution.

Chapter 5. RESISTIVE MHD INSTABILITIES IN A POLOIDAL DIVERTOR TOKAMAK

5-1. Introduction

In the previous chapter we tested extensively our 3-D resistive MHD initial value code RPD and the new semi-implicit scheme in a square cross-section tokamak without a poloidal divertor. RPD has passed our extensive numerical tests both linearly and nonlinearly, and the new semi-implicit scheme was shown to be a very efficient, yet quite accurate, numerical method for a 1-D spectral, 2-D finite difference resistive MHD initial value code.

In this chapter we test and utilize the full capability of our RPD code by including a poloidal divertor in the computational domain. Although poloidal divertor tokamaks may assume different magnetic topologies depending on the number of divertor rings, the shape of the wall, and many other factors, we shall focus on a four-node poloidal divertor tokamak with a square cross section. There are two reasons for this. First and most important, our research is intended to provide, within the realm of resistive MHD theory, a theoretical explanation of unusual features observed in the Wisconsin Tokapole II discharges.[23-30] (See also Fig.1-4.) Second, it is far beyond the scope of this thesis to investigate all the imaginable poloidal divertor configurations.

To conduct a large number of linear and nonlinear calculations, we heavily rely on the new semi-implicit scheme. Despite the simplified semi-implicit operator that assumes a standard tokamak ordering, the maximum temporal step size for numerical stability is shown to increase by a factor of somewhat less than the aspect ratio. Results with the semi-implicit schemes are compared to those with the mostly explicit scheme in selected cases to justify its use.

In sections 5-2 and 5-3 we present the simulation results for the cases in which either the m=2, n=1 tearing mode is dominant or the m=1, n=1 resistive kink mode is dominant. Each section consists of three parts: description of MHD equilibrium inputs, linear results and nonlinear results. Our studies include investigation into the effect of the proximity of the mode rational surface to the poloidal divertor separatrix and the effect of the plasma current outside the divertor separatrix on their linear and/or nonlinear evolution. In section 5-4 we compare our results with the key features of the Tokapole discharges.

5-2. m=2, n=1 Tearing Mode Dominant Case

5-2-1. MHD equilibria

About 30 MHD equilibria with $1 < q_{axis} < 2$ were generated for a poloidal divertor tokamak with an aspect ratio ($\equiv R_o/a$) of five. (a is not the distance between the magnetic

axis and the divertor separatrix but one half the size of the square wall.) The aspect ratio was chosen to be about twice as large as that of the Tokapole II to lessen the toroidal effects. In all the equilibria four divertor rings are placed at the same distance (=0.23a) away from the four corners of the square wall, respectively. In addition, each ring is positioned an equal distance (=0.16a) away from the nearby horizontal and vertical wall boundaries. In this section we show five of them (Equil.#8-#12) as examples. (See Figs.5-1 to 5-5.) All of them are essentially force free with a plasma beta of less than 0.01 percent.

Equilibria with and without the plasma current outside the divertor separatrix are considered. Equil.#9 is obtained by removing the plasma current from the common flux region of Equil.#8 while trying to keep unchanged the J_ζ and q profiles inside the divertor separatrix. Because of the limitations of our equilibrium code EQPD, we are able to keep the profiles unchanged only up to about half the distance between the q=2 surface and the divertor separatrix. Some J_ζ is scraped off from the region inside but near the divertor separatrix. As a result, the divertor separatrix moves in by about 0.05a.

Equil.#10 and #11 again constitute a pair of equilibria with and without the plasma current outside the divertor separatrix. A distinguishing feature of this pair is that the J_ζ profile is tailored so as to keep the positions of the q=2 surface and the

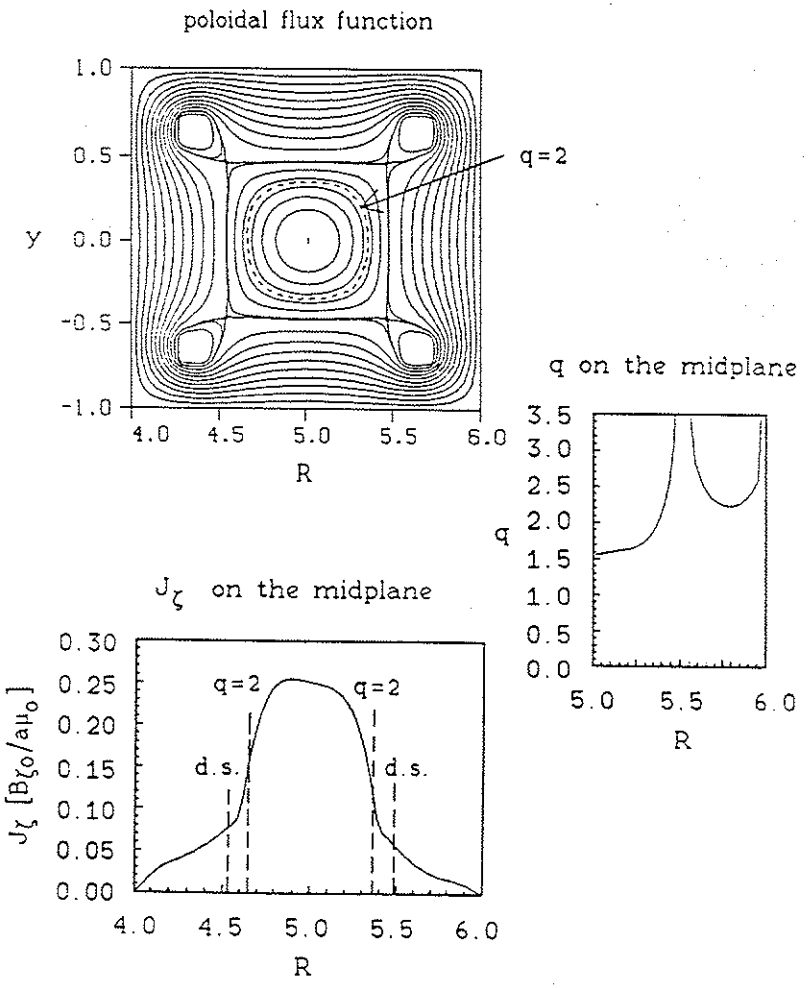

Fig.5-1. Contour plot of ψ and the plots of J_ζ and q on the midplane for Equil.#8. q on the magnetic axis is 1.56. Plasma current is included in the common flux region outside the divertor separatrix which is indicated by d.s.

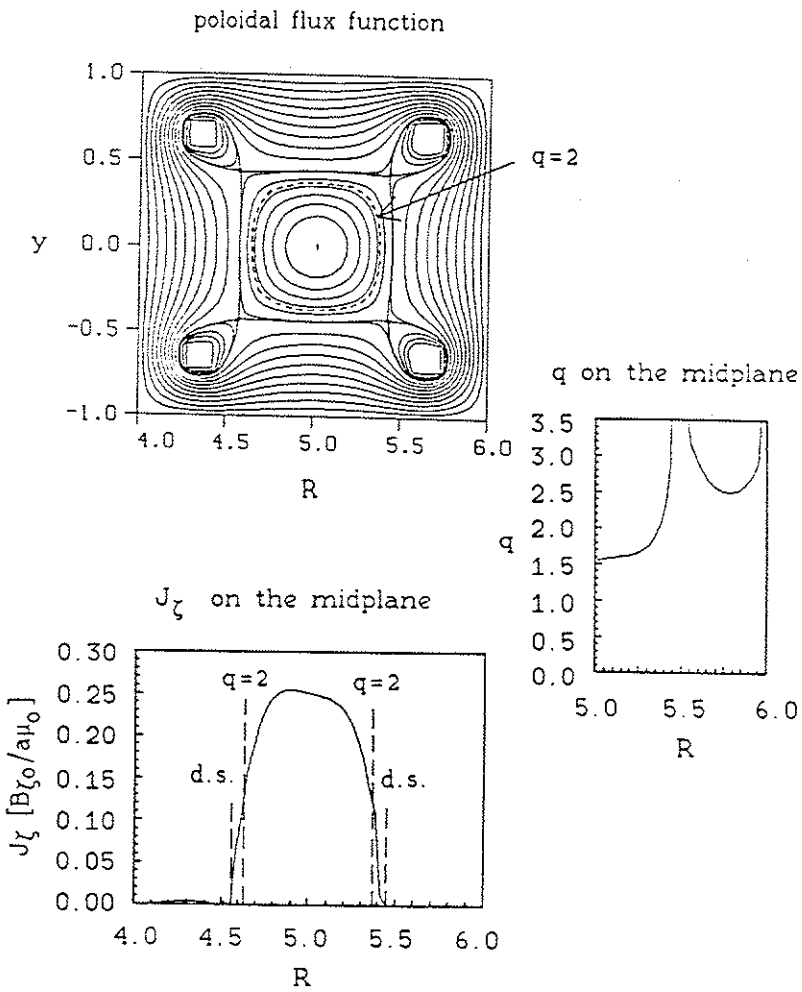

Fig.5-2. Contour plot of ψ and the plots of J_ζ and q on the midplane for Equil.#9. Plasma current in the common flux region is removed from Equil.#8 while the J_ζ and q profiles inside the divertor separatrix are kept almost unchanged.

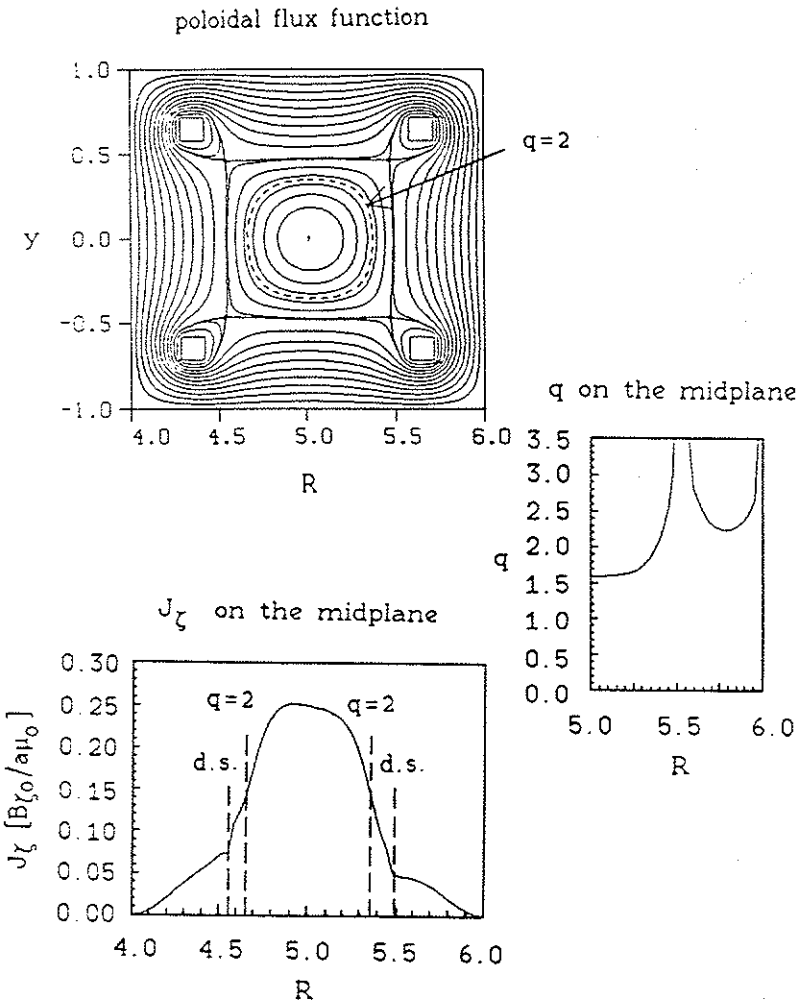

Fig. 5-3. Contour plot of ψ and the plots of J_ζ and q on the midplane for Equil. #10. q on the magnetic axis is 1.59. Plasma current is included in the common flux region.

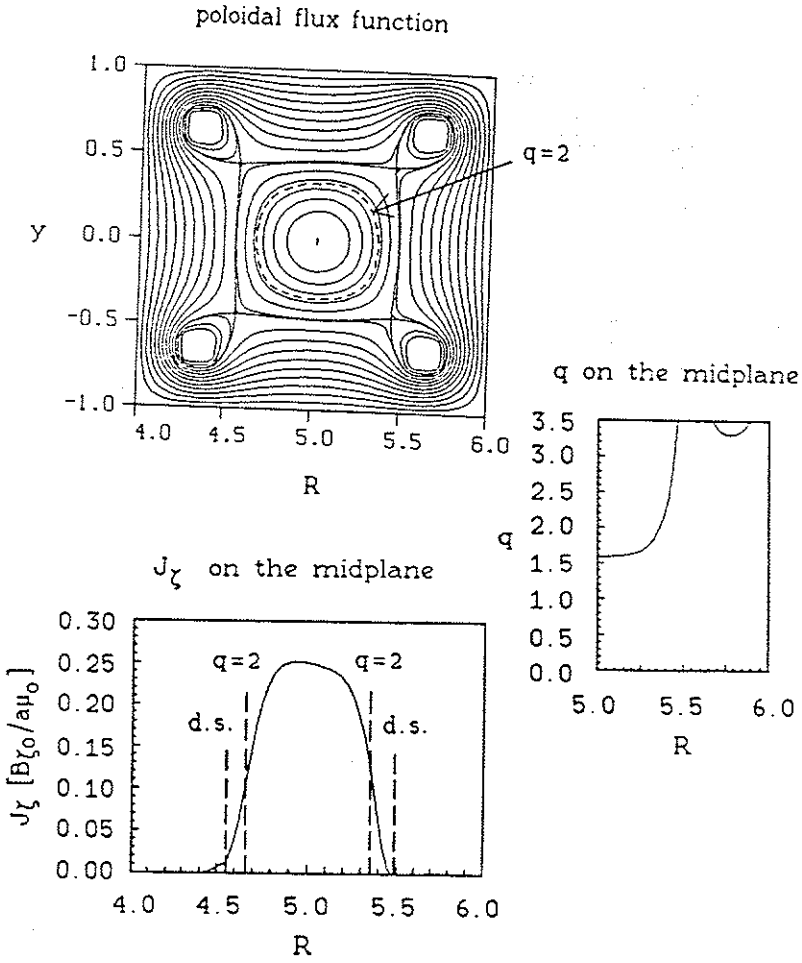

Fig. 5-4. Contour plot of ψ and the plots of J_ζ and q on the midplane for Equil. #11. Plasma current in the common flux region is removed from Equil. #10 while the positions of the q=2 surface and the divertor separatrix are kept almost unchanged.

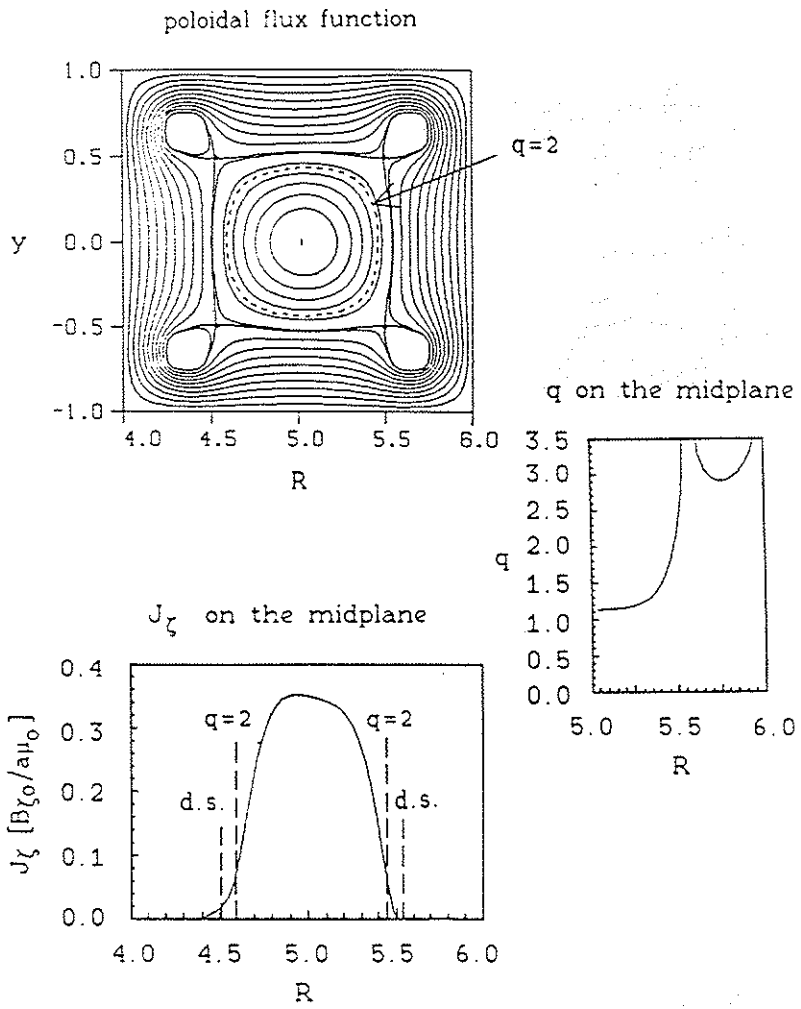

Fig.5-5. Contour plot of ψ and the plots of J_ζ and q on the midplane for Equil.#12. q on the magnetic axis is 1.13. Plasma current is removed from the common flux region.

divertor separatrix unchanged. In addition, J_ζ goes to zero more smoothly in Equil.#11 than in Equil.#9 and it is probably closer to an experimental profile when the plasma current is scraped off from the common flux region. It should be pointed out that a small amount of plasma current diffused out of the divertor separatrix in Equil.#11 as a result of a small but finite resistivity term in the EQPD code.

Equil.#12 is an equilibrium with about 40 percent more plasma current than other four equilibria. As a result, the divertor separatrix is pushed further out. This case is included here because it and Equil.#8 are used in the nonlinear simulations of the m=2, n=1 tearing mode.

5-2-2. Linear results

As in the case of a divertorless tokamak, we keep only the n=0, 1^+, and 1^- components (superscripts $^+$ and $^-$ refer to Fourier cosine and sine terms) and advance the linear terms of only the n=1^+ and 1^- components. All the helical modes with $|m| \geq 2$ and n=1 are included because of our spatial representation that is spectral only in the toroidal direction. The high m cutoff depends on the number of grid points used in the calculation. Partly because of a very limited flux space between the q=2 surface and the divertor separatrix, magnetic islands with $m \geq 3$ are difficult to identify. The m=2, n=1 tearing mode is found to invariably dominate the linear

evolution of the n=1 component.

Equil.#8 is used extensively to compare the semi-implicit and the mostly explicit schemes as applied to the divertor geometry. The eigenfunctions obtained with the two schemes are found to be in very good agreement despite the fact that the semi-implicit term enables us to use a temporal step size Δt that is larger than a mostly explicit run by a factor somewhat less than the aspect ratio. As an example, plots of the perturbed J_ζ on the midplane at $\zeta=0$ that are calculated with the two schemes are compared in Fig.5-6. A temporal step size Δt of $0.05\tau_A$ $(=0.01\tau_{Hp})$ is used for the semi-implicit scheme and Δt of $0.0125\tau_A$ $(=0.0025\tau_{Hp})$ is used for the mostly explicit scheme. The semi-implicit coefficient α is chosen to be 0.05. The grid size is 100 by 100 and the magnetic Reynolds number is taken to be 10^4.

As for the eigenvalue, the semi-implicit scheme has a tendency to reduce the linear growth rate of the n=1 component as the temporal step size Δt is increased. Fig.5-7 shows the effect of the temporal step size Δt on the linear evolution of the n=1 component. Results with the semi-implicit scheme for $\alpha=0.05$ are compared with those with the mostly explicit scheme. At a very modest expense in accuracy the maximum step size for numerical stability is increased by a factor somewhat less than the aspect ratio of five. Equil.#8 with the grid size of 60 by 60 is used in this survey.

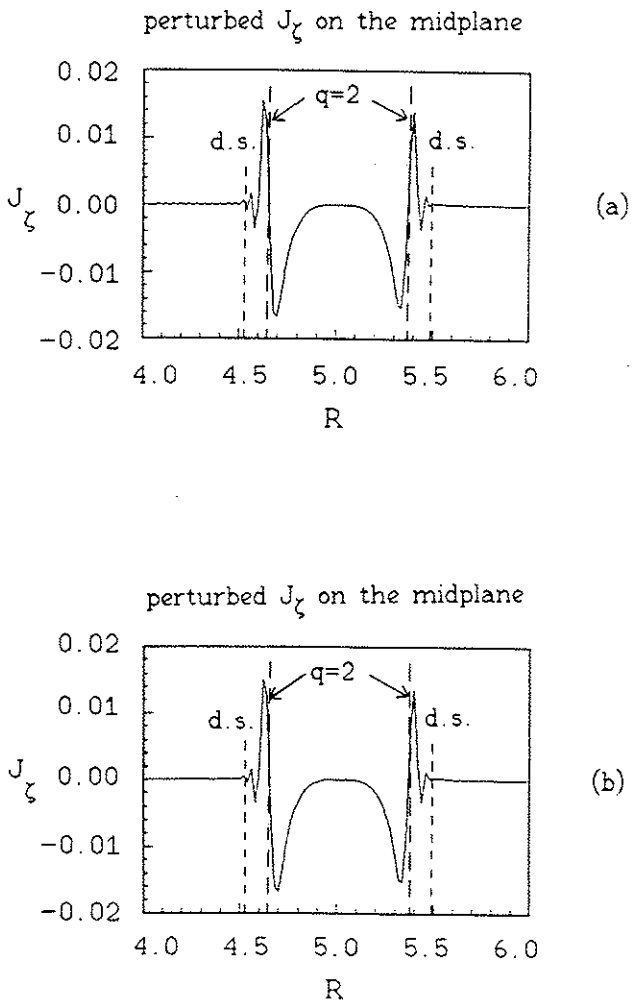

Fig.5-6. Plots of perturbed J_ζ on the midplane for Equil.#8 calculated with (a) the mostly explicit scheme and (b) the new semi-implicit scheme.

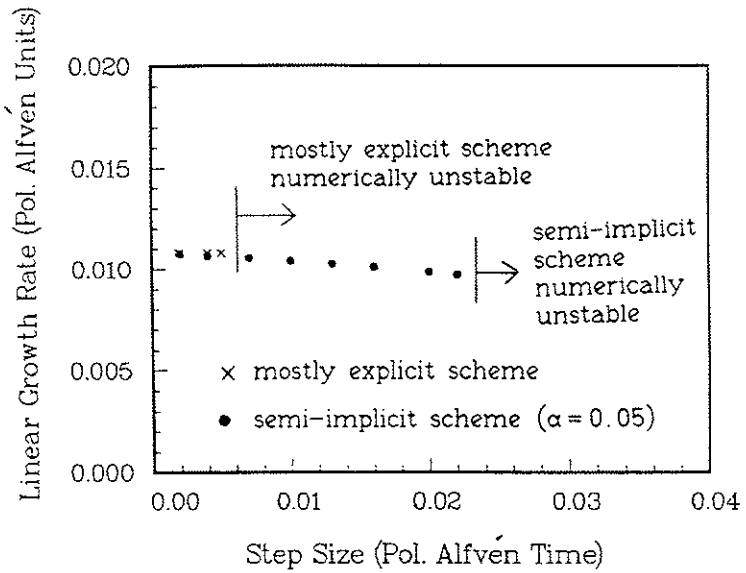

Fig.5-7. Effect of temporal step size on the linear growth rate of the n=1 component (m=2,n=1 tearing mode dominant) for Equil.#8. Results with the mostly explicit and the semi-implicit schemes are compared.

In the case of a divertorless geometry the maximum step size for numerical stability was found to be almost independent of the grid size. Unfortunately, it is not so in the case of a poloidal divertor geometry. The maximum step size for numerical stability decreases linearly with the grid spacing. This step size restriction is probably due to the Alfven waves that propagate toroidally near the divertor rings. Such waves are significant in the regions where $B_\zeta \sim B_{poloidal}$, and the step size restriction imposed by them is apparently not eliminated by

our simplified semi-implicit term. However, it is noteworthy that our semi-implicit term does improve the code efficiency (i.e., the computer time required to reach the same physical time) by almost a factor of the aspect ratio for all grid sizes.

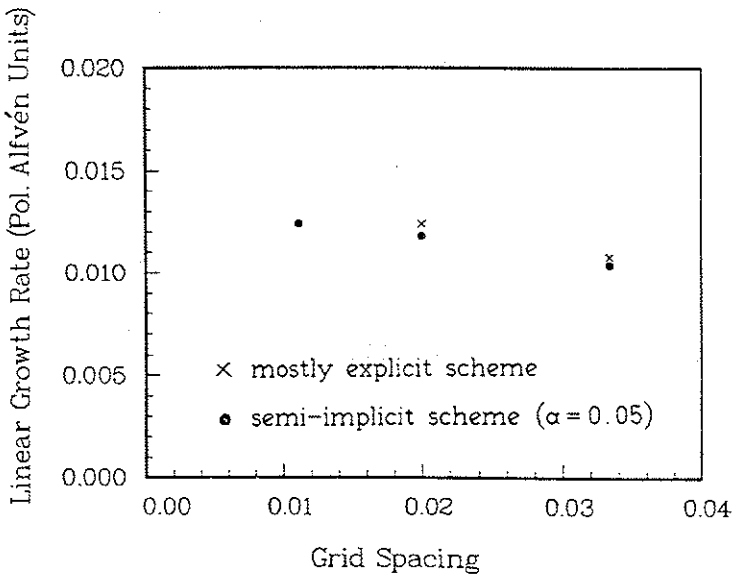

Fig.5-8. Effect of grid spacing (or reciprocal of one half the grid size) on the linear growth rate of the n=1 component (m=2,n=1 tearing mode dominant) for Equil.#8. Results with the mostly explicit and the semi-implicit schemes are compared.

Fig.5-8 shows the grid convergence of the linear growth rate of the n=1 component for Equil.#8. The grid sizes used are 60 by 60, 100 by 100, and 180 by 180 for the semi-

implicit scheme and 60 by 60 and 100 by 100 for the mostly explicit scheme. Although the number of data points is limited, we conclude that the grid convergence is satisfactory in view of our experience with the divertorless geometry. (See Fig.4-11.)

Next we examine the effect of the plasma current outside the divertor separatrix on the linear evolution of the n=1 component. To this end, we use Equil.#8 and #9 both with a grid size of 100 by 100. S is assumed to be 10^4 everywhere and the semi-implicit scheme is adopted for better code efficiency. (Even so, each run requires about 90 minutes of computer time for a well converged solution.) The gross features of the eigenfunction structures are similar; the MHD activity is mostly contained in the region near the q=2 surface and inside the divertor separatrix. However, some minor differences are found. For example, the perturbed J_ζ for Equil.#9 exhibits more asymmetry about the magnetic axis of the equilibrium than that for Equil.#8 does. (See Fig.5-9.) In addition, the perturbed J_ζ for Equil.#9 contains more fine scale features near the divertor separatrix. Fig.5-10 compares the kinematics of the instability for the two cases. The divertor separatrix of the equilibrium is superposed on each plot.

The linear growth rates of the n=1 component are found to be 1.2×10^{-2} $[1/\tau_{HP}]$ for Equil.#8 and 8.7×10^{-3} $[1/\tau_{Hp}]$ for Equil.#9. This may appear rather surprising because the

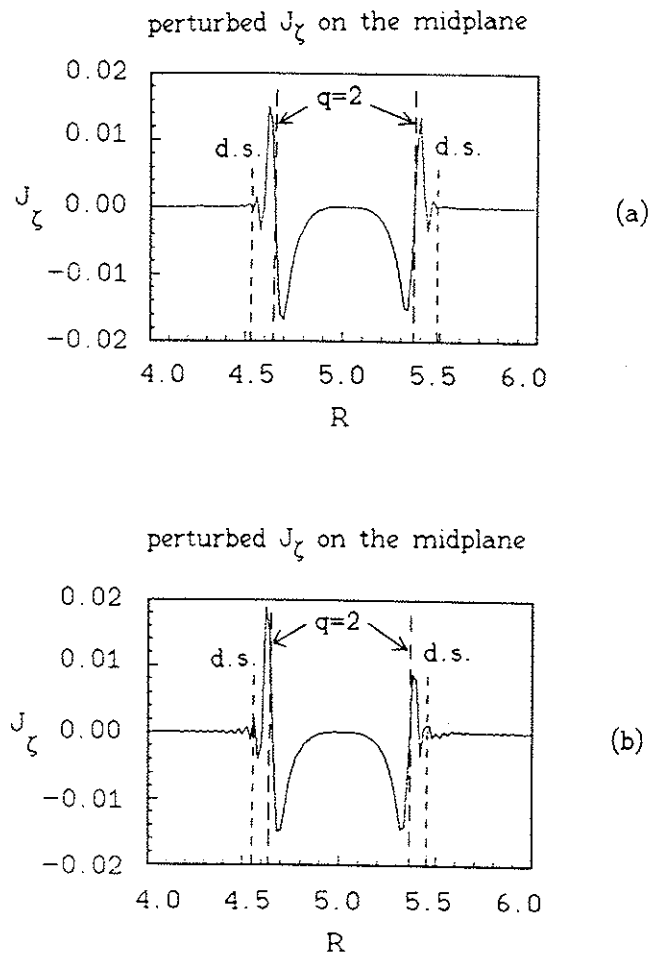

Fig.5-9. Perturbed J_ζ of the n=1 component for (a) Equil.#8 (with plasma current in the common flux region) and (b) Equil.#9 (no plasma current in the common flux region).

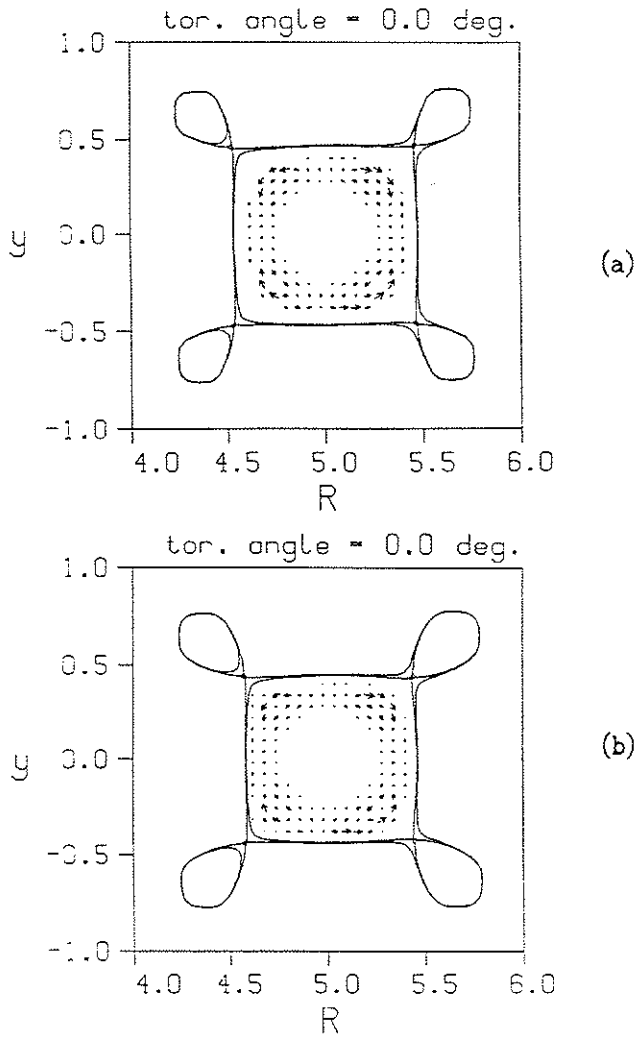

Fig.5-10. Plasma flow patterns of the n=1 component for (a) Equil.#8 (with plasma current in the common flux region) and (b) Equil.#9 (no plasma current in the common flux region).

plasma current in the wings usually stabilizes the m=2,n=1 tearing mode in a divertorless tokamak. However, we can at least partially attribute this discrepancy to the noncircularity effect. Because the q=2 surface is closer to the divertor separatrix in Equil.#8, the stabilizing effect due to noncicularity[70] is stronger. (This stabilizing effect has also been confirmed by our RPD code in a divertorless geometry by placing the q=2 surface near the square wall.) In support of this explanation, we find that the fractional difference in the linear growth rates is smaller for a pair of equilibria with the q=2 surface further away from the divertor separatrix.

To gain some insight into the linear instability of the m=2,n=1 tearing mode in a real experiment, we study a family of equilibrium pairs with more realistic J_ζ profiles as in Equil.#10 and #11. The q value on the magnetic axis is changed from 1.89 to 1.15, and thereby the distance between the q=2 surface and the divertor separatrix is changed from 0.26a to 0.08a. The result of this parameter survey is shown in Fig.5-11.

The case with q_{axis}=1.89 is found to be stable with a negative growth rate. As the q=2 surface is moved away from the central region where the J_ζ gradient is small, the m=2,n=1 tearing mode becomes unstable and the linear growth rate of the n=1 component increases. An equilibrium with no plasma current outside the divertor separatrix invariably yields

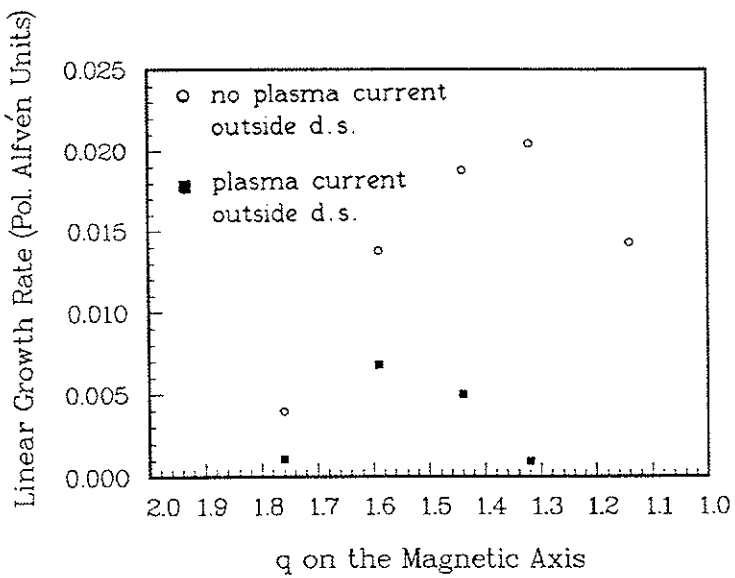

Fig.5-11. Effects of plasma current in the common flux region and the value of q_{axis} on the linear growth rate of the n=1 component (m=2,n=1 tearing mode dominant). As q_{axis} decreases, the q=2 surface moves closer to the divertor separatrix.

a larger linear growth rate than its counterpart with plasma current outside. This is in contrast to the result with the earlier equilibrium pair (Equil.#8 and #9) and suggests the importance of the profile effect. The mode is stabilized again when the q=2 surface is brought too close to the divertor separatrix regardless of whether or not there is plasma current in the common flux region. For this parameter survey a fairly coarse grid of 60 by 60 was used and S was assumed to

be 10^4 everywhere. The results were later confirmed by using a finer grid of 100 by 100 for selected cases.

From our studies it is reasonable to conclude that the mere presence of the plasma current in the common flux region is not important for the linear stability of the m=2,n=1 tearing mode. What is more important is the way the plasma current in the common flux region affects the J_ζ and q profiles in the vicinity of the q=2 surface and the divertor separatrix.

5-2-3. Nonlinear results

When magnetic islands grow sufficiently wide in a divertor tokamak, they can interact with the divertor separatrix to alter the tearing mode evolution from that in a divertorless tokamak. Investigation of such an effect requires nonlinear simulations. As discussed in section 4-2-3, a well converged nonlinear simulation all the way to the onset of a major disruption is extremely difficult and demanding. It is reasonable to anticipate that a divertor geometry would require substantially more grid points and toroidal Fourier harmonics to achieve convergence. Such a nonlinear run would require hundreds, even thousands, of hours of computer time per run even with the help of the semi-implicit scheme and it is far beyond the scope of this thesis. Instead of attempting such a run, we are content to test the nonlinear option of our RPD code for cases in which a major disruption is not likely to take place.

Fig.5-12 on page 156 summarizes the results of three nonlinear runs for Equil.#8. With q_{axis}=1.56 this equilibrium has the advantage of excluding the q=1.5 surface. S is taken to be 10^4 everywhere. In all three cases the growth of the n=1 component of the magnetic energy (m=2, n=1 mode dominant) saturates. The saturation energies agree within 25 percent. Table 5-1 shows that the magnetic and kinetic energies of the toroidal Fourier components diminish rapidly with increasing toroidal mode numbers. This justifies a truncation of the Fourier series after only a few terms. For a higher code efficiency the new semi-implicit scheme is used for all the nonlinear runs. Even so, the run with nine Fourier harmonics with a 60 by 60 grid took about seven hours of Cray 2 computer time.

	n=2/n=1	n=3/n=1	n=4/n=1
magnetic part	9.0×10^{-3}	4.1×10^{-4}	2.6×10^{-5}
kinetic part	6.7×10^{-2}	2.4×10^{-3}	4.6×10^{-4}

Table 5-1. Ratios of the energies of various Fourier components.

Fig.5-13 shows puncture plots of the magnetic field lines at ζ=0 and 180 degrees for $t=300\tau_{Hp}$ for the case with nine Fourier components. Besides the m=2, n=1 magnetic island, a

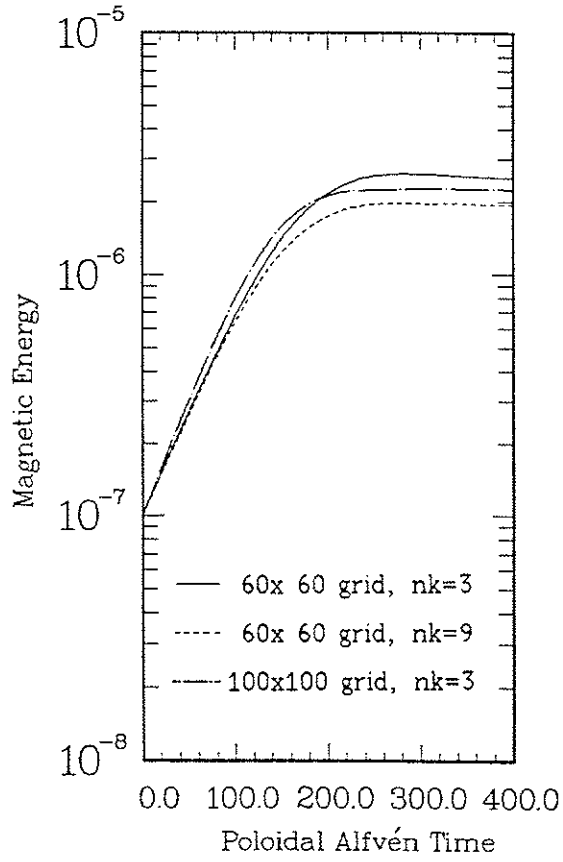

Fig.5-12. Temporal evolution of the n=1 component (m=2, n=1 tearing mode dominant) of the magnetic energy for Equil.#8 with $S=10^4$. Results of three nonlinear runs are compared. The magnetic energy is measured in units of $a^3(B_\zeta)^2/2\mu_0$. nk is the number of toroidal Fourier harmonics.

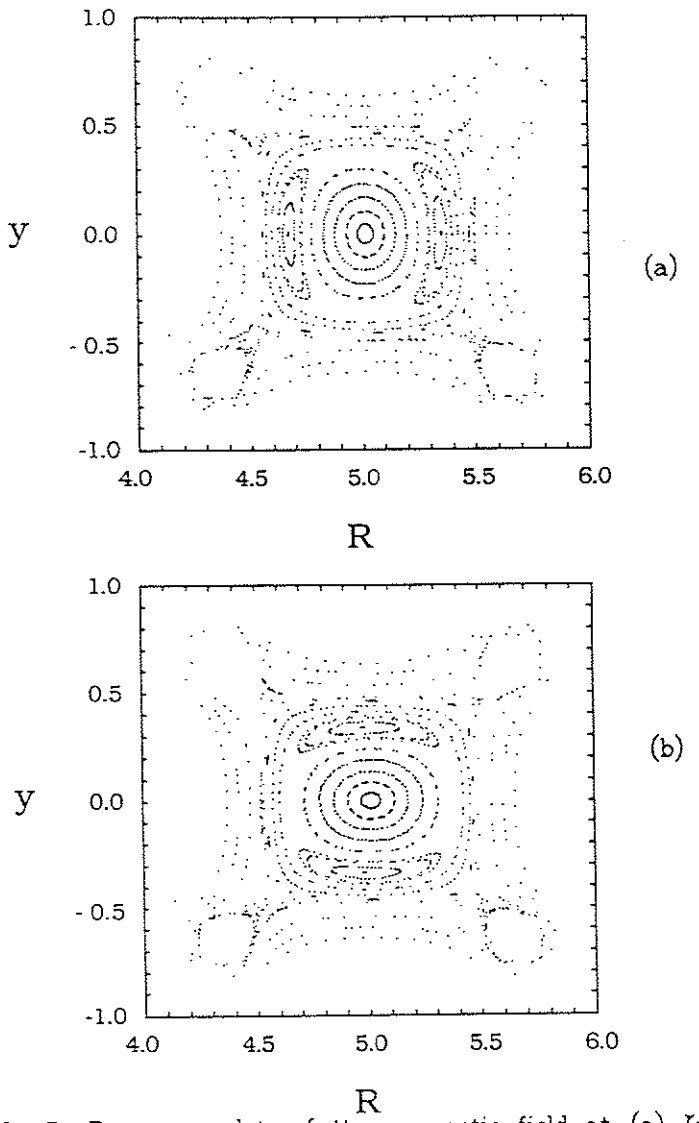

Fig. 5–13. Puncture plots of the magnetic field at (a) ζ=0 and (b) 180 degrees for t=300 τ_{Hp}.

very narrow m=3, n=1 island is identified near the divertor separatrix. (It is easier to tell this while the program is generating a plot on the screen.) The flux surfaces are found to be quite resilient. It is only in the region very near the divertor separatrix where the magnetic field becomes stochastic.

Fig. 5–14 is a plot of the total J_ζ on the midplane at ζ=0 for this run. The positions of the q=2 surface and the divertor separatrix are indicated. Small oscillations outside the divertor separatrix are numerical in origin.

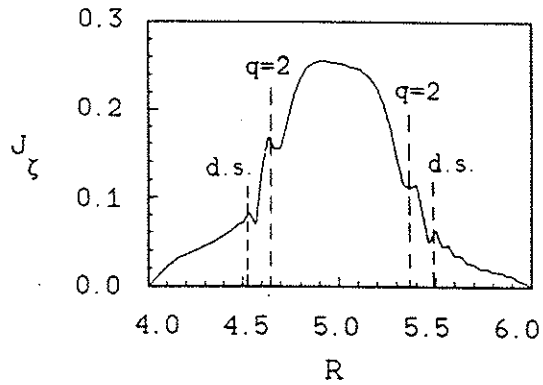

Fig. 5–14. The total J_ζ on the midplane at ζ=0 for t=300 τ_{Hp}.

To force the m=2, n=1 tearing mode to interact more strongly with the divertor separatrix, we carried out a nonlinear run with Equil. #12 in which the q=2 surface is placed closer to the divertor separatrix. To eliminate the possibility of interaction of m=2, n=1 and m=3, n=2 modes, we deliberately

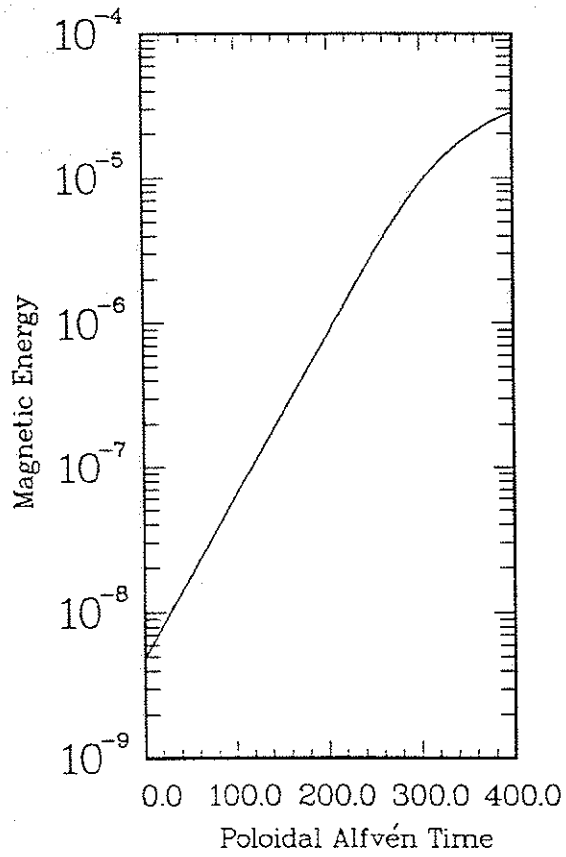

Fig. 5-15. Temporal evolution of the n=1 component (m=2, n=1 tearing mode dominant) of the magnetic energy for Equil. #12 with $S=10^4$. The magnetic energy is measured in units of $a^3(B_\zeta)^2/2\mu_0$.

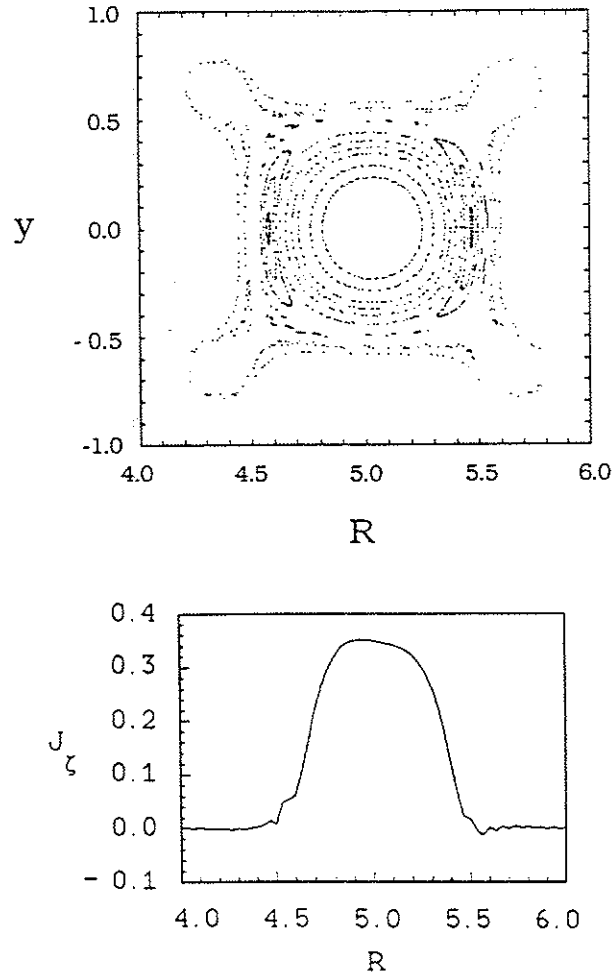

Fig. 5-16. Puncture plot of the magnetic field and the total J_ζ on the midplane both at $\zeta=0$ for $t=225\tau_{Hp}$.

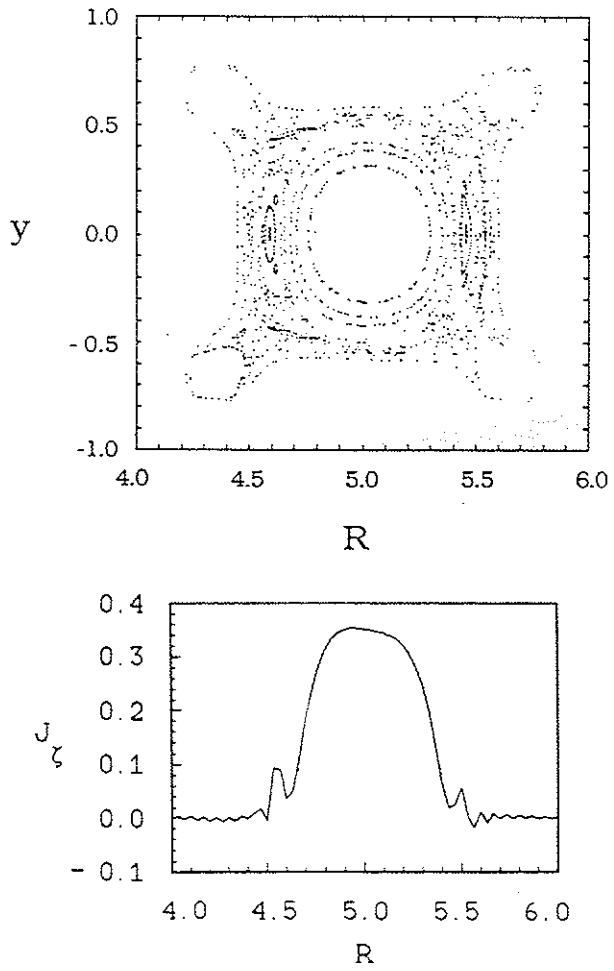

Fig.5-17. Puncture plot of the magnetic field and the total J_ζ on the midplane both at ζ=0 for t=350τ_{Hp}. The m=2,n=1 island interacts with the divertor separatrix and causes significant stochasticity of the magnetic field.

ran a case with only n=0, 1+ and 1- components. The results are shown in Figs. 5-15, 5-16, and 5-17. Before the growth of the n=1 component saturates, the m=2,n=1 magnetic island begins to overlap with the divertor separatrix. As a result, significant stochasticity develops in the region near the divertor separatrix.

5-3. m=1,n=1 Resistive Kink Mode Dominant Case

5-3-1. MHD equilibria

About 20 MHD equilibria with $q_{axis} < 1$ were generated for a poloidal divertor tokamak with an aspect ratio of five. As in equilibria with $1 < q_{axis} < 2$, four divertor rings are placed at the same distance (=0.23a) away from the four corners of the square wall. In addition, each ring is positioned an equal distance away from the nearby horizontal and vertical wall boundaries. In this section we again present five of them (Equil.#13-#17) as examples. (See Figs.5-18 to 5-22.) The plasma beta is chosen to be less than 0.01 percent in all five equilibria.

Equil.#13 and #14 are a pair of equilibria with and without plasma current outside the divertor separatrix. Equil.#14 is obtained by removing the plasma current from the region outside the divertor separatrix of Equil.#13 while not altering the J_ζ and q profiles inside the divertor separatrix. Pragmatically, the limitations of our equilibrium code EQPD

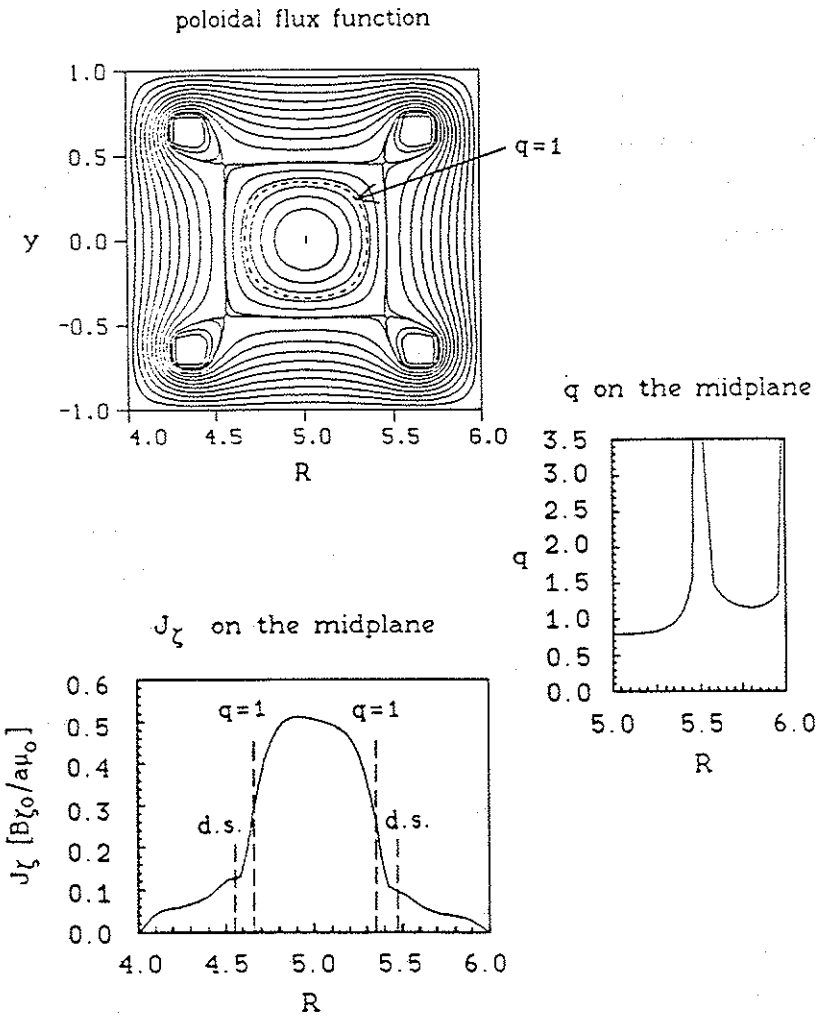

Fig.5-18. Contour plot of ψ and the plots of J_ζ and q on the midplane for Equil.#13. q on the magnetic axis is 0.79. Plasma current is included in the common flux region outside the divertor separatrix (d.s.)

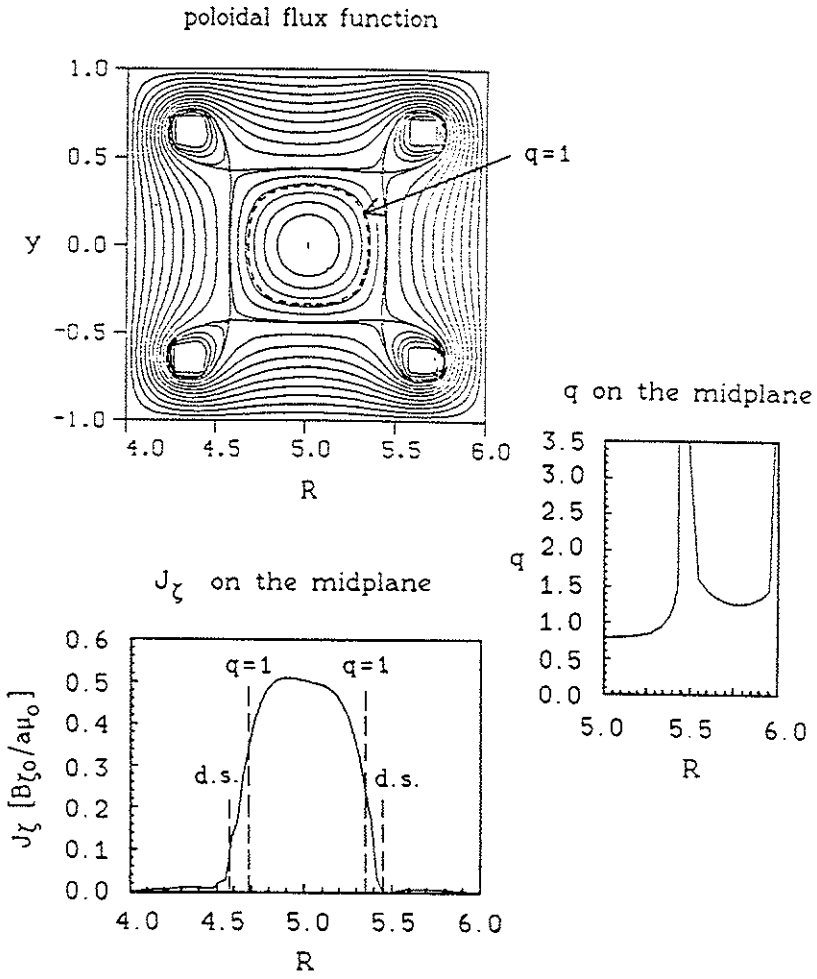

Fig.5-19. Contour plot of ψ and the plots of J_ζ and q on the midplane for Equil.#14. Plasma current in the common flux region is removed from Equil.#13 while the J_ζ and q profiles inside the divertor separatrix are kept almost unchanged.

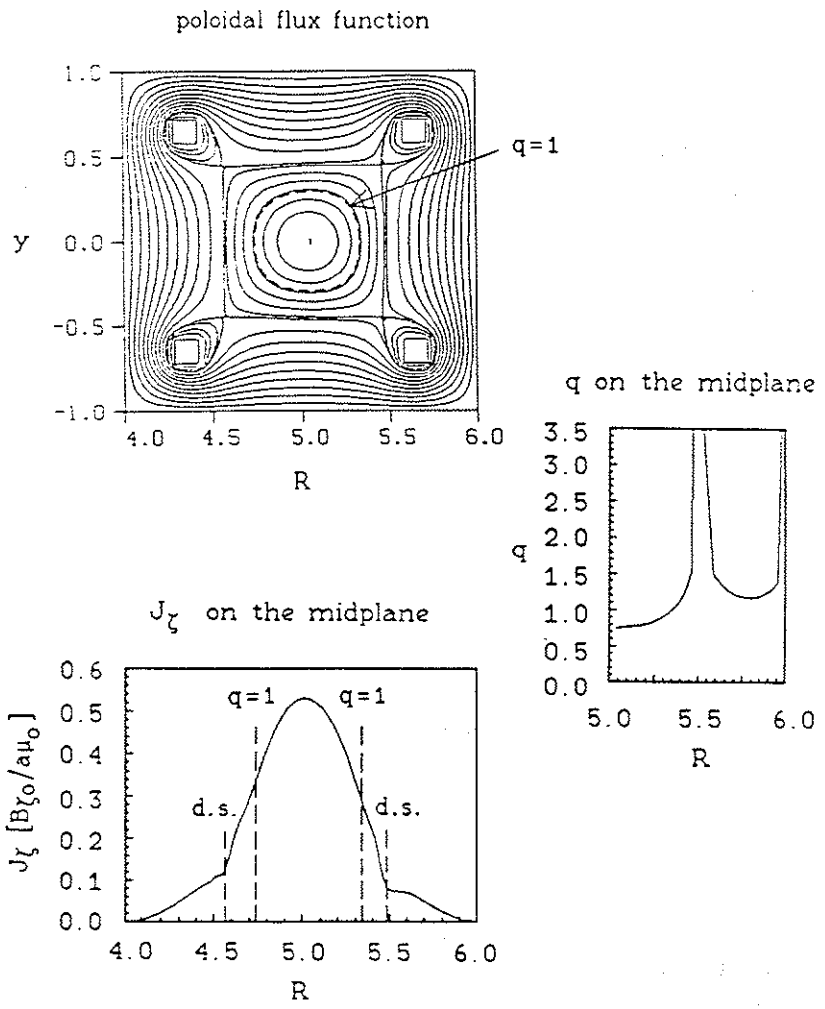

Fig. 5-20 Contour plot of ψ and the plots of J_ζ and q on the midplane for Equil. #15. q on the magnetic axis is 0.75. Plasma current is included in the common flux region.

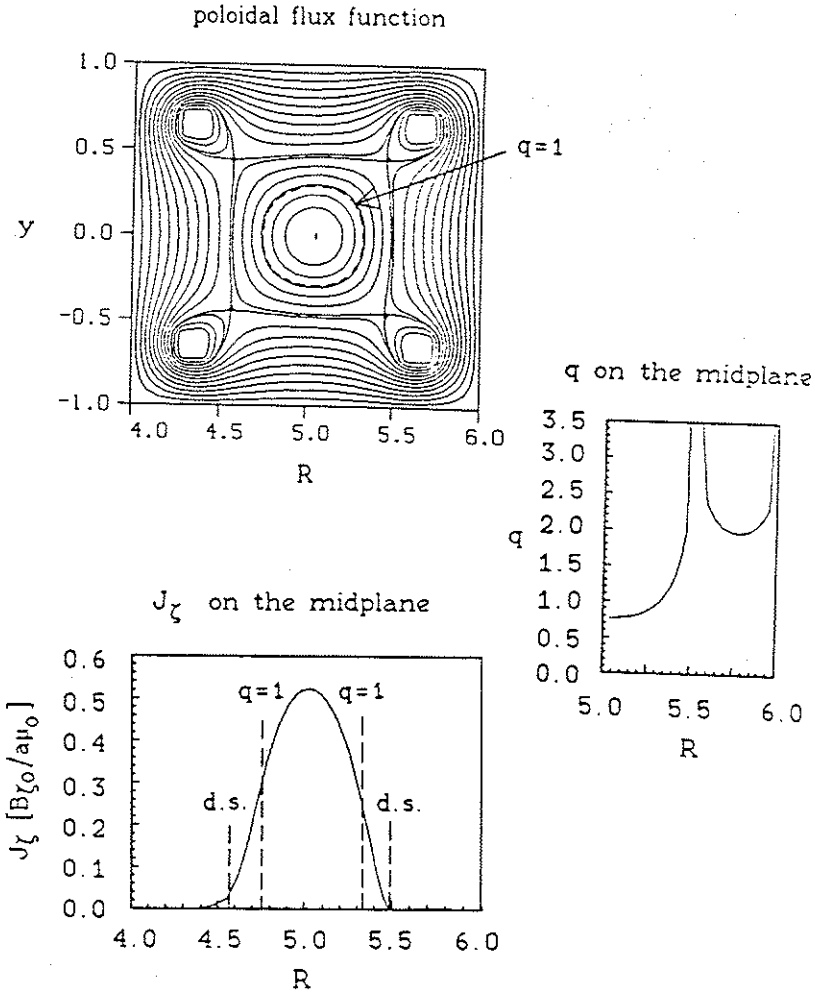

Fig. 5-21. Contour plot of ψ and the plots of J_ζ and q on the midplane for Equil. #16. Plasma current in the common flux region is removed from Equil. #15 while the positions of the q=1 surface and the divertor separatrix are kept almost unchanged.

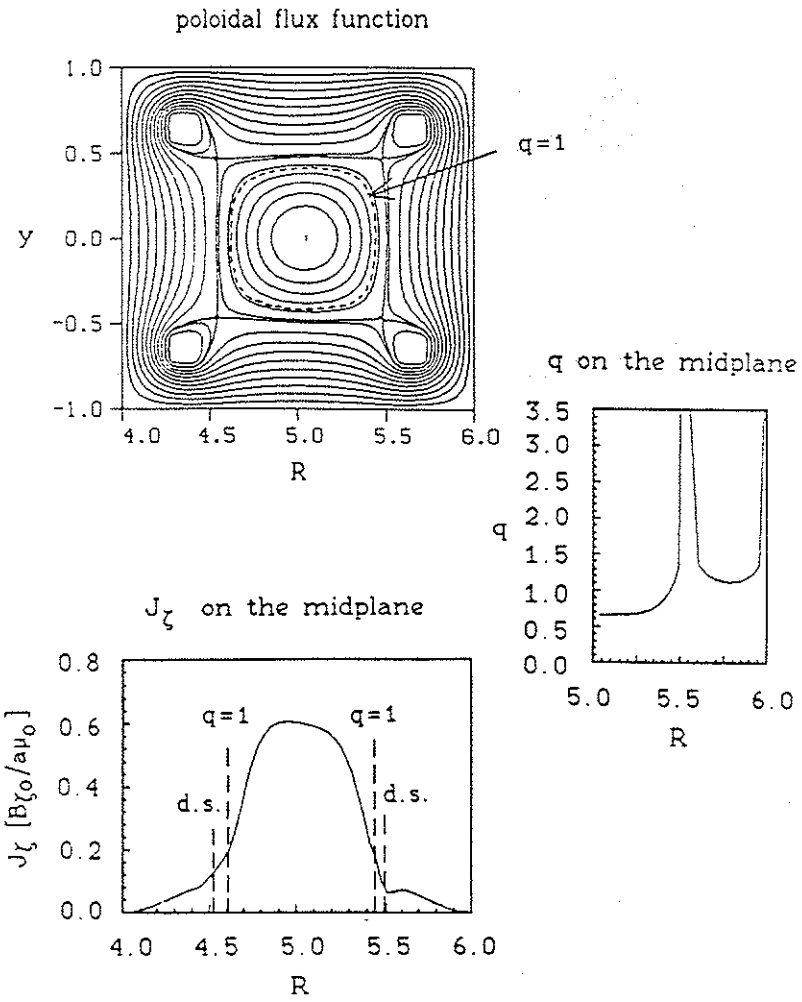

Fig.5-22. Contour plot of ψ and the plots of J_ζ and q on the midplane for Equil.#17. q on the magnetic axis is 0.65. Plasma current is included in the common flux region.

allow us to keep the profiles unchanged only up to about half the distance between the q=1 surface and the divertor separatrix. A small amount of J_ζ is scraped off from the region just inside the divertor separatrix. As a result, the divertor separatrix moves in by about 0.03a.

Equil.#15 and #16 constitute a different pair of equilibria with and without plasma current outside the divertor separatrix. Unlike Equil.#13 and #14, the J_ζ profile is tailored so as to keep the positions of the q=1 surface and the divertor separatrix unchanged. Although the J_ζ profile is more peaked than that for a low q discharge ($q_{axis} < 1$) in Tokapole II, the way J_ζ goes to zero at or near the divertor separatrix is probably more realistic than that of Equil.#13.

Equil.#17 is an equilibrium with the q=1 surface very close to the divertor separatrix. This is one of the two equilibria used in the nonlinear simulations of the m=1,n=1 resistive kink mode. (The other is Equil.#13.)

5-3-2. Linear results

Linear simulations of the n=1 component are repeated using equilibria with $q_{axis} < 1$. As in a divertorless tokamak, the m=1,n=1 resisitive kink mode is found to be dominant over all other modes with n=1.

Both the semi-implicit and the mostly explicit schemes are used for Equil.#13 with a grid size of 100 by 100. The

eigenfunctions obtained with the two schemes are again in very good agreement. (See Fig. 5-23 as an example.) The semi-implicit run with α=0.05 and Δt=0.05τ_A reduces the linear growth rate by only five percent compared with the mostly explicit run with Δt=0.0125 τ_A. This along with the results of more extensive numerical tests performed for the equilibria with $1<q_{axis}<2$ in section 5-2-2 strongly suggest a reliability and usefulness of the new semi-implicit scheme in the divertor geometry as well.

Next we examine the effect of the plasma current in the common flux region on the linear evolution of the n=1 component when the m=1, n=1 resistive kink mode is dominant. Equil. #13 and #14 both with a grid size of 100 by 100 are studied using the semi-implicit scheme with α=0.05 and Δt=0.05 τ_A. The eigenfunction structures are in very good agreement. Figs. 5-24 and 5-25 show the perturbed J_ζ on the midplane and the plasma flow patterns, all at ζ=0. The linear growth rates are found to be $4.28\times10^{-2}[1/\tau_{Hp}]$ and $4.19\times10^{-2}[1/\tau_{Hp}]$, respectively. This comparison is repeated for other equilibrium pairs including and excluding the plasma current in the common flux region while keeping the J_ζ and q profiles inside the divertor separatrix unchanged for each pair. We find the effect of the plasma current outside the divertor separatrix on the linear evolution of the m=1, n=1 resistive kink mode to be small.

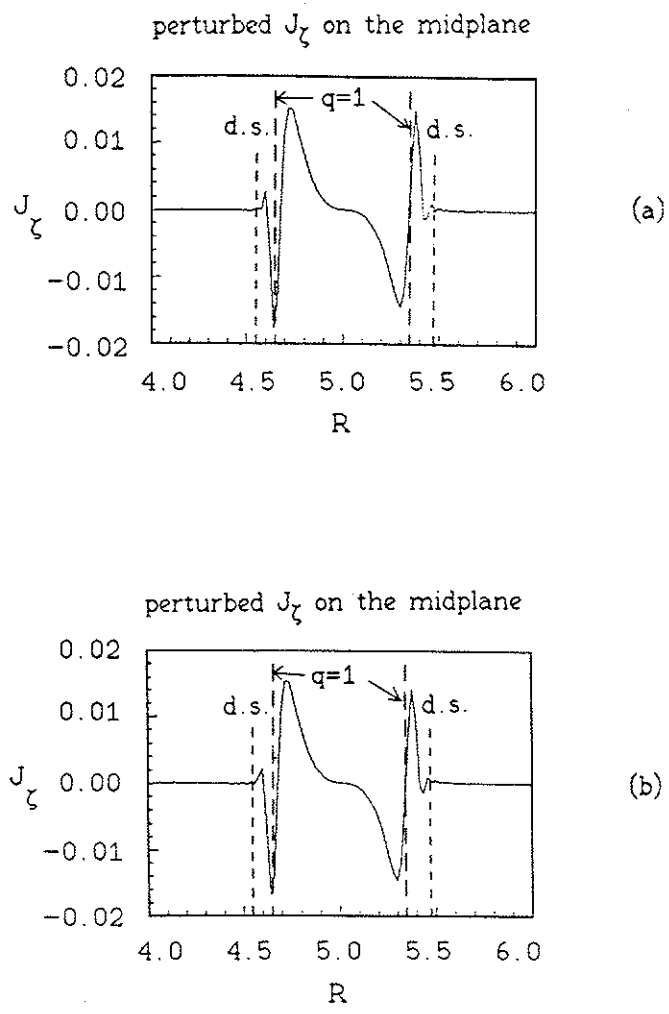

Fig. 5-23. Plots of the perturbed J_ζ on the midplane for Equil. #13 calculated with (a) the mostly explicit scheme and (b) the new semi-implicit scheme.

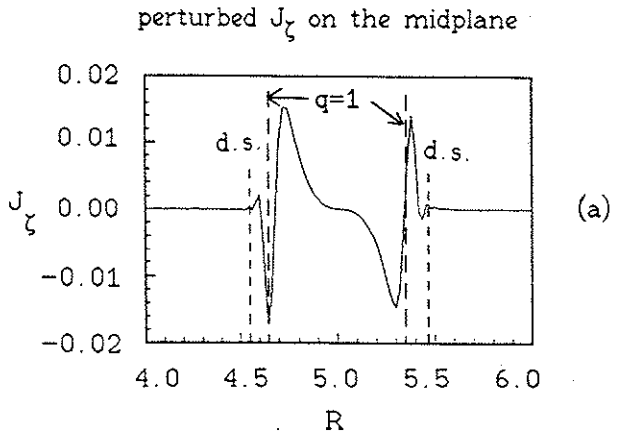

Fig. 5-24. Perturbed J_ζ of the n=1 component for (a) Equil. #13 (with plasma current in the common flux region) and (b) Equil. #14 (no plasma current in the common flux region).

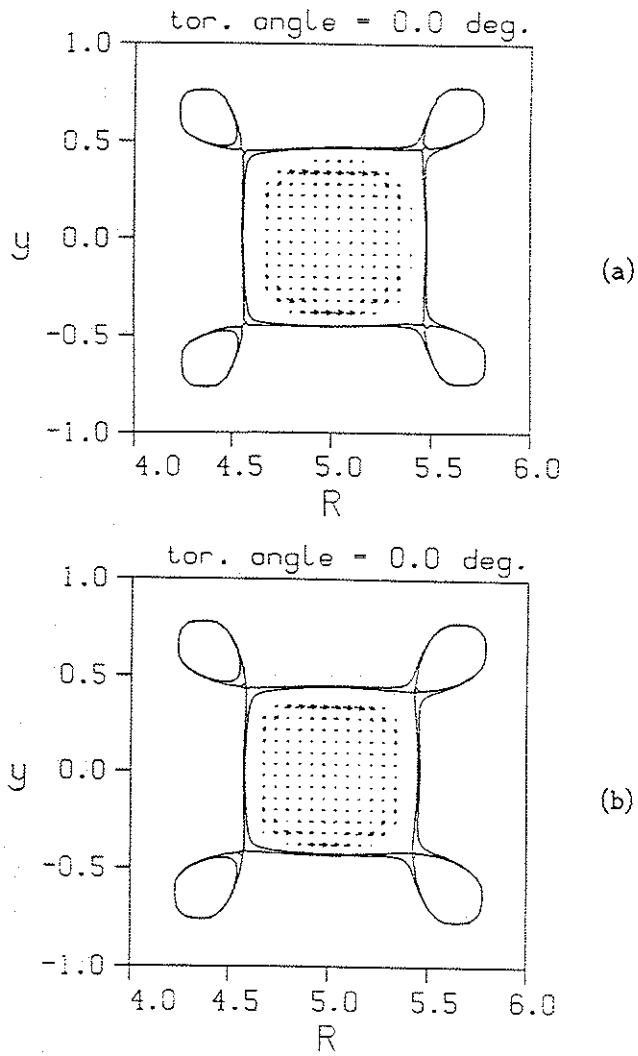

Fig. 5-25. Plasma flow patterns of the n=1 component for (a) Equil. #13 (with the plasma current in the common flux region) and (b) Equil. #14 (no plasma current in the common flux region).

To facilitate a comparison with experiment, we conduct linear calculations for a family of equilibrium pairs that have more realistic J_ζ profiles. A representative pair are Equil.#15 and #16. The q value on the magnetic axis is changed from 0.83 to 0.55, and thereby the distance between the q=1 surface and the divertor separatrix is changed from 0.15a to 0.05a. The result of this parameter survey is shown in Fig.5-26. Unlike the m=2,n=1 tearing mode, the effect of the divertor

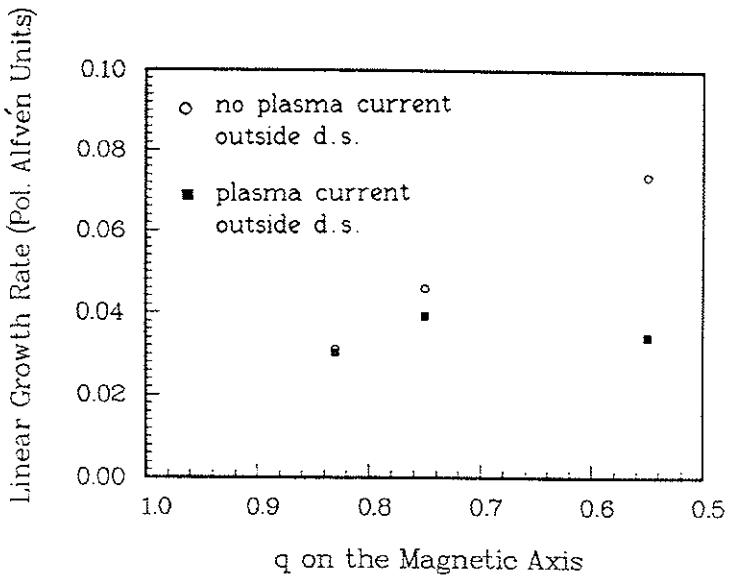

Fig.5-26. Effects of plasma current in the common flux region and the value of q_{axis} on the linear growth rate of the n=1 component (m=1,n=1 resistive kink mode dominant). As q_{axis} decreases, the q=1 surface moves closer to the divertor separatrix.

separatrix is small on the m=1,n=1 resistive kink mode; no significant stabilization effect is observed, if any.

5-3-3. Nonlinear results

The nonlinear calculations of the m=2,n=1 tearing mode in section 5-2-3 strongly suggest that the nonlinear option of our RPD code works quite well for a square cross-section tokamak with a four-node poloidal divertor. It is of great interest to extend our nonlinear work to the case in which the m=1,n=1 resistive kink mode is initially dominant. This would allow us to address the question of partial reconnection of the m=1,n=1 magnetic island in a poloidal divertor tokamak.

Equil.#13 and #17 are used to conduct nonlinear simulations. Because of the limited computer time allocation available we must presently restrict ourselves to cases with only a few toroidal Fourier harmonics. Thus, the results presented here are subject to considerable numerical errors and should be regarded as preliminary in nature.

The nonlinear simulation of the m=1,n=1 resistive kink mode using Equil.#13 is very noteworthy because, as we shall see shortly, it exhibits a behavior that is consistent with partial reconnection of the island. The temporal evolution of the n=1 and 2 components of the magnetic energy are shown in Fig.5-27. For this particular run, a 60 by 60 grid was used

with only five Fourier components (0, 1^+, 1^-, 2^+ , and 2^-). Interestingly, the n=2 component is larger than, or at least comparable to, the n=1 component in the later phases of the simulation. This clearly suggests a definite need for many more toroidal Fourier harmonics for a converged result.

Setting aside this convergence problem, however, we move on to generate the puncture plots of the magnetic field structure and the plots of the total J_ζ on the midplane all at ζ=0 for $t=100\tau_{Hp}$ (Fig.5-28), $125\tau_{Hp}$ (Fig.5-29), $175\tau_{Hp}$ (Fig.5-30), and $200\tau_{Hp}$ (Fig.5-31). The original magnetic axis was never taken over completely by the huge m=1,n=1 magnetic island. Instead, it survived the reconnection process and recovered somewhat by $t=200\tau_{Hp}$. The q value of the original magnetic axis at $t=200\tau_{Hp}$ is found to be about 0.91.

A similar result (i.e., partial reconnection) is also obtained when we increase the grid size to 100 by 100 or the number of the toroidal Fourier harmonics to nine(0, 1^+, 1^-, 2^+, 2^-, 3^+, 3^-, 4^+, and 4^-). For example, the total J_ζ on the midplane at $t=200\tau_{Hp}$ again has a distinctive hump near the inner side of the divertor separatrix. (See Fig.5-32.) This corresponds to a small region surrounding the original magnetic axis that has been displaced from its initial position by the huge m=1,n=1 island. As for the convergence with the number of toroidal Fourier harmonics, the n=3 and 4 components of the

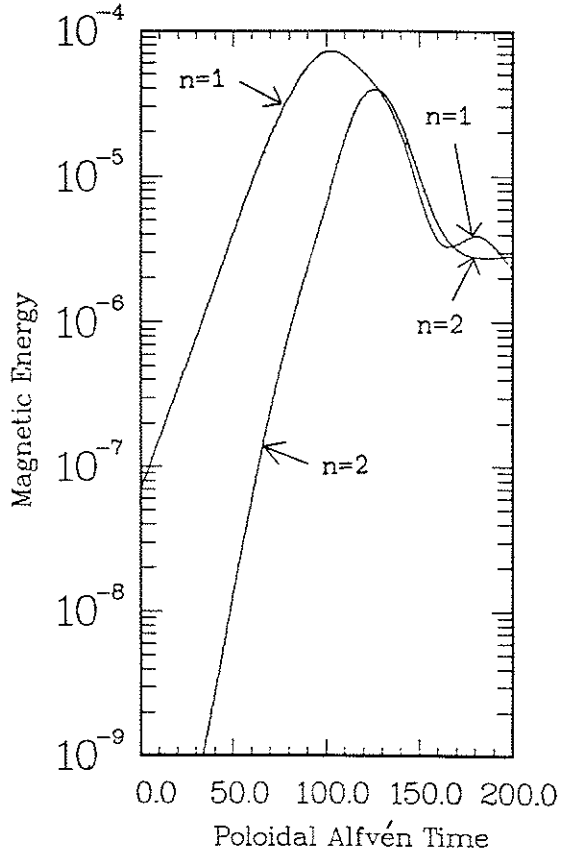

Fig.5-27. Temporal evolution of the n=1 and 2 components (m=1,n=1 resistive kink mode dominant) of the magnetic energy for Equil.#13. The magnetic energy is measured in units of $a^3(B_\zeta)^2/2\mu_0$.

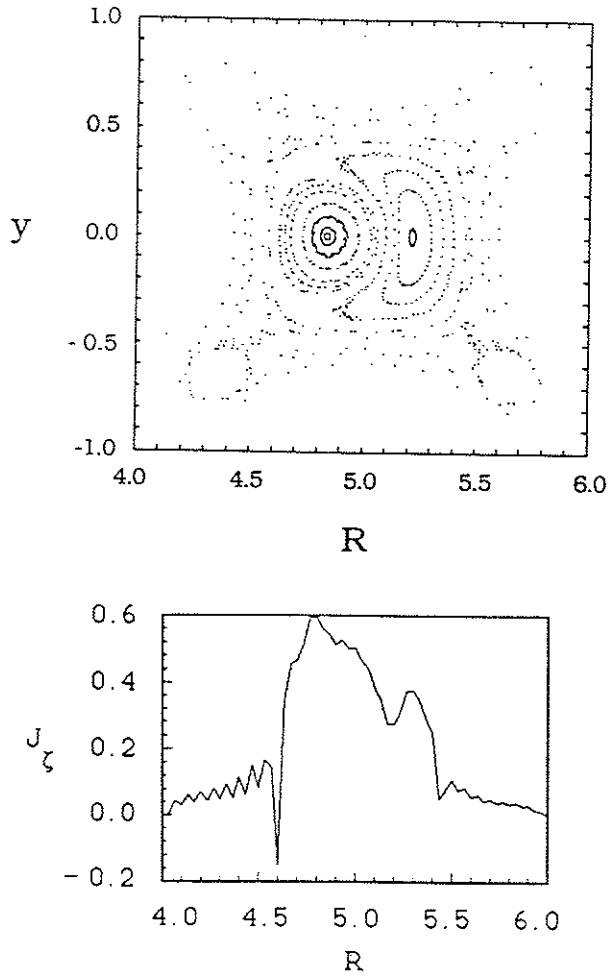

Fig.5-28. Puncture plot of the magnetic field and the total J_ζ on the midplane at ζ=0 for t=100τ_{Hp} with Equil.#13. A large m=1,n=1 magnetic island is present.

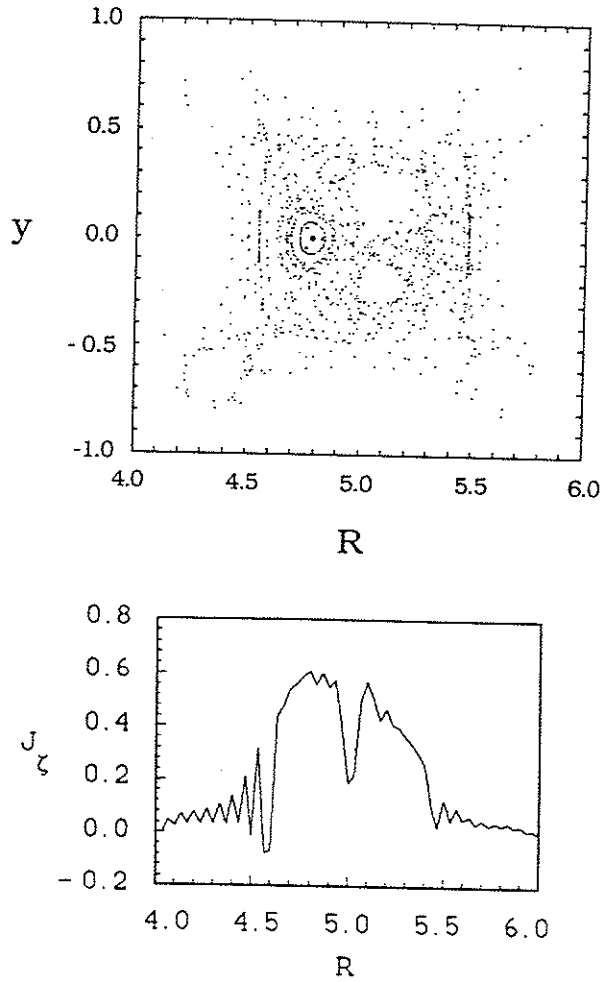

Fig.5-29. Puncture plot of the magnetic field and the total J_ζ on the midplane at ζ=0 for t=125τ_{Hp} with Equil.#13. The m=1,n=1 magnetic island continues to grow and considerable stochasticity develops in the island.

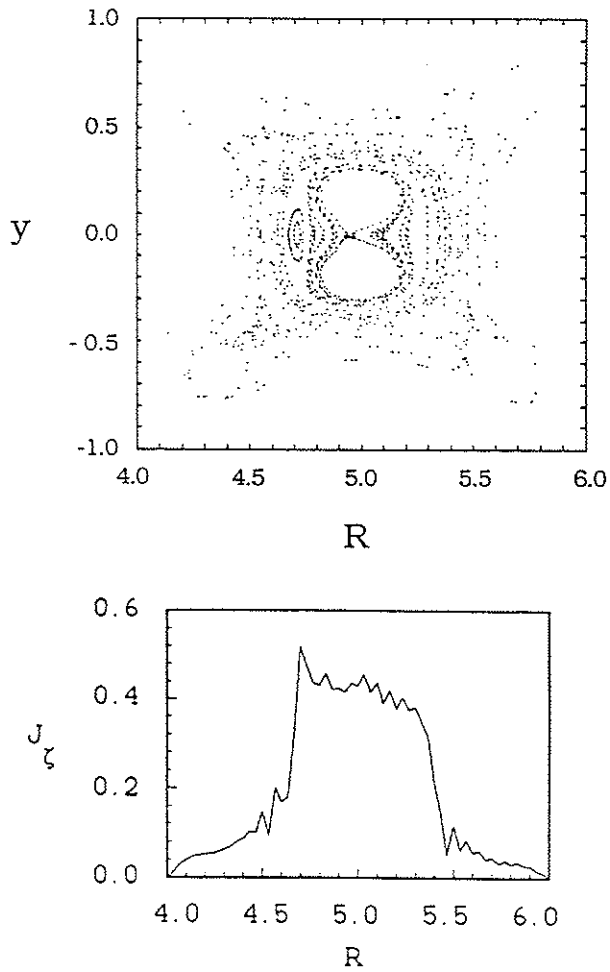

Fig. 5-30. Puncture plot of the magnetic field and the total J_ζ on the midplane at ζ=0 for t=175τ_{Hp} with Equil.#13. Despite the very large m=1, n=1 island, a small region near the original magnetic axis still remains. Flux surfaces can be identified in the region between the island and the divertor separatrix.

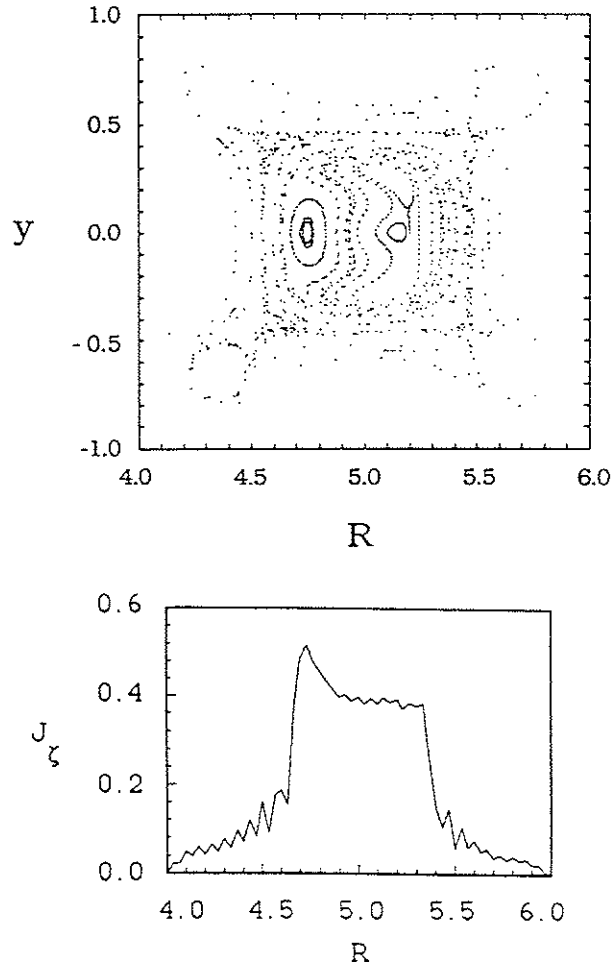

Fig. 5-31. Puncture plot of the magnetic field and the total J_ζ on the midplane at ζ=0 for t=200τ_{Hp} with Equil.#13. The m=1, n=1 island has shrunk somewhat without a total reconnection.

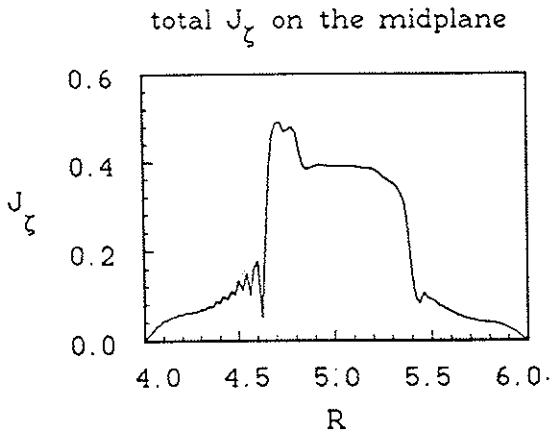

Fig.5-32. The total J_ζ on the midplane at ζ=0 for t=200τ_{Hp}. For this, a 100 by 100 grid is used with five Fourier harmonics.

magnetic energy are smaller than the n=1 component by factors of about 4 and 10, respectively.

A nonlinear simulation of the m=1, n=1 resistive kink mode using Equil.#17 results in a total reconnection of the island. We first show the temporal evolution of the n=1 and 2 components of the magnetic energy in Fig.5-33. A 100 by 100 grid is used with only five Fourier components. The magnetic Reynolds number S is taken to be 10^4 everywhere. As in the divertorless tokamak runs (see section 4-3-3), the n=1 component remains larger than the n=2 component throughout the simulation although the magnitudes are almost comparable in the later phases.

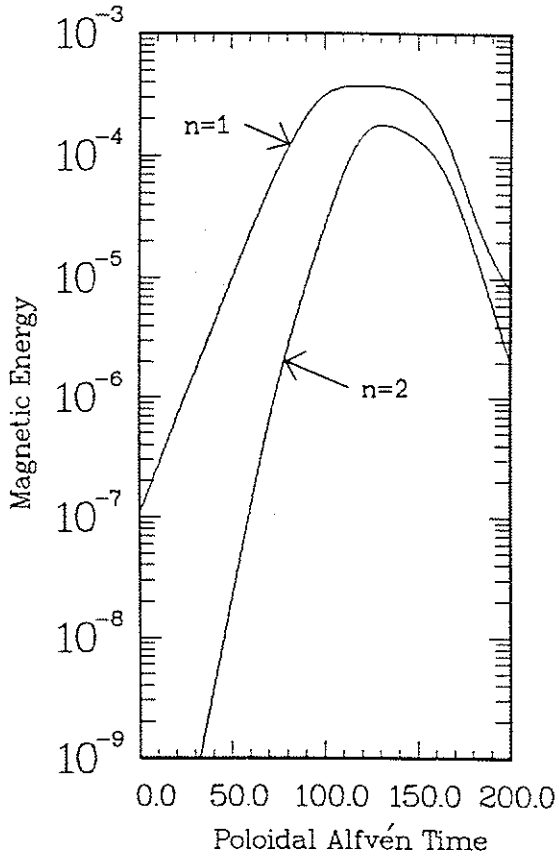

Fig.5-33. Temporal evolution of the n=1 and 2 components (m=1, n=1 resistive kink mode dominant) of the magnetic energy for Equil.#17. The magnetic energy is measured in units of $a^3(B_\zeta)^2/2\mu_0$.

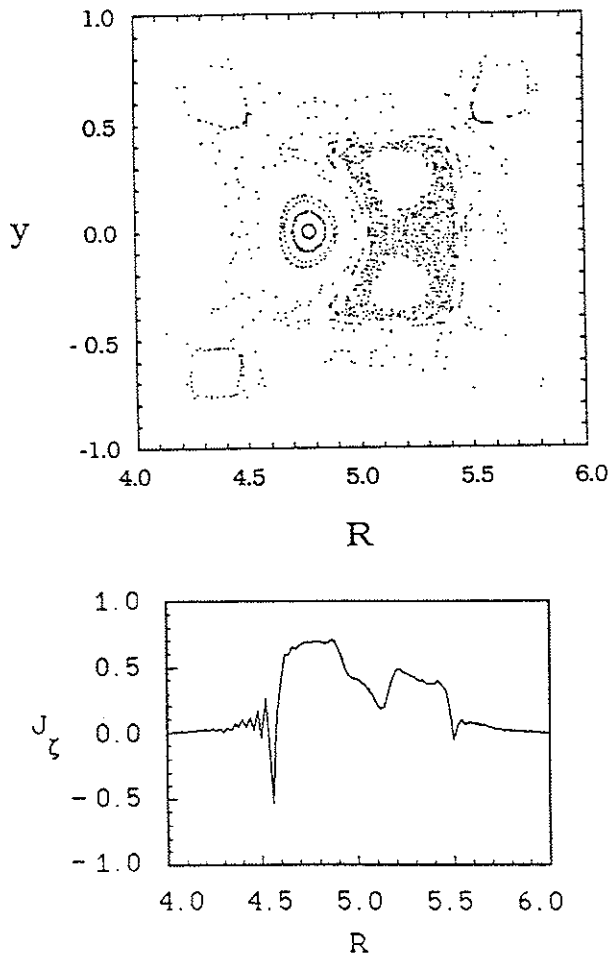

Fig.5-34. Puncture plot of the magnetic field and the total J_ζ on the midplane at ζ=0 for t=120τ_{Hp} with Equil.#17. The m=1,n=1 magnetic island begins to interact with the divertor separatrix.

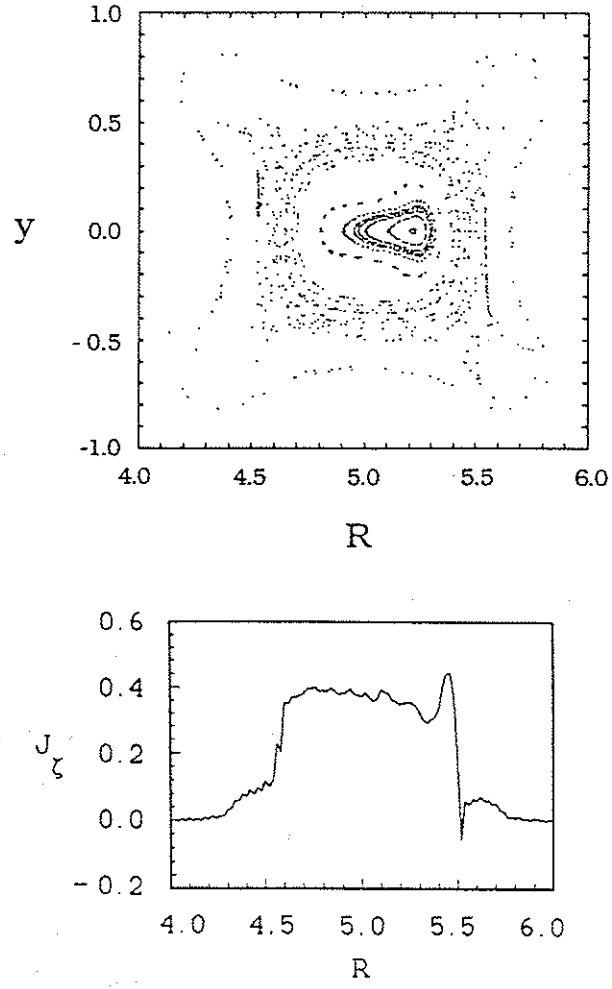

Fig.5-35. Puncture plot of the magnetic field and the total J_ζ on the midplane at ζ=0 at t=190τ_{Hp} for Equil.#17. Total reconnection has taken place.

Figs. 5-34 and 5-35 show the puncture plots of the magnetic field structure and the plots of the total J_ζ on the midplane at ζ=0 for t=120τ_{Hp} and 190τ_{Hp}. The original magnetic axis is completely taken over by the m=1,n=1 magnetic island and the q value rises above unity everywhere.

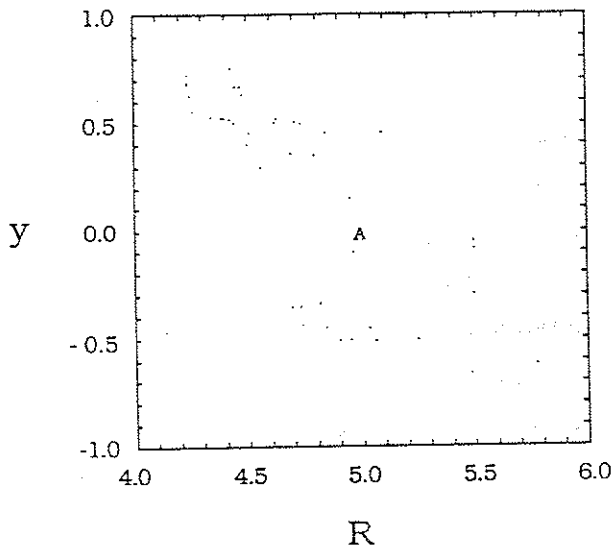

Fig. 5-36. Puncture plot of the magnetic field that illustrates the interaction of the m=1,n=1 magnetic island with the region outside the divertor separatrix. A magnetic field line is followed starting from the point 'A'.

It is not well understand why the m=1,n=1 island partially reconnected in one case while it totally reconnected in the other. A potentially relevant observation is that the magnetic stochasticity near the divertor separatrix is greater in the latter case. By connecting the regions inside and outside the divertor separatrix as in Fig. 5-36, the m=1,n=1 magnetic island may continue growing even after the helical flux between the q=1 surface and the divertor separatrix is exhausted for the reconnection process. This has also been seen in HIB code runs.[24] However, if for some reason the flux surfaces near the divertor separatrix are resilient, the island growth has to come to a halt when the helical flux supply is used up. It is possible that this is the case for Equil.#13 because the q=1 surface is further away from the divertor separatrix and the interaction of the m=1,n=1 island with the divertor separatrix is weaker.

5-4. Comparison with Tokapole II Experiments[30,41-43]

A large number of linear runs and a limited number of nonlinear runs have been carried out for a four-node poloidal divertor tokamak. We are now in a position to start comparing our RPD results with the MHD behavior of Tokapole discharges obtained by the experimental group.[23,24,26-30] However, we need to proceed with caution.

To lessen the toroidal effects that could contaminate and

obscure the effects of the divertor separatrix on resistive MHD instabilities, a fairly straight geometry of $R_0/a = 5$ was used throughout our numerical work. On the other hand, Tokapole II is a more tightly curved tokamak with $R_0/a = 50cm/22cm \approx 2.27$. In the laboratory experiment toroidal effects might be playing quite an important role.

Numerically, we have considered two types of MHD equilibria: one with and one without plasma current flowing outside the divertor separatrix. The former corresponds to a magnetic limiter discharge. The latter was intended to simulate a material limiter discharge in which little plasma is present outside the divertor separatrix. However, because of a constant resistivity assumption the physical characteristics of the common flux region are different from those in the experiment. Our numerical work allows a conducting fluid in the common flux region even if the plasma current is removed.

In view of such differences as well as a lack of sufficient experimental data for the current profile in Tokapole II discharges, we do not attempt any detailed quantitative comparisons of the numerical and experimental results. Instead, we just point out aspects of our numerical results that are qualitatively consistent with the experimental results obtained by the experimental group. Readers are encouraged to refer back to Fig.1-4 of chapter 1 to remind themselves of the key features of Tokapole II discharges.

Fig.5-11 shows numerically that the m=2,n=1 tearing mode tends to be linearly stabilized as q_{axis} is lowered and the q=2 surface is brought closer to the divertor separatrix. This agrees with the experimental result that the major and/or minor disruptions, for which the m=2,n=1 tearing mode is believed to be at least partially responsible, are suppressed at lower volume averaged q. Furthermore, it has been shown numerically that the m=2,n=1 mode tends to be linearly stabilized at a lower q_{axis} value when plasma current is removed from the common flux region. Experimentally, the MHD behavior due to the m=2,n=1 tearing mode disappears at a lower volume averaged q for the material limiter discharges than for the magnetic limiter discharges (namely, $\langle q \rangle \sim 1.7$ for the material limiter discharges and $\langle q \rangle \sim 2.2$ for the magnetic limiter discharges). Thus, the numerical and experimental results are in qualitative agreement.

The m=2,n=1 magnetic island was shown to saturate nonlinearly before the onset of significant stochasticity if the separation between the q=2 surface and the divertor separatrix was large. Rotation of such an island can account for the m=2,n=1 Mirnov oscillations observed in the Tokapole II discharges as in a standard divertorless tokamak.

As for the m=1,n=1 resistive kink mode, it was found to be linearly unstable regardless of the plasma current outside the divertor separatrix as long as $q_{axis}<1$. (See Fig.5-26.) This is

consistent with experimental observations where sawtooth oscillations, which are believed to be due to the m=1,n=1 resistive kink mode, are seen in both magnetic and material limiter discharges for sufficiently low <q> values.

Our RPD code has shown that at least for one equilibrium the m=1,n=1 magnetic island does not totally reconnect. This is a very significant result because this partial reconnection phenomenon can account for attainment of low q discharges in Tokapole II. It is possible that the divertor separatrix is resilient enough to prevent the growth of a magnetic island beyond the divertor separatrix for certain divertor equilibria. However, it should be emphasized that the nonlinear calculations of the m=1,n=1 resistive kink mode are still of a preliminary nature; further investigation is required before a final verdict can be reached.

Chapter 6 SUMMARY, CONCLUSION, AND SUGGESTIONS FOR FUTURE WORK

6-1. Summary and Conclusions

We have successfully developed from scratch a resistive MHD simulation package for a square cross-section tokamak with or without a poloidal divertor. The package consists of the axisymmetric MHD equilibrium code EQPD (with the initialization code SETPD) and the 3-D nonlinear resistive MHD initial value code RPD.

EQPD uses the basic features of the Chodura-Schlüter method in which a plasma with a small ficticious friction is relaxed into a stationary state that is an MHD equilibrium. EQPD assumes axisymmetry, thereby reducing the problem to two dimensions. In advancing the three dependent variables ψ(poloidal flux function), P(pressure), and I(poloidal current function), the functional forms of $P=P(\psi)$ and the safety factor $q=q(\psi)$ are preserved. As a result, EQPD is capable of generating axisymmetric MHD equilibria over a wide range of plasma beta for a divertorless tokamak. In a divertor geometry, however, significant spurious numerical oscillations in the current density were observed in the vicinity of the divertor rings and the divertor separatrix. This problem has been overcome partially by introducing a small but finite resistivity in the code. Although calculation of the MHD

equilibrium is not the main topic of this thesis, it was an indispensable part of our work. All of the axisymmetric equilibria for the resistive MHD instability studies in this thesis were calculated with EQPD.

The RPD code numerically advances a full set of 3-D compressible resistive MHD equations either linearly or nonlinearly. The code is fully toroidal and no aspect ratio ordering assumption is made. In order to handle the complicated geometry including the poloidal divertor separatrix and the region outside it, all the dependent variables are finite differenced in the two Cartesian directions of a constant toroidal angle plane. They are, however, Fourier analyzed in the toroidal direction to facilitate an efficient mode representation.

An earlier version of our RPD code employed a mostly explicit time advancement scheme and the maximum step size for numerical stability was quite restrictive. This was overcome by developing and implementing a new semi-implicit scheme that approximately removes the step size restriction imposed by the fast compressional waves. The new semi-implicit scheme is based on that proposed by Harned and Kerner, but an operating splitting method is applied to the simplified semi-implicit operator. As a result, only a set of small tridiagonal matrices need be solved in advancing the plasma velocity despite a 2-D finite difference, 1-D spectral spatial representation. Typically, the semi-implicit scheme

speeded up the code by a factor of one to three times the aspect ratio in a divertorless geometry and by a factor of somewhat less than the aspect ratio in a poloidal divertor geometry.

We first conducted very extensive, if not exhaustive, numerical tests of our RPD code and the new semi-implicit scheme using a number of divertorless tokamak equilibria. The linear and nonlinear results for the m=2,n=1 tearing mode and the m=1,n=1 resistive kink mode were all shown to be in good agreement with the standard analytic and/or numerical results. The results obtained with the semi-implicit scheme were also shown to be in good agreement with those from the mostly explicit scheme except for some minor differences due to the dispersive effect of the semi-implicit term. The numerical characteristics of the code, such as grid convergence and step size convergence, were found to be satisfactory. We conclude that our 3-D resistive MHD initial value code RPD works correctly for a divertorless tokamak and our new semi-implicit scheme is a simple yet very powerful method for significantly improving the efficiency of a 2-D finite difference, 1-D spectral resistive MHD code.

Next we extended our work to a poloidal divertor geometry. A version of RPD with a four-node poloidal divertor was used exclusively to study the effect of the divertor separatrix and the plasma current outside of it on resistive MHD instabilities. After successful verification of the code in such a

geometry and of the new semi-implicit scheme, we studied the linear and nonlinear behavior of the m=2, n=1 tearing mode and the m=1, n=1 resistive kink mode.

The new physics results obtained can be summarized as follows. Placing the divertor separatrix near the q=2 surface tends to strongly stabilize the linear growth of the m=2, n=1 tearing mode. On the other hand, the proximity of the divertor separatrix to the q=1 surface has only a very small effect on the linear stability of the m=1, n=1 resistive kink mode. For experimentally realistic equilibria, plasma current outside the divertor separatrix tends to linearly stabilize the m=2, n=1 tearing mode by modifying the current profile near the mode rational surface and the divertor separatrix. A similar effect is seen for the m=1, n=1 resistive kink mode, but to a lesser extent. However, merely removing the plasma current from the common flux region without significantly altering the current profile inside the divertor separatrix does not destabilize the m=2, n=1 or m=1, n=1 linear modes.

The nonlinear simulation results are still of a preliminary nature. Our observations include the saturation of the m=2, n=1 magnetic island as is common in a standard divertorless tokamak. If the separation between the q=2 surface and the divertor separatrix is small, however, the m=2, n=1 magnetic island and the divertor separatrix overlap and stochasticity develops before the saturation of the island

growth. Similarly, for the m=1, n=1 resistive kink, for at least one equilibrium the magnetic island fails to totally reconnect but instead saturates. In this case stochasticity of the magnetic field near the divertor separatrix is not as prevalent as the case in which the m=1, n=1 magnetic island did totally reconnect.

Finally, our numerical results were compared qualitatively with the MHD behavior observed in the Tokapole II discharges. Partly because of a lack of sufficient experimental profile data and partly because of simplifying assumptions employed in our numerical work (e.g., larger aspect ratio and uniform resistivity except near the divertor rings), a detailed quantitative comparison of the numerical and experimental results was not possible. Nevertheless, the numerical and experimental results were found to be qualitatively in good agreement.

6-2. Suggestions for Future Work

Although over 500 hours of supercomputer time has been used to carry out this research project, our work is far from complete. Our resistive MHD package for a poloidal divertor tokamak is not totally problem-free and some modifications and improvements are desirable. We are still left with a virtually unbounded parameter space to explore. In this last section of my thesis, I present a partial list of future work to be done on

and with our resistive MHD package for a poloidal divertor tokamak.

The main weakness of our resistive MHD package lies in the generation of an equilibrium input. The highly nonlinear nature of a divertor equilibrium makes it difficult to come up with a good set of numerical equilibria to study and compare; changing one parameter almost invariably results in changing many others that we want to keep fixed. A systematic approach should be developed and implemented in the equilibrium code to generate a better set of controlled equilibria. In addition, a divertor equilibrium obtained with our EQPD code sometimes suffers from a minor convergence problem in the region near the divertor separatrix that we are most interested in. The problem becomes significant for a high beta and/or tight aspect ratio plasma in which the axis shift is large. Although this problem can be overcome partially by increasing the numerical resistivity, the plasma profile will then be altered. To circumvent such problems, we need to develop a new axisymmetric MHD equilibrium code that would most likely employ a standard Grad-Shafranov solver.

The 3-D resistive MHD code RPD including the poloidal divertor works very well for a wide range of plasma parameters. The new semi-implicit scheme allows us to increase the code efficiency by a factor of somewhat less than the aspect ratio compared with the mostly explicit scheme.

Yet, the code efficiency becomes too poor for a high resolution run. An option of grid packing in the vicinity of the divertor rings would help us alleviate this problem somewhat. To make major progress, however, we need to develop an improved semi-implicit scheme that would further relax the temporal step size restriction for numerical stability. For such a scheme we also need to add a predictor-corrector step to make the temporal advancement second-order accurate in time.

To better simulate the material limiter discharge, it is desirable to use a resistivity profile that rises sharply in the common flux region. Unfortunately, a very high resistivity in the vicinity of a divertor ring tends to make the RPD code numerical unstable due to the step size restriction imposed by a rapid diffusive time scale there. We need to improve our treatment of the resistivity term near the ring to overcome this problem.

Many nonlinear runs, especially the ones in which the m=1,n=1 resistive kink mode is dominant, were not well converged because of an insufficient number of toroidal Fourier harmonics and grid points for the problem. To ascertain the partial reconnection of the m=1,n=1 magnetic island, it is essential to repeat our calculations including more Fourier harmonics and grid points. Furthermore, at least several more poloidal divertor tokamak equilibria with $q_{axis}<1$ need to be studied to establish a correlation between the equilibrium profile

and the occurence of partial reconnection.

To bring out the effect of the divertor separatrix on the resistive MHD instabilities, we chose to use a fairly straight tokamak of $R_0/a = 5$. On the other hand, the Tokapole II is a more tightly curved tokamak with $R_0/a \simeq 2.27$. It is possible, and even probable, that toroidal effects are also playing a major role in the experiments. It is of great interest to repeat the linear and nonlinear simulations of resistive MHD instabilities in a tightly curved poloidal divertor tokamak. Along with better experimental profile information, we could then embark on a quantitative comparison of the numerical and experimental results.

In a four-node divertor tokamak such as Tokapole II the flux surfaces near the divertor separatrix become highly noncircular and squarish. Although the squarishness is a consequence of the four-node divertor, this obscures the effect of the divertor x point itself on the linear and nonlinear evolution of resistive MHD instabilities. It would be instructive to repeat our simulation work for different divertor configurations. A simpler version of RPD without a poloidal divertor is also helpful for this investigation. By choosing an equilibrium with the mode rational surface close to the square wall, the effect of squarishness on the resistive MHD instabilities could be examined.

Although the RPD code employs the set of compressible

resistive MHD equations, the effect of finite plasma pressure was never vigorously studied. By including the finite pressure effects in a divertor geometry, we may be able to shed some light on the H-mode of divertor tokamak operation.[64]

References

1. H.P. Furth, J. Killeen, and M.N. Rosenbluth, Phys. Fluids 6, 459 (1963).

2. J.D. Callen, B.V. Waddell, B. Carreras, M. Azumi, P.J. Catto, H.R. Hicks, J.A. Holmes, D.K. Lee, S.J. Lynch, J. Smith, M. Soler, K.T. Tsang, and J.C. Whitson, in Plasma Physics and Controlled Nuclear Fusion Research 1978 (Proc. 7th Conf., Innsbruck, 1978) vol.1, IAEA, Vienna, p.415 (1979).

3. G. Bateman, MHD Instabilities (MIT Press, Cambridge, MA, 1978).

4. A.B. Rochester and T.H. Stix, Phys. Rev. Letters 36, 587 (1976).

5. S.V. Mirnov and I.B. Semenov, Sov. J. Atomic Energy 30, 22 (1971).

6. S. von Goeler, W. Stodiek, and N. Sauthoff, Phys. Rev. Letters 33, 1201 (1974).

7. E.P. Gorbunov and K.A. Razumova, J. Nucl. Energy, Part C 6, 515 (1964).

8. R.B. White, D.A. Monticello, M.N. Rosenbluth, and B.V. Waddell, Phys. Fluids 20, 800 (1977).

9. B. Carreras, B.V. Waddell, and H.R. Hicks, Nuclear Fusion 19, 1423 (1979).

10. W. Park, Bull. Am. Phys. Soc. 31, 1527 (1986).

11. B.B. Kadomtsev, Sov. J. Plasma Phys. 1, 389 (1975).

12. A. Sykes and J.A. Wesson, Phys. Rev. Letters 37, 140 (1976).

13. G.L. Jahns, M. Soler, B.V. Waddell, J.D. Callen, and H.R. Hicks, Nuclear Fusion 18, 609 (1978).

14. B.V. Waddell, M.N. Rosenbluth, D.A. Monticello, and R.B. White, Nuclear Fusion 16, 528 (1976).

15. R.D. Hazeltine, J.D. Meiss, and P.J. Morrison, Phys. Fluids 29, 1633 (1986).

16. B.V. Waddell, B. Carreras, H.R. Hicks, J.A. Holmes, and D.K. Lee, Phys. Rev. Letters 41, 1386 (1978).

17. B.V. Waddell, B. Carreras, H.R. Hicks, and J.A. Holmes, Phys. Fluids 22, 896 (1979).

18. B. Carreras, H.R. Hicks, J.A. Holmes, and B.V. Waddell, Phys. Fluids 23, 1811 (1980).

19. A.P. Biddle, R.N. Dexter, R.J. Groebner, D.T. Holly, B. Lipschultz, M.W. Phillips, S.C. Prager, and J.C. Sprott, Nuclear Fusion 19, 1509 (1979).

20. M. Keilhacker, D.B. Albert, K. Behringer, R. Behrisch, W. Engelhardt, G. Fussmann, J. Gernhardt, E. Glock, G. Haas, G. Herppich, Y. Shie, F. Karger, O. Klüber, M. Kornherr, K. Lackner, G. Lisitano, Ch. Liu, H.M. Mayer, D. Meisel, R. Müller, H. Murmann, H. Niedermeyer, W. Poschenrieder, H. Rapp, S. Rossnagel, J. Roth, N. Ruhs, B. Scherzer, F. Schneider, S. Sesnic, G. Siller, P. Staib, G. Staudenmaier, F. Wagner, K. Wang, H. Wedler, and F. Wesner, in Plasma Physics and Controlled Nuclear Fusion Research 1980 (Proc. 8th Conf., Brussels, 1980) vol.2,

IAEA, Vienna, p.351 (1981).

21. DIVA Group, Nuclear Fusion 18, 1619 (1978).

22. D. Meade, V. Arunasalam, C. Barnes, M. Bell, M. Bitter, K. Bol, R. Budny, J. Cecchi, S. Cohen, C. Daughney, S. Davis, D. Dimock, F. Dylla, P. Efthimion, H. Eubank, R. Fonck, R. Goldston, B. Grek, R. Hawryluk, E. Hinnov, H. Hsuan, M. Irie, R. Jacobsen, D. Johnson, L. Johnson, H. Kugel, H. Maeda, D. Manos, D. Mansfield, R. McCann, D. McCune, K. McGuire, D. Mikkelson, S.L. Milora, D. Mueller, M. Okabayashi, K. Owens, M. Reusch, K. Sato, N. Sauthoff, G. Schmidt, J. Schmidt, E. Silver, J. Sinnis, J. Strachan, S. Suckewer, H. Takahashi, and F. Tenney, in Plasma Physics and Controlled Nuclear Fusion Research 1980 (Proc. 8th Conf., Brussels, 1980) vol.1, IAEA, Vienna, p.665 (1981).

23. T.H. Osborne, R.N. Dexter, and S.C. Prager, Phys. Rev. Letters 49, 734 (1982).

24. T.H. Osborne, Ph.D. Thesis, University of Wisconsin-Madison (1984).

25. N.S. Brickhouse, J.D. Callen, R.N. Dexter, D.E.Graessle, D. Kortbawi, R.A. Moyer, T.H. Osborne, S.C. Prager, J.S. Sarff, J.C. Sprott, E. Uchimoto, C.K. Chu, J. DeLucia, A. Deniz, R.A. Gross, A.A. Grossman, A. Holland, F.M. Levinton, M. Machida, T.C. Marshall, and G.A. Navratil, in Plasma Physics and Controlled Nuclear Fusion Research 1984 (Proc. 10th Conf., London, 1984) vol.1, IAEA, Vienna, p.385 (1985).

26. T.H. Osborne, N.S. Brickhouse, R.N. Dexter, R.A. Moyer, and S.C. Prager, Bull. Am. Phys. Soc. 29, 1337 (1984).

27. N.S. Brickhouse, T.H. Osborne, R.N. Dexter, S.C. Prager, Phys. Fluids 28, 3429 (1985).

28. R.A. Moyer, R.N. Dexter, and S.C. Prager, Bull. Am. Phys. Soc. 30, 1441 (1985).

29. R.A. Moyer, R.N. Dexter, J.A. Goetz, S.C. Prager, and I.H. Tan, Bull. Am. Phys. Soc. 31, 1594 (1986).

30. R.A. Moyer, Ph.D. Thesis, University of Wisconsin-Madison, in preparation.

31. J.D. Callen, W.X. Qu, K.D. Siebert, B.A. Carreras, K.C. Shaing, and D.A. Spong, in Plasma Physics and Controlled Nuclear Fusion Research 1986 (Proc. 11th Conf., Kyoto, 1986) vol.2, IAEA, Vienna, p.157 (1987).

32. J. Manickam, W. Park, D. Monticello, A.E. Miller, and F.W. Perkins, Bull. Am. Phys. Soc. 29, 1295 (1984).

33. W. Park, D. Monticello, and R.B. White, Bull. Am. Phys. Soc. 23, 779 (1978).

34. H.R. Strauss, W. Park, D.A. Monticello, R.B. White, S.C. Jardin, M.S. Chance, A.M.M. Todd, and A. H. Glasser, Nuclear Fusion 20, 638 (1980).

35. H.R. Strauss, Phys. Fluids 19, 134 (1976).

36. E. Uchimoto, J.D. Callen, and L. Garcia, Bull. Am. Phys, Soc. 30, 1421 (1985).

37. E. Uchimoto and J.D. Callen, Sherwood Theory Conference (San Diego, California, 1987), paper 1D18.

38. D.S. Harned and W. Kerner, J. Comp. Phys. 60, 62

(1985).

39. E. Uchimoto, J.D. Callen, L. Garcia, and B.A. Carreras, Sherwood Theory Conference (Incline Village, Nevada, 1984), paper 1Q19.

40. R. Chodura and A. Schlüter, J. Comp. Phys. 41, 68 (1981).

41. E. Uchimoto and J.D. Callen, in the 12th Conference on the Numerical Simulation of Plasmas (San Francisco, Sept. 20-23, 1987), paper PM23.

42. R.A. Moyer, E. Uchimoto, J.D. Callen, R.N. Dexter, J.A. Goetz, S.C. Prager, and I.H. Tan, Bull. Am. Phys. Soc. 32, 1774 (1987).

43. Zuoyang Chang, E, Uchimoto, J.D. Callen, and S.C. Prager, Bull. Am. Phys, Soc. 32, 1774 (1987).

44. H. Grad and H. Rubin, in "Proceedings of Second International Conference on the Peaceful Uses of Atomic Energy" (United Nations, Geneva, 1958), Vol.31, p.190.

45. V.D. Shafranov, Sov. Phys.-JETP 10, 775 (1960).

46. J.D. Callen and R.A. Dory, Phys. Fluids 15, 1523 (1972).

47. M.S. Chu, D. Dobrott, T.H. Jensen, and T. Tamano, Phys. Fluids 17, 1183 (1974).

48. K. Lackner, Comp. Phys. Comm. 12, 33 (1976).

49. L.L. Lao, S.P. Hirshman, and R.M. Wieland, Phys. Fluids 24, 1431 (1981).

50. M.W. Phillips, University of Wisconsin PLP 765 (1978). (PLP is an internal report of the Plasma Physics Group at the Department of Physics of the University of Wisconsin-Madison. Copies are available upon request from Plasma Physics Group, Department of Physics, 1150 University Avenue, University of Wisconsin, Madison, Wisconsin 53706.)

51. V.D. Shafranov, Nuclear Fusion 3, 183 (1963).

52. E.I. Yurchenko, Sov. Phys. Tech. Phys. 12, 1057 (1968).

53. H.R. Strauss, Phys. Rev. Letters 26, 616 (1971).

54. H.R. Hicks, B. Carreras, J.A. Holmes, D.K. Lee, and B.V. Waddell, J. Comp. Phys. 44, 46 (1981); Erratum: J. Comp. Phys. 53, 205 (1984).

55. L.A. Charlton, J.A. Holmes, H.R. Hicks, V.E. Lynch, and B.A. Carreras, J. Comp. Phys. 63, 107 (1986).

56. J.A. Holmes, L.A. Charlton, B.A. Carreras, and V.E. Lynch, in the 12th Conference on the Numerical Simulation of Plasmas (San Francisco, Sept. 20-23, 1987), paper IW3.

57. B.A. Carreras, J.A. Holmes, H.R. Hicks, and V.E. Lynch, Nuclear Fusion 21, 511 (1981).

58. J.K. Lee, M.S. Chu, F.J. Helton, J.Y. Hsu, and N. Ohyabu, Bull. Am. Phys. Soc 30, 1421 (1985).

59. J.K. Lee, Phys. Fluids 29, 1629 (1986).

60. J.A. Holmes, B.A. Carreras, T.C. Hender, H.R. Hicks,

V.E. Lynch, and B.F. Masden, Phys. Fluids 26, 2569 (1983).

61. R. Courant, K.O. Friedrichs, and H. Lewy, Math. Ann. 100, 32 (1928).

62. R. Izzo, D.A. Monticello, H.R. Strauss, W. Park, J. Manickam, R.C. Grimm, and J. Delucia, Phys. Fluids, 26, 3066 (1983).

63. A.Y. Aydemir and D.C. Barnes, J. Comp. Phys. 53, 100 (1984).

64. F. Wagner, G. Becker, K. Behringer, D. Campbell, A. Eberhagen, W. Engelhardt, G. Fussmann, O. Gehre, J. Gernhardt, G.v. Gierke, G. Haas, M. Huang, F. Karger, M. Keilhacker, O. Klüber, M. Kornherr, K. Lackner, G. Lisitano, G.G. Lister, H.M. Mayer, D. Meisel, E. Müller, H. Murmann, H. Niedermeyer, W. Poschenrieder, H. Rapp, H. Röhr, F. Schneider, G. Siller, E. Speth, A. Stäbler, K.H. Steuer, G. Venus, O.Vollmer, and Z. Yü, Phys. Rev. Letters 49, 1408 (1982).

65. C.H. Finan III and J. Killeen, Comp. Phys. Comm. 24, 441 (1981).

66. D.S. Harned and W. Kerner, Nucl. Sci. Eng. 92, 119 (1986).

67. D.S. Harned and D.D. Schnack, J. Comp. Phys. 65, 57 (1986).

68. D.D. Schnack, D.C. Barnes, Z. Mikic, D.S. Harned, E.J. Caramana, J. Comp. Phys. 70, 330 (1987).

69. N.J. O'Neill and A.A. Mirin, National Magnetic Fusion

Energy Computer Center, LIBRIS Library.

70. R.C. Grimm, R.L. Dewer, J. Manickam, S.C. Jardin, A.H. Glasser, and M.S. Chance, in Plasma Physics and Controlled Nuclear Fusion Research 1982 (Proc. 9th Conf., Baltimore, 1982) vol.3, IAEA, Vienna, p.35 (1983).

71. H. Strauss, D.A. Monticello, and J. Manickam, Bull. Am. Phys. Soc. 32, 1773 (1987).

72. B. Coppi, J.M. Greene, and J.L. Johnson, Nuclear Fusion 6, 101 (1966).

73. H.P. Furth, P.H. Rutherford, and H. Selberg, Phys. Fluids 16, 1054 (1973).

74. R. Izzo, D.A. Monticello, W. Park, J. Manickam, H.R. Strauss, R. Grimm, and K. McGuire, 26, 2240 (1983).

75. A.H. Glasser, J.M. Greene, and J.L. Johnson, Phys. Fluids 19, 567 (1976).

76. P.H. Rutherford, Phys. Fluids 16, 1903 (1973).

77. B. Coppi, R. Galvão, R. Pellat, M. Rosenbluth, and P. Rutherford, Sov. J. Plasma Phys. 2, 533 (1976).